2016

ELECTROPHYSIOLOGY OF BASAL GANGLIA (BG) CIRCUITRY AND DYSTONIA AS A MODEL OF MOTOR CONTROL DYSFUNCTION

Deepak Kumbhare
Virginia Commonwealth University

ELECTROPHYSIOLOGY OF BASAL GANGLIA (BG) CIRCUITRY AND DYSTONIA AS A MODEL OF MOTOR CONTROL DYSFUNCTION

A Dissertation submitted in partial fulfillment of the requirements for the degree of DOCTOR OF PHILOSOPHY at Virginia Commonwealth University.

by

DEEPAK KUMBHARE, M.S.

MASTER OF SCIENCE, VIRGINIA COMMONWEALTH UNIVERSITY, 2011

BACHELOR OF ENGINEERING, RAJIV GANDHI TECHNICAL UNIVERSTY, INDIA, 2007

Director: PAUL A. WETZEL, PH.D.

ASSOCIATE PROFESSOR,

DEPARTMENT OF BIOMEDICAL ENGINEERING

Virginia Commonwealth University

Richmond, Virginia

May 2016

ACKNOWLEDGEMENT

Firstly, I would like to thank my advisor, Dr. Paul A. Wetzel for providing me with this great research opportunity. Thank you for your support and encouragement in my research. I would like to express my gratitude to my mentor and project supervisor, Dr. Mark S. Baron for his guidance and support throughout this project. His extensive knowledge and encouragement to develop independent thinking has immensely enhanced my research skills. I would also like to thank Dr. Kathryn Holloway and Dr. Ann Rice for her invaluable suggestions and guidance. I would like to thank Nancy Smith and George Weistroffer for their valuable assistance throughout this project. I would also like to thank my committee members, Dr. Ding-Yu Fei, Dr. Ou Bai and Dr. Dianne T.V. Pawluk, for all their insightful comments and help in completion of this work. Last and most importantly, I would like to thank my family and friends for their enduring love and support.

TABLE OF CONTENT

Content **Page**

LIST OF TABLES

LIST OF FIGURES AND MOVIE

LIST OF ABBREVIATIONS

AA	Average accuracy
ACH	Autocorrelation Histogram
AF	Allan Factor
AI	Asymmetric Index
ANOVA	Analysis of Variance
BC	Biomodality Coefficient
BE	Burst Entropy
BG	Basal Ganglia
BGTC	Basal Ganglia Thalamocortocal Circuitry
BO	Burst Order
BP	Burst Percentage
BT	Burst Tendency
CA	Classification Accuracy
CI	Confidence Interval
CR	Coordinated Reset
CS	Clinical Score
CT	Computerized Tomogram
CV	Coefficient of Variation
CV2	Coefficient of Variation for a sequence of Two ISIs
Cx	Cortex
DA	Dopamine
DBS	Deep Brain Stimulation
Dfe	Degree of Freedom
DP	Discriminatory Power
DYT1	Dystonia 1 gene
EMG	Electromyography
EP	Entopeduncular nucleus (rat equivalent of GPi)
F_d	Dystonia Frequency
FF	Fano Factor
FN	False Negative
FP	False Positive
GABA	Gamma Aminobutyric Acid
GI*	Getis-Ord GI* statistic
GLM	Generalized Linear Model
GMI	Global Moran's I function
GP	Globus Pallidus (rat equivalent of GPe)
GPe	Globus Pallidus externus
GPi	Globus Pallidus internus
GUI	Graphical User Interface
HDS	Hartigan's Dip Statistics
IACUC	Institutional Animal Care and Use Committee
i.p.	Intraperitoneal injection

IR	Difference of the log of two adjacent ISIs
ISI	Interspike Interval
jj	Jaundiced rat
κ	Kappa, shape parameter of Gamma distribution
Kr	Kurtosis
LOS	Loss of Specificity
LTS	Low Threshold Ca^{2+} Spikes
LV	Local Variation of ISIs
LVr	Local Variation parameter with refractory period information
MC	Motor cortex
MC	Primary Motor Cortex
MER	Microelectrode Recordings
MMO	Multiple Metric Optimization
MPTP	1-methyl-4-phenyl-1,2,3,6-tetrahydropyridine
MRI	Magnetic Resonance Image
MSN	Medium Spiny Neurons
NAN	Not a Number
NeuroPAM	Processing-Analysis-Modeling of Neuronal system
Nj	Non-jaundiced rat
PCA	Principal Component Analysis
PD	Parkinson's disease
PETH	Perievent Time Histograms
PSP	Post Spike Suppression
ROC	Receiver Operating Characteristic
Sk	Skewness
SMA	Supplementary Motor Area
SNc	Substantia Nigra pars compacta
SNr	Substantia Nigra pars reticulate
STN	Subthalamic Nucleus
STR	Straitum
Sulfa	Sulfadimethoxine
TL	Thalamus
TN	True negative
TP	True positive
VL	Pallidal receiving Thalamus
VPL	Cerebellar-receiving VPL Thalamus

ABSTRACT

ELECTROPHYSIOLOGY OF BASAL GANGLIA (BG) CIRCUITRY AND DYSTONIA AS A MODEL OF MOTOR CONTROL DYSFUNCTION

By Deepak Kumbhare

A Dissertation submitted in partial fulfillment of the requirements for the degree of DOCTOR OF PHILOSOPHY at Virginia Commonwealth University.

Major Director: PAUL A. WETZEL, PH.D.

Associate Professor, Department of Biomedical Engineering

Virginia Commonwealth University, Richmond, VA

The basal ganglia (BG) is a complex set of heavily interconnected nuclei located in the central part of the brain that receives inputs from the several areas of the cortex and projects via the thalamus back to the prefrontal and motor cortical areas. Despite playing a significant part in multiple brain functions, the physiology of the BG and associated disorders like dystonia remain poorly understood. Dystonia is a devastating condition characterized by ineffective, twisting movements, prolonged co-contractions and contorted postures. Evidences suggest that it occurs due to abnormal discharge patterning in BG-thalamocortocal (BGTC) circuitry. The central purpose of this study was to understand the electrophysiology of BGTC circuitry and its role in motor control and dystonia.

Toward this goal, an advanced multi-target multi-unit recording and analysis system was utilized, which allows simultaneous collection and analysis of multiple neuronal units from multiple brain nuclei. Over the cause of this work, neuronal data from the globus pallidus (GP), subthalamic nucleus (STN), entopenduncular nucleus (EP), pallidal receiving thalamus (VL) and motor cortex (MC) was collected from normal, lesioned and dystonic rats under awake, head restrained conditions. The results have shown that the neuronal population in BG nuclei (GP, STN and EP) were characterized by a dichotomy of firing patterns in normal rats which remains preserved in dystonic rats. Unlike normals, neurons in dystonic rat exhibit reduced mean firing rate, increased irregularity and burstiness at resting state. The chaotic changes that occurs in BG leads to inadequate hyperpolarization levels within the VL thalamic neurons resulting in a shift from the normal bursting mode to an abnormal tonic firing pattern.

During movement, the dystonic EP generates abnormally synchronized and elongated burst duration which further corrupts the VL motor signals. It was finally concluded that the loss of specificity and temporal misalignment between motor neurons leads to corrupted signaling to the muscles resulting in dystonic behavior. Furthermore, this study reveals the importance of EP output in controlling firing modes occurring in the VL thalamus.

CHAPTER 1

INTRODUCTION

Movement control in vertebrates is a complex neural process that includes generation, modulation and transmission of motor signals controlling various temporal and spatial aspects of the desired movement. This requires a high level of coordination between different parts of brain. The final output is the relay of selective information to different muscles for precise movement with predetermined amplitude (strength), speed, selectivity and phasic relationship with other muscles (Aldridge et al., 2004) (Mink & Thach, 1991). Each element of this neural network is important for the proper functioning of this assiduous process. Damage or loss in any of these elements may cause impairment in movement quality. One of the most crucial element in the motor control pathway is the basal ganglia (BG) (Herrero et al., 2002) that plays a significant role in many brain functions including motor control. This important subcortical structure is located in the central part of the neuronal loop that receives inputs from the several areas of the cortex and projects via the thalamus back to the prefrontal and motor cortical areas (Nambu, 2011). Abnormality in BG function contributes to many neurological disorders including Parkinson's disease and dystonia. Although the BG anatomy has been studied extensively, to date, the functional mechanism and its role in motor control are still unknown. The electrophysiology of BG nuclei in normal and motor dysfunction states provides valuable information about the various intrinsic and extrinsic factors involved in the process. The central purpose of this study was to understand the physiology of BG and its role in motor control and BG associated disorders. This would include studying the neuronal activity of the BG using dystonia as a model of motor control dysfunction.

1.1. Basal Ganglia

The basal ganglia (BG) is a set of interconnected subcortical nuclei which influence cortical motor functioning through the cortico-BG-thalamo-cortical neural pathway (Steine, 2010). It consists of four main nuclei; striatum (STR), globus pallidus (GP), subthalamic nucleus (STN), and substantia nigra (SN), that are connected to each other, cerebral cortex and other mid brain structures through a complex series of circuits. The GP contains internal and external segments (GPI and GPe respectively), while SN contains distinct areas designated compacta (SNc) and reticulate (SNr). BG receives motor related cortical inputs via STR and STN, modulates the signal, and then, per current modeling, relays the processed inhibitory output via GPi and SNr to the pallidal receiving thalamus (VL-TL), which in turn excites the prefrontal/ motor cortical areas and brain stem (Leh et al., 2007). BG nuclei primarily employ three neurotransmitters, Gamma aminobutyric acid (GABA), glutamate, and dopamine (DA).

STR is the main input nucleus of BG, which receives excitatory inputs from the entire cortex, especially from the sensorimotor and the frontal cortex (fig 1.1). STR can be further divided into caudate, putamen, and ventral STR. Putamen is the primary site for motor related inputs. The majority of the afferent projections to STR synapse with medium spiny neurons (MSN). MSN constitute about 96% of the STR neuronal population. The output of MSN is diversely modulated by the presence of dopamine (DA), which has a differential effect on two major DA receptors found in MSNs of STR, namely D1 and D2. D1 receptors, which are predominately present in cells in the direct pathway, get excited in presence of DA, while D2 receptors which are mostly present in indirect pathway get inhibited by DA. Through these direct and indirect

pathways, STR regulates the activities of downstream BG via inhibitory GABA neurotransmitter. Subthalamic nucleus (STN) is the second major input nuclei of STR and plays an important role in modulation of the BG output signals. It primarily receives inputs from frontal and somatosensory cortex and STR. STN chiefly innervates the pallidum and SNr via excitatory glutamatergic projection neurons. STR forms a dual projection loop with GPi and GPe, an auto-stabilizing loop with GPe, and forms the hyper-direct pathway in the BG. The GP consist of two nuclei; Globus pallidus externus (GPe; or GP in rodents) and globus pallidus internus (GPi; entopenduncular nucleus, EP in rodents). The GP is a major relaying component of the indirect pathway of BG and projects inhibitory GABAeric outputs to both STN and GPi. GPi/ EP is the major output nuclei of BG, which is anatomically and physiologically similar to GPe/ GP. GPi receives inhibitory inputs from STR (via direct pathway) and GPe (via indirect pathway), and excitatory inputs from STN. GPi primarily relays its GABAergic projections to the pallidal receiving thalamic nucleus (ventro-lateral thalamus, VL). Substantia nigra (consisting of SNr and SNc) is presumed to play important roles in reward, addiction, and movement. The SNr is the second major output nuclei of BG, which in unison with GPi, innervates thalamus and superior colliculus. The Pars compacta (SNc) produces the DA, which influences D1 and D2 type receptors in STR, and thus is very significant in maintaining balance in the striatal pathway.

Modulation of incoming motor signal within BG is an intricate process, which includes interaction of various elements of intrinsic BG nuclei. The BG is thought to have an essential role in motor control due to its unique anatomical centralized position in the brain's motor control system, and it being a recipient of a variety of input information from different parts of cortex and thalamus. BG is presumed to be involved in action selection (Mink, 1996), motor

learning (Turner & Desmurget, 2010) (Graybiel, 2005) (Grahna et al., 2009), cognition (Grahn et al., 2008), channeling information and modulation of motor parameters, and contribution to some non-motor aspects (like motor context, reinforcement etc.). However, the exact functional role and the underlying mechanism of the BG are yet to be unveiled.

Fig 1.1. Left figure: Location of basal ganglia in human brain *(image by Author - John Henkel, from the Food and Drug Administration}} |Source=Transfered from [http://en.wikipedia.org en.wikipedia] |Date=2006-08-31 (original upload)*. Middle and right figure: coronal view of human brain showing BG. Anterior slice (middle figure): striatum, globus pallidus (GPe and GPi). Posterior slice (right figure): subthalamic nucleus (STN), SN (substantia nigra). (*Permission is granted to copy, distribute and/or modify this document under the terms of the **GNU Free Documentation License**, Version 1.2 or any later version published by the Free Software Foundation*).

1.2. Basal Ganglia Functional Mechanism

The BG is a highly complex set of parallel and integrative networks (Haber, 2003) (fig 1.2). The classical basal ganglia (box and arrow) rate-models (Albin et al., 1989) (DeLong, 1990) simplify BG circuitry by emphasizing changes in discharge rates over relatively long periods of time, and by largely emphasizing direct and indirect STR to GPi pathways. The excitatory cortical inputs to STR stimulate the ‘direct’ monosynaptic and ‘indirect’ pathways by inhibiting and exciting the GPi respectively. The net reduced inhibitory output from GPi to the ventrolateral (VL) thalamus is thought to release thalamo-cortical activation. This model has limitations with

respect to explaining many lesion and DBS effects (Lozano et al., 1995) (Baron et al., 1996) (Leh et al., 2007). Additionally, although the models continue to expand at the expense of simplicity, they are arguably still restrictive and do not account for changes in patterned activity regularly occurring over 10's of milliseconds, and do not generally give comparable consideration to many potentially equally important basal ganglia projections. Depending upon the diffused nature of STN projection to the BG output nuclei, Mink and others suggest that the STN might be an equally critical BG input nuclei (Worbe et al., 2010) (Mink, 2003). STN includes 'hyperdirect' cortical-STN pathway to suggest an inhibitory center-surround organization for focusing action selection. Nambu put forward a dynamic model (Nambu, 2004), which extends Mink's space surround model in the temporal domain. According to this model, first the fast hyperdirect inhibitory pathway resets the network for further action, then the slightly slower direct excitatory pathway executes the signal, and finally the slowest indirect pathway acts to terminate the action. In addition to these models, SNc produces dopamine (DA) which controls the differential modulation of STR output by increasing the excitatory effect of the direct pathway (causing movement) and reducing the inhibitory effect of the indirect pathway (preventing full inhibition of movement) and thus helps maintain balance in striatal pathways in normal state (Hiromi et al., 2013). Also, it is well established that the STN forms a strong dual projection loop with GPe and GPi (Yoshinori et al., 2013). Furthermore, GPe, which receives dual inputs from STR and STN, in turn, not only projects to the STN forming an auto-stabilizing feedback loop, but projects directly to GPi, as well as to STR (Hanley & Bevan, 2000) (Bevan et al., 1998). Furthermore, Delong and Alexander describes the cortico-BG information transmission via parallel reciprocal circuits (those associated with same functions) projecting from different functional territories (Alexander et al., 1986). However, anatomical evidence

reveals non-reciprocal connections forming a wide integrative network which channels information between different functional

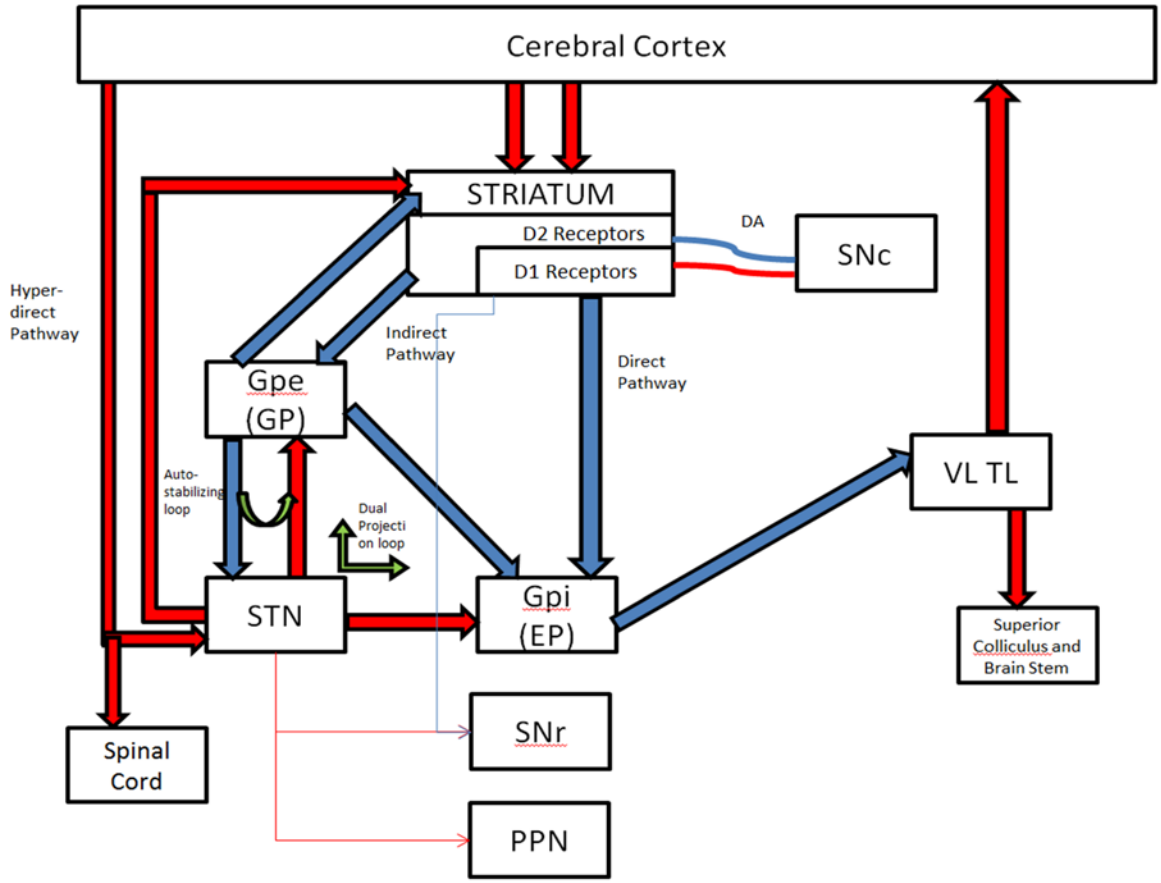

Fig 1.2. Basal ganglia-Thalamo-cortical motor circuitry. GP: Globus Pallidus, EP: Entopeduncular nucleus, VL: ventrolateral (pallidal receiving) thalamus, SNr: substantia nigra pars reticulate, SNc: substantia nigra Pars compacta. Red arrows = excitatory (glutamate) pathways, blue arrows = inhibitory (GABA) pathways. Blue curved lines = inhibitory effect of DA, Red curved lines = excitatory effect of DA

subdivisions of BG (Haber, 2003) (McFarland & Haber, 2002). Thus, in BG, different input components of information (like motor, limbic, and associative signals) influence the processing of each other. To add more to the BG complexity, the somatotopically organized BG nuclei tend to converge as compared to their cortical counterparts, i.e. the number of neurons representing each functional subdivision is reduced (Rivlin-Etzion, 2009). Based on this information, Bar-Gad

et al introduce a ‘reinforcement driven dimension reduction model’ (Bar-Gad et al., 2000a) suggesting compression of cortical information via DA modulation. Some recent work also reports disynaptic interface between BG and cerebellum as well. The cerbello-thalamo-straital pathway projects signals from deep cerebellum to STR (Hoshi et al., 2005). Additionally, STN projects cerebellum via pre-cerebellar nuclei of the brain stem (Boston et al., 2010). This portrays BG as a highly complex and interconnected information processing network. Loss or damage in any element of this network would disrupt the normal functioning of BG. This in turn relays abnormal signals to thalamocortical circuit resulting in motor dysfunction. Thus, each element in the above network has its own role in modulating the motor signal.

Additional BG models to explain motor control in BGTC circuit

The basis of the majority of models is combination of the detection of cortical contexts with the selection, modification, and integration of cortical inputs to generate the sequences of patterns. The above section describes some of the initial attempts used to model the functional mechanism of BG circuitry. The concept of ‘Direct-Indirect-Hyperdirect’ pathways and differential modulation of striatal output by DA explains the space surround (center facilitation- surround inhibition) model for action selection. Nambu then extends this model to temporal domain, explaining the sequence initiation, execution, and termination of ‘a single action’ (Nambu, 2004). Although, the above models provide an invaluable framework for conceptualizing basal ganglia connections, these rate-based models have major limitations. Instead, Gurney et al introduced the concept of selection pathway (similar feed-forward off center-on surround network) and an additional control pathway with synergistically complementary DA modulation (which regulates the selection pathway to ensure its effective operation) (Gurney et al., 2001)

(Gurney et al., 2001). Many researchers also consider the role of BG as not just mere selection of a particular action, but also in control of sequence of actions and learning (Turner & Desmurget, 2010; Turner & Desmurget, 2010). For a series of actions required to be executed in a particular sequence, the system may need external or internal cues to control the reward based signal flow (Terra et al., 2011). Beiser's model (Houk & Beiser, 1995) explains this through a series of encoding cortical inputs at the STR level. Although each MSN in STR receives about thousand afferents, only few of them get activated by an initial pattern of cortical activation due to the mesh of lateral inhibition. STR thus acts as a context detector; and the spatiotemporal pattern generated in STR accounts for the further modifications in the cortical pattern (Beiser & Houk, 1998). On the other hand, the model introduced by Berns, explains how BG produces action sequences, based on the assumption that the local working memory exists in the form of reciprocal connections between GPe and STN (Sejnowski, 1998). According to this model, the action selection takes place at the STR→GP projections based on a lateral inhibition by neighboring cells, and sequence learning is sensitive to the ratio of strength of STR↔nigral and STN↔GP learning loops. Another model, the Actor-Critic model is based on a reward based reinforcement of connections of actor (action execution) networks by a critic network. This accounts for the DA response and is mediated by direct and indirect pathways (Barto, 1995).

Other than anatomical connections and type (inhibitory-excitatory) of inputs, yet another important aspect considered during modeling is the type of information (i.e. the voltage features of discharge spikes and the discharge patterns associated with the information). It is not well understood how the motor information sent by different functional regions of the cortex is processed in the BG (Bar-Gad et al., 2000a). Additionally, another challenge is to associate the

firing pattern of a neuron with the type of information it is relaying. The challenge here is twofold; estimating the cause of a particular firing pattern and then evaluating the effect of altered firing pattern in the target nuclei and the network. Connolly describes coupling between MSN signals by relating the cortico-striatal projection signal features, trough and peak voltages, with the goal and boundary conditions (Burns, 1993 a). Similarly, Contreras models (Contreras-vidal, 1995) BG circuits as a 'go' signal relay for movement. The model calculates the reaction time and movement strength according to the difference between the target and the present position vector.

Lesion and motor disorder modeling helps in simulating additional controlled computation in the neural network and in exploring the theories of basal ganglia function. Berns et al. tested their learning model by introducing a model of a lesion in GP to observe the increase in STN gain (Sejnowski, 1998). The point process models (PPM) described by Saxena et al. investigate the physiological connections between different sites in GPe and GPi (Saxena, 2010). The GPi PPM generalize the firing rate of a 'Poisson process' based on the independent activity of neighboring neurons of the subpopulation, spiking history of the neuron itself, spiking history of the projecting GPe neurons, and the relative contribution of intrinsic and extrinsic factors (DBS). Rubin and McIntyre studied the downstream effects of parkinsonism in BG to establish its relationship with increased GPi output, increased synchrony, burst discharges, and oscillations (McIntyre & Wichmann, 2012).

1.3. Dystonia

Dystonia is a devastating condition characterized by ineffective, twisting movements, prolonged co-contractions and contorted postures (Geyer & Bressman, 2006) (Grosse et al., 2004) (Raike et al., 2005) (Yanagisawa & Goto, 1971). The neural mechanism behind dystonia is not yet fully understood. However, evidence suggests that it occurs due to abnormal discharge patterns in the BGTC circuitry. The dystonic state is characterized by loss of neural inhibition of unwanted contraction sustained in agonist-antagonist muscle pairs. The EMG burst in dystonia is sustained for 100-300 ms.

Various forms of dystonia have been reported based on anatomical distribution, age of onset, and etiology. Dystonia can be focal, multifocal, segmental, unilateral, or generalized based on its anatomical distribution in the body. If dystonia arises during or before adolescence, it spreads throughout the body, achieving a generalized state, causing severe twisting of trunk and limbs. However, if the symptoms begin at an older age, it remains localized. Inherited or sporadic cases of dystonia are called primary dystonia, while dystonia caused by stroke, drug effects, or is work related, then it is called secondary dystonia. There is no treatment to completely cure dystonia at present. However, treatment options like pharmacological, surgical and physical therapy are used frequently to reduce the severity of symptoms. Patients with severe dystonic symptoms, with no to minimal response to pharmacological treatments, can benefit from deep brain stimulation (DBS) of GPi. DBS effect on patients with primary dystonia shows fair success rate for improvement of dystonic symptoms. However, patients with secondary dystonia exhibit high variability in DBS results. This variability indicates involvement of different brain regions and pathology within multiple pathways causing secondary dystonia.

Fig 1.3. Examples of dystonia: (a) Dystonia in human being (*picture by James Heilman, MD (Own work) [CC BY-SA 3.0 (http://creativecommons.org/licenses/by-sa/3.0) or GFDL (http://www.gnu.org/copyleft/fdl.html)], via Wikimedia Commons*). (b) Dystonic Gunn rat. Rat's age is 18 days and was injected on day 16. Note the impaired righting reflex, contorted body and multiple co-contractions in limbs. (c) A dystonic lesioned rat. Note the hind limb extension of the contralateral side (more details on lesioned animal in Chapter 5).

GP, EP and STN under dystonia

Under pathology of dystonia, various BG nuclei behave abnormally and relay corrupted information to target nuclei. A common observation in various dystonias is that the GP (GPe) exhibits reduced neuronal discharge activity with abnormal bursts in both primates and rodents (Vitek et al., 1999) (Nambu et al., 2011) (Baron et al., 2011). Similar reduced firing rate and abnormal burst pattern is observed in EP (GPi) also (Lenz et al., 1998) (Merello et al., 2004) (Sanghera et al., 2003) (Zhuang et al., 2004). In STN, however, the firing pattern is also found to become more irregular and bursty but no clear change in firing rate was observed (Starr et al., 2005). Another most contrasting feature on pallidal firing pattern in dystonia is the level of synchrony found among their neuronal population during movement (Sharott et al., 2008) (Chen et al., 2009). This excessive oscillatory activity in GP and EP is also synchronized with the dystonic EMGs at 3-12 Hz i.e. the dystonia frequency (f_d). The preliminary results also show

synchronized pausing and bursting in GP and EP respectively during dystonic movement (Chaniary et al., 2008) (Baron et al., 2011). In summary, the pathology of dystonia causes drastic change in the firing pattern of BG nuclei accompanied by loss in their sub-population functional specificity (LOS) (Bar-Gad et al., 2011), which is reflected in their reorganized somatotopy. This pathologically can alter both spatial and temporal information when relayed back to motor cortex via the thalamus, leading to dystonic motor symptoms.

1.4. Dissertation Overview

The central purpose of this research was to study a common neurological movement disorder 'dystonia' as a model of motor control dysfunction, and to compare the related BG dysfunction to normal conditions. The objective of this study was twofold: improvement in the current recording-analysis techniques for neuronal data to ensure reliability of the results, and electrophysiological characterization of neurons found in BGTC circuitry. This would further lead to development of a more robust model of the BGTC circuitry explaining the mechanism of pathophysiology of disorders of BG. Based on the literature review and the preliminary studies, the principal hypothesis was that the BG is critical to programming normal movement, and that unless BG neurons can independently fire at precise times, abnormal movements will occur. In the case of dystonia, an additional hypothesis is that abnormal signaling patterns and increased neuronal synchrony leads to simultaneous or untimely activation of antagonistic muscles and undesired joints. These hypotheses were systematically tested using the following specific aims during the course of this study:-

Specific Aim 1: **Qualitatively evaluate the electrophysiological changes in basal ganglia nuclei, VL-thalamus and primary motor cortex in normal rats during limb movements.**

Specific Aim 2: **Define and relate the abnormal neuronal discharge pattern and motor symptoms in dystonic, lesioned, and spontaneously recovered dystonic rats.**

Specific Aim 3: **To interpret the information coded in the neuronal firing patterns in various nuclei and model the basal ganglia functionality.**

The first part of this project was to develop sophisticated and robust techniques to increase the reliability of the collected and analyzed data. Towards this aim, a modified head holder system was developed facilitating simultaneous multi-nuclei recording from large exposed brain area in an awake head restrained rat. Various geometrical orientations of the electrode manipulator were tested, and recording cannula spacers were designed to maximize number of recorded neurons from multiple nuclei. Sophisticated algorithms and GUIs were developed in MATLAB for spike detection-sorting-processing of multineuronal data recorded from seven-core electrodes (Chapter #2). A novel tri-component algorithm was developed for robust discrimination of neuronal firing patterns (Chapter #3). Statistical modeling and hot spot analysis of efficacy of DBS and ibotenic brain lesions was implemented (Chapter #4). Additionally, novel GP lesion based rat models were separately developed for parkinsonism and dystonia (Chapter #5). Thorough recording and analysis of the electrophysiological signals from normal and kernicterus dystonic rats were conducted utilizing above advancements. The neuronal populations in basal ganglia nuclei (GP, STN and EP; Chapter #4) and in recovered rats (Chapter #6) were characterized. The neuronal population in BG receiving thalamus (VL) and motor cortex (MC) (Chapter #7) were then systematically characterized. Finally a novel model of BGTC network accounting for GPi modulation of thalamic firing modes (Chapter #8) was proposed.

CHAPTER 2
ADVANCEMENTS IN MULTI-TARGET MULTI-UNIT

RECORDING SYSTEM

2.1. INTRODUCTION

This chapter describes the set of tools employed and developed in the lab to facilitate multi-target multi-neuronal recoding from a head restrained rat.

Simultaneous recording and analysis of multiple neurons from multiple targets in awake animals is an important tool for neuroscience. This capability allows characterization of the neuronal population and evaluation at the network level. There are many hardware as well as software limitations and challenges in this field that need to be resolved in order to get a convenient, reliable, and efficient system.

Many neuronal data gathered from live animals in this field are recorded from animals under ear bar restraint requiring anesthesia. The neuronal data under such anesthetized state does not represent the ideal baseline network activity, because many cortical and other inputs to the network nuclei are altered under anesthesia. On the other hand, recording from freely moving animals induces additional nondeterministic and confounding variables that, along with enhanced possibility of electrode drift, influence the output of the control studies. Recordings performed during awake head restrained conditions, therefore provides a more practical method to analyze neuronal behavior in steady state as well as during controlled movement. In this chapter, modifications to the previously developed stereotaxic device used for head restraint recording from awake rats are described. The head chamber used in the present study was redesigned to be considerably lighter and wider allowing easier targeting of a wide range of brain regions. This leads to the next challenge of this study, which was to develop an ‘electrode

tracking manipulation system' and develop strategies that can facilitate accurate targeting of motor territories in multiple regions. This includes spacers to redirect cannula and optimization of trajectories for targeting different nuclei. An additional goal for targeting strategies was to optimize that the number of tracks to maximize the amount of neuronal data collected while minimizing damage to the brain tissue. Fig 2.1 shows the damage caused by a single electrode track. Numerous electrode tracks can cause considerable damage to the tissue resulting in abnormal alterations in network activity and introducing additional variables in the control study.

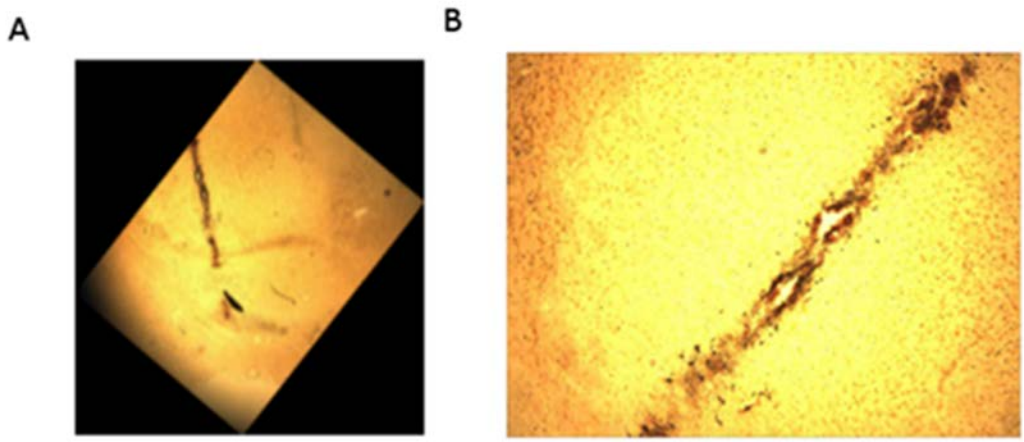

Fig 2.1. Light microscopic view of the silver stained brain slides indicating damage due to single heptode track. A. Track mark in thalamus, zona incerta and STN at magnified at 10X. B. Same track magnified at 20X.

Furthermore a MATLAB based application, Processing-Analysis-Modeling of Neuronal system, (**NeuroPAM**) was created. This application provides an additional *heptode* mode for data analysis. NeuroPAM provides exhaustive tools for analysis of continuous and point processes for rest and movement data. In addition, NeuroPAM provides tools for simulation of a wide variety

of spike firing patterns, including regular, irregular, and burst firing rasters. NeuroPAM also provides preliminary tools for simple modeling of neural network behavior.

2.2. METHODS AND OUTCOMES

2.2.1. Heptodes and data acquisition system

Toward more reliable and flexible spike data recording techniques, the neural laboratory is equipped with a sophisticated multichannel multicore microelectrodes called heptodes. Heptodes are seven core microelectrodes which are well suited for single unit isolation from multi-unit recordings. A specialized Thomas RECORDING Inc (TR; Fig 2.4B) seven heptode manipulator system was used, which provides a total of 49 recording sites/ channels. These 100µm thick multi-core electrodes impart less tissue damage than standard microelectrodes. Heptode recording enables reliable and easy separation of spikes originating from different neurons. Additionally, using specialized targeting strategies and a linear head electrode manipulator system (TR), simultaneously recording from more than two target nuclei was facilitated. The Alphaomega SnR data acquisition system ensures high resolution data recording from 64 channels. In this chapter, the aim was to develop sophisticated and robust spike sorting and analysis techniques for multiunit-multicore microelectrode recordings. The different recording sites of a heptode are situated at a slightly different distance with respect to the neuron. This induces an amplitude and temporal distinction between the channels. This feature can be used for efficient spike sorting. The ratio of spike amplitude of a cell on different heptode channels remain the same, while this ratio remains different for other cells.

2.2.2. Novel stereotaxic device for neuronal recording and customized multiple brain region targeting strategies

A novel stereotaxic device was introduced, which provides a safe way to record from a head restrained awake animal without any confounding effects of anesthesia. This involves a novel stereotaxic system designed and developed previously in the lab which facilitates recording from an awake head restrained rat. This system includes a stereotaxic positioner (fig 2.2A) and a head holder (fig 2.2B). Since, this assembly, provided limited exposure to the brain, more lateral and posterior targets were not accessible. Moreover targeting simultaneous multiple nuclei was difficult to achieve. To address these issues, the head holder was further modified to make it wider and lighter (fig 2.2C, D), allowing more exposed brain area for easy targeting and reduced mass load for the rat.

The principal aims of the intended neuronal studies in rats were to record from (i) one nuclei at a time; (ii) from three basal ganglia nuclei (EP, GP, STN) simultaneously; and (iii) from the principal output nucleus of the basal ganglia (EP), BG receiving thalamus (VL), and motor cortex (MC) simultaneously using 5-7 heptodes. Fig 2.3A indicates all the target regions used in this study. Different head configurations were analyzed and customized for simultaneous neural recordings from two or more different locations. Two cannula configurations for targeting aim (ii) and (iii) are shown in fig 2.3.B and C respectively. For multiple nuclei targeting, new customized spacers were designed to direct the electrode cannulas to predetermined coordinates. The linear spacer was designed to simultaneously target GP, STN, and EP (fig 2.4B). A second spacer to target outflow of the BGTC circuit, EP, VL, and MC is shown in fig 2.4C.

A

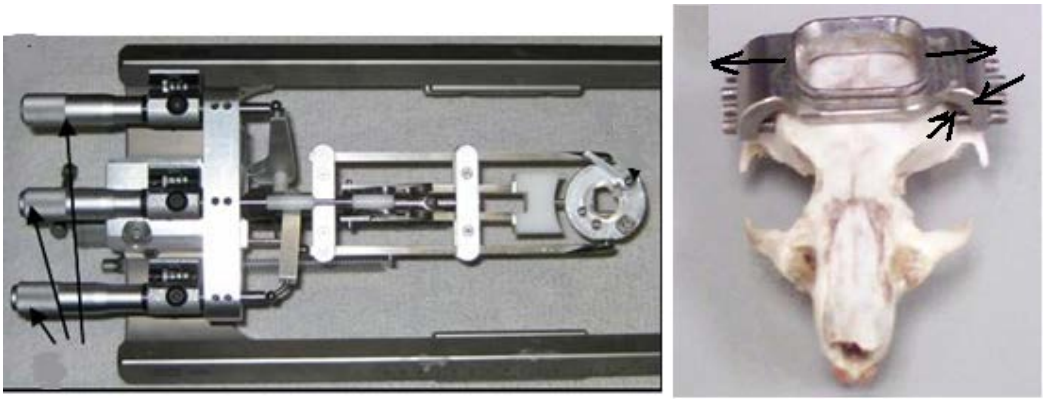

B

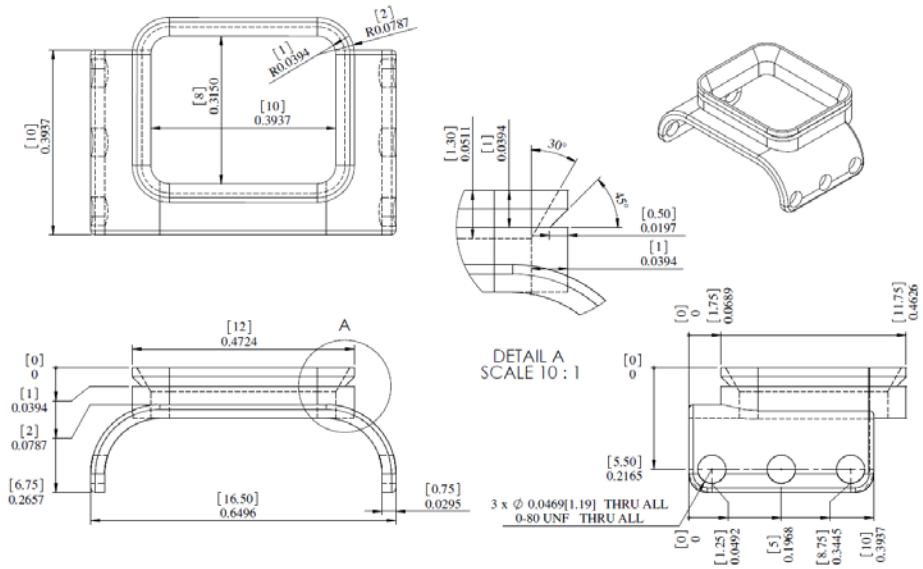

C

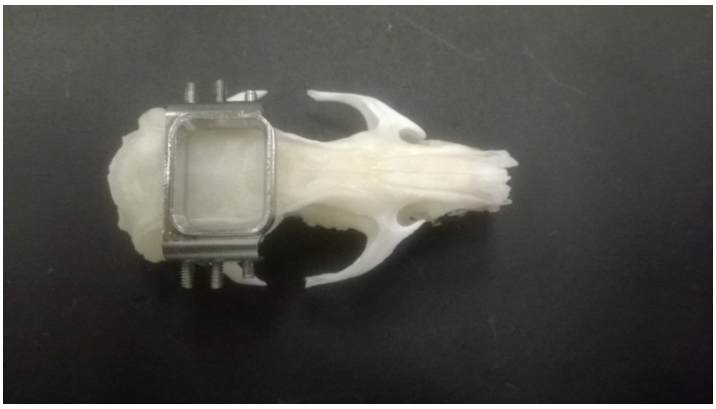

Fig 2.2. Stereotactic system for head restraint recoding from rats. **A.** Previously developed Stainless steel stereotaxic positioner system. And head fixture. C. modified design of the wider and lighter head holder (permission obtained from *Custom Design & Fabrication, Inc.)* D. Modified stainless steel head fixture for head restraint recording.

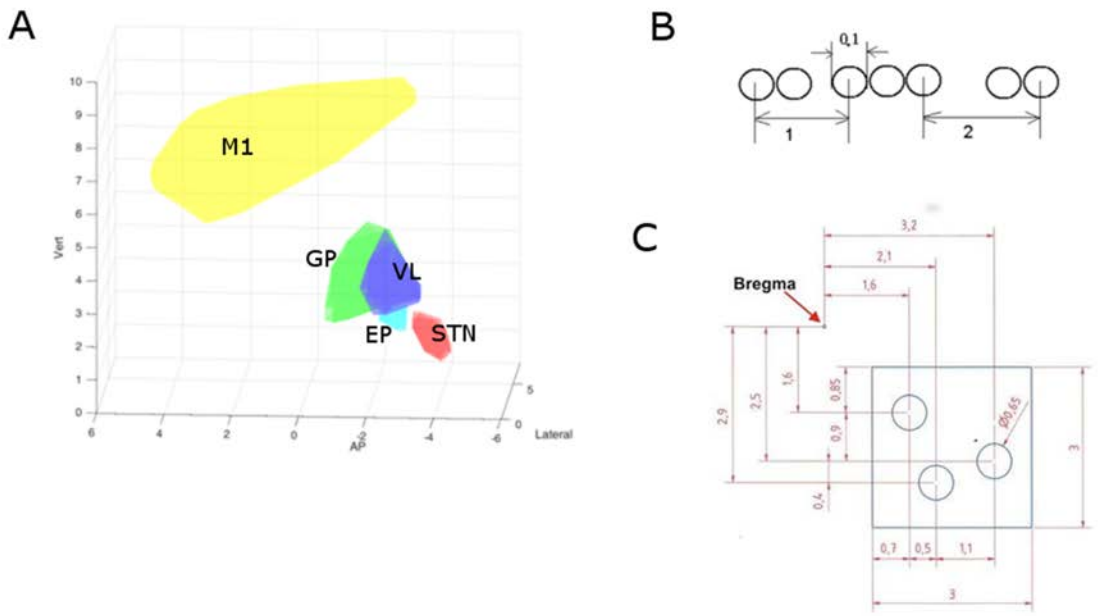

Fig 2.3. Multiple regions to target. (A) Target nuclei in 3d, MC: Motor cortex, GP: globus pallidus, STN: subthalamic nuclei, EP: entopenduncular nuclei, VL: ventrolateral thalamus. (B) Linear electrode arrangement for targeting GP, STN and EP. (C) 3d spacer configuration to target EP, VL and MC.

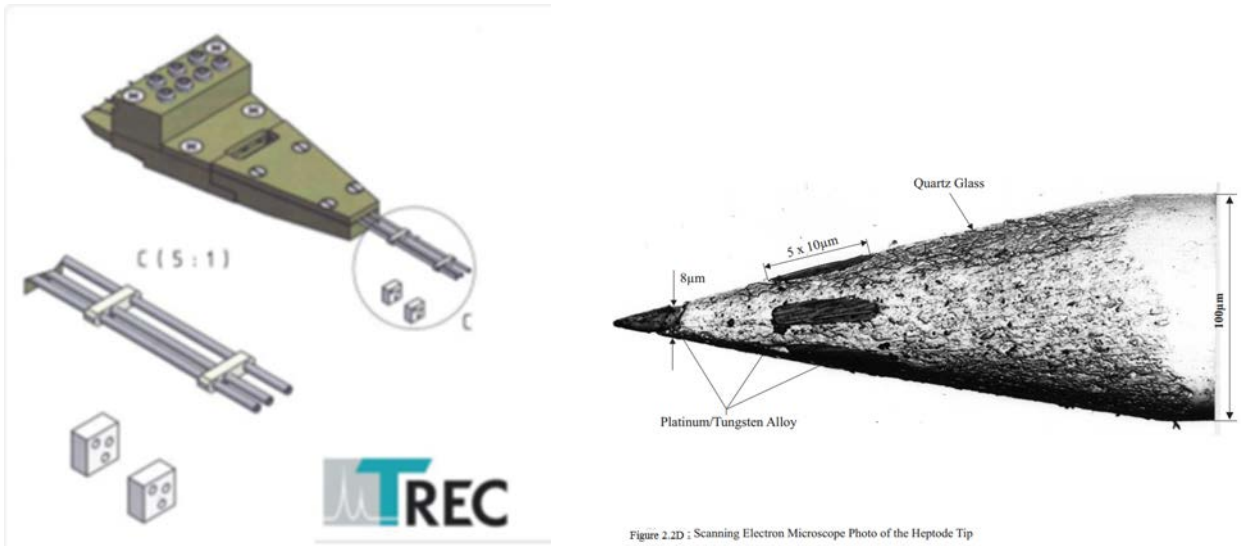

Fig 2.4. Modifications from Thomas recordings. (left) Thomas recording plastic spacers to direct the electrode cannula to different configurations. (right) Scanning Electrode microscope photo of the seven core heptode tip. (The pictures are published with permission of "Thomas RECORDING GmbH, Germany, www.ThomasRECORDING.com.)

The next step was to develop different strategies to accurately target the motor territories of two or more brain regions in the BG circuitry. In order to find the correct motor related regions in the nuclei, an extensive literature review was performed to assess the somatotopy and to determine the spatial coordinates for targeting. These coordinates were further confirmed by movement related alterations in neuronal responses during head restraint studies (extensive details are provided in Chapters 4, 5, and 7). The exact location of the electrode placement were cross confirmed by histology of rat's brain (details in Chapter 4 and 5). Finally, various geometrical and statistical techniques were used to estimate the appropriate head piece arrangement and the geometrical orientation of the electrode manipulator. Table 2.1 indicates coordinates of the targets in sagittal plane. Although, there are particular sagittal planes where all five nuclei can be observed, the motor territories of basal ganglia nuclei are located in the more lateral-posterior part of the nuclei.

Table 2.1. Locations of the targets in different sagittal planes

Lateral Plates	**EP (MGP)**	**STN**	**LGP**	**VL**	**CX (MC)**
L 1.40	--	--	--	B -2.0 to -3.4 (-2.6)	B 0.8 to -3.4 (-1.2)
L 1.90		B -3.7 to -4.5 (-4.0)	--	B -2.0 to -3.4 (-2.6)	B 3.0 to -0.6 (1.4)
L 2.40	B -2.3 to -3.1 (-2.6)	B -3.2 to - 4.4 (-3.6)	B -0.6 to - 1.4 (-1.0)	B - 2.0 to -3.0 (-2.5)	B 3.5 to 0.6 (2.6)
L 2.90	B -2.3 to - 3.1 (-2.6)	B -3.2 to -4.0 (-3.6)	B -0.8 to -1.7 (-1.3)		B 4.0 to 0.2 (2.2)
L 3.40	B -2.4 to - 3.1 (-2.5)		B -1.0 to -1.9 (-1.6)		B 3.4 to 1.0 (2.1)
L 3.90			B -1.2 to -2.1 (-1.6)		B 4.6 to 2.0 (3.4)
L4.20			B -1.8 to -3.0 (-2.4)		B 3.8 to 2.2 (3.4)
L 4.60			B -2.2 to -3.0 (-2.5)		B 3.2 to 2.8 (3.0)
L 1/2	L 2.9	L 2.4	L 3.4 / 3.9	L 1.9 c	L 1.4 (1.6)

Using polynomial curve fitting, three dimensional geometry, and minimum mean square error, the optimal orientation of the manipulator head piece, the entrance angles for the electrode were estimated (Table 2.2). Table 2.3 indicates optimal bregma points to target multiple nuclei. Table 2.4 indicates the optimal angles required to reach the targets, when the entrance coordinates (laterality and AP coordinates) are fixed.

Fig 2.5A shows the software application developed for online tracking of location of the electrode with respect to the target nuclei. Fig 2.5B shows the two trajectories to target various BG and thalamic nuclei. To maximize the number of neurons recorded from single nuclei, a concentric head configuration with 305 µm intra-electrode spacing was used.

Table: 2.2. Required angles to reach the targets:

	EP (MGP) (400 µm AP)	**STN (600 µm AP)**	**LGP (600 µm AP)**	**VL (800 µm AP)**	**CX (MC) (800 µm AP)**
L 1/2	**L 2.9**	**L 2.4**	**L 3.4 / 3.9**	**L 1.9**	L 1.4 (1.6)
B (0,0)	20º	25º	14º /14º	23º	45º
B (-1,0)	14º	20º	4-5º / 5º	16º	15º
B (0,-1)	17º	23º	10º /11º -12º	20º	30º
B (-1,-1)	10º	17º	4º /5º	14º	10º

Table 2.3: Bregma point for targeting GP, STN, EP, VL and MC

Electrode number	**Targeting GP, STN and EP** **Lateral 2.40 mm at 20°.** ***Separations: 0.6 mm (600 µm) and 0.4 mm (400 µm)***		**Targeting EP, VL and MC** **Lateral 2.40 mm at 20°** **Separations: 0.8mm (800 µm), 0.6 mm (600 µm) and 0.4 mm (400 µm)**	
	Location	**Target**	**Location**	**Target**
1	B (2.0)	GP1	B (3.0)	CX (MC) 1
2	B (1.4)	GP2	B (2.4)	CX (MC) 2
3	B (0.8)	EP1	B (1.6)	CX (MC) 3
4	B (0.4)	EP2	B (0.8)	EP1
5	B(-0.2)	STN1	B(0.4)	EP2
6	B(-0.8)	STN2	B(-0.2)	VL1
7	--	--	B (-0.6)	VL2

Table 2.4. Required angles to reach the targets:

	EP (MGP) (400 µm AP)	**VL (800 µm AP)**	**CX (MC) (800 µm AP)**
L 1/2	**L 2.9**	**L 1.9**	**L 1.4 (1.6)**
B (0,0)	20º	23º	45º
B (-1,0)	14º	16º	15º
B (0,-1)	17º	20º	30º
B (-1,-1)	10º	14º	10º

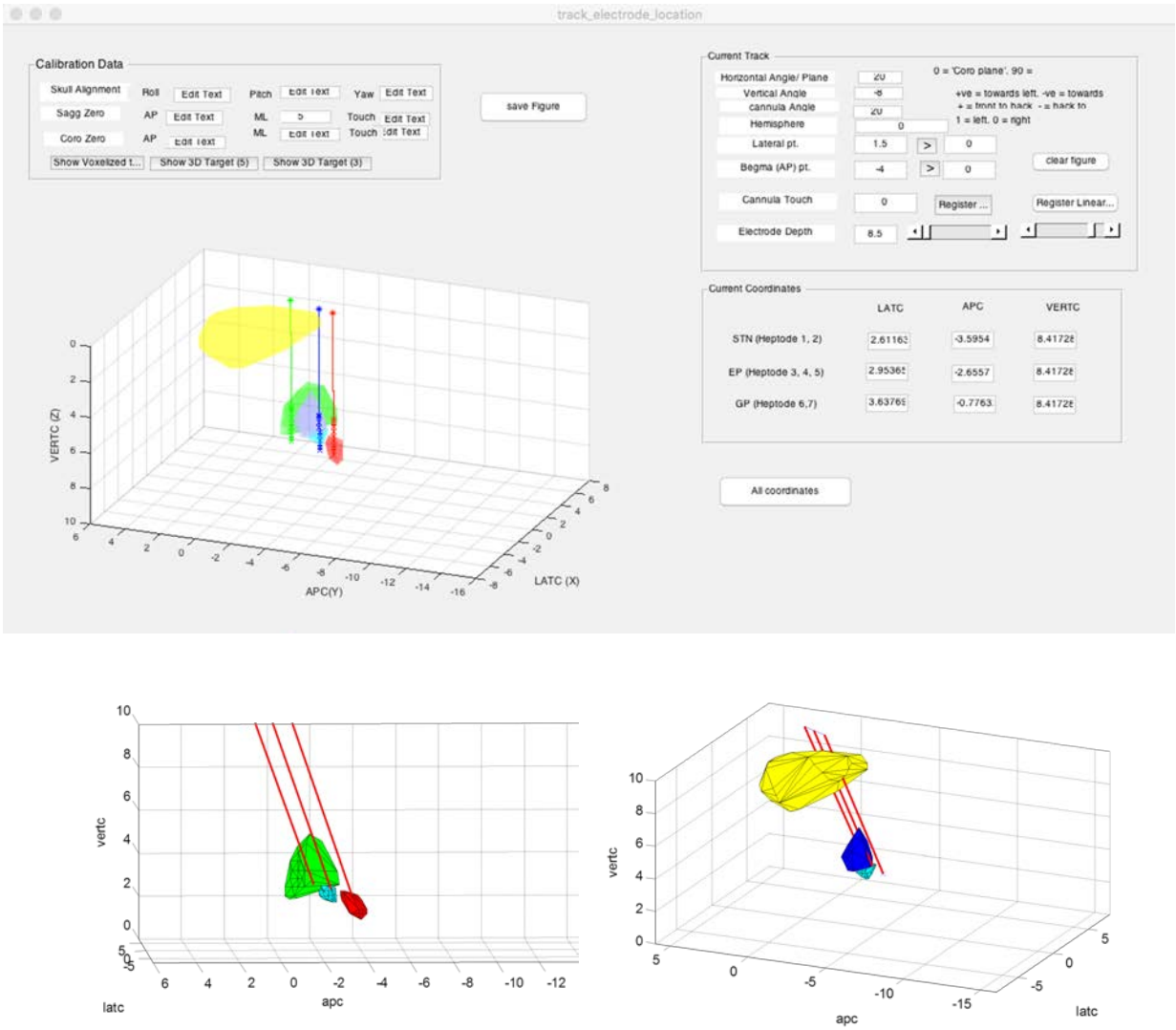

Fig 2.5. Strategies to target multiple brain regions simultaneously. (top) Electrode tracking software for online tracking of location of the electrode with respect to the target nuclei. (bottom) Tracking strategies.

2.2.3. Advanced multicore microelectrode spike sorting technique:

(a) Single channel spike detection and offline sorting

The discharge spikes were extracted online via manual amplitude thresholding of continuous signals during the recordings and saved for offline spike sorting (fig 2.5, 2.6) in MATLAB R2012a and Offline Sorter V 3.2.4, Plexon Inc. Only the signals with at least a 3:1 signal to noise ratio were considered for further analysis. Any invalid waveforms were manually removed before sorting. Generally, the first three principal components were used for spike sorting and clustering (fig 2.6 top row, second plot), but other waveform shape parameters (peak-to peak, waveform width, etc.) were also employed if needed. Final sorting included clustering into the 2D or 3D feature space using manual (K-means clustering, contours and waveform crossing method) and automated valley-seeking sorting techniques (fig 2.6 top row, third plot). This permitted excellent separation of waveforms collected from single or multiple electrodes (fig 2.6 top row, fourth plot). The separated waveforms were then inspected for potential loss of the neuron and for quality of neuronal isolation (fig 2.6 middle and bottom row). Any obvious artifacts in the signal were removed. Neuronal units were included only if a unit displayed a high quality of separation from background noise, the number of recorded potentials exceeded 300, and the activity was recorded for a minimum of 120 s. Neuronal units whose location could not be assured from the plotted tracks were excluded from all further analysis.

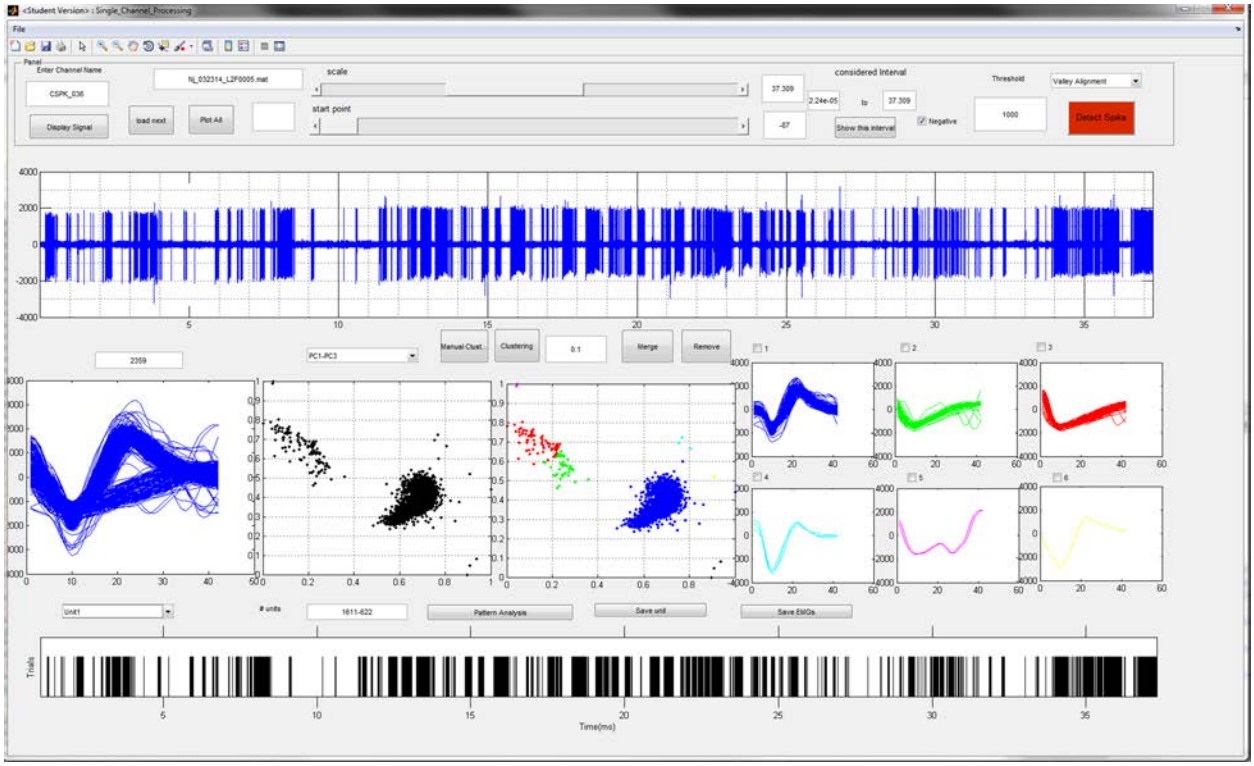

Fig 2.6. Software for spike sorting and pattern analysis of single channel recordings.

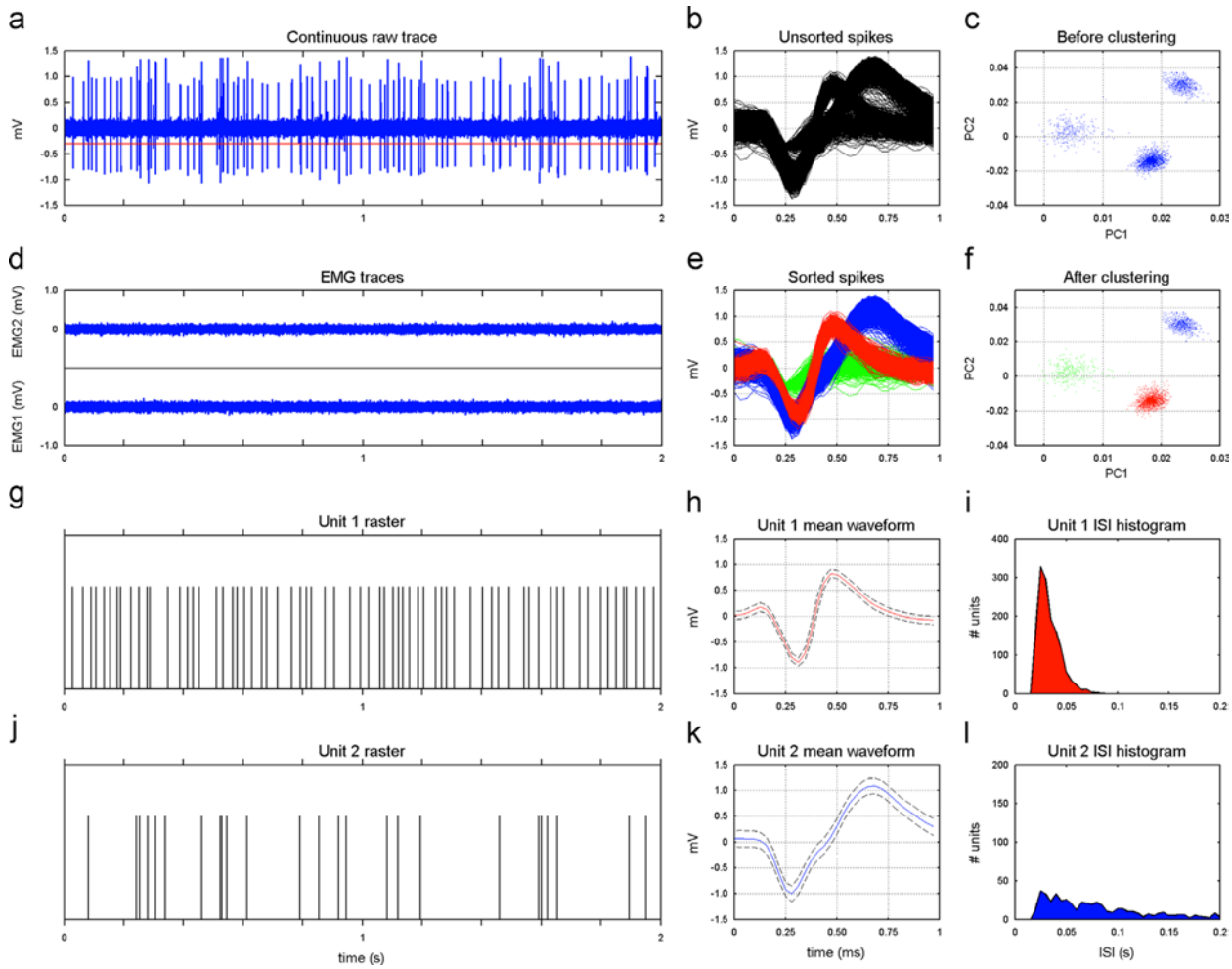

Fig. 2.7. An example of spike sorting and clustering from a recording in STN in a normal rat. Illustrated are raw traces (duration, 3 sec) of a portion of **(a)** continuously recorded extracellular neuronal signals from a single microelectrode with **(d)** simultaneously recorded EMGs from the gluteus superficialis (EMG1) and gluteus medius (EMG2) muscles. The red line in (a) indicates the threshold set for spike detection. **(b)** The unsorted spikes and **(c)** associated PC distribution are shown. **(e)** Valley-seeking sorting revealed two separate neurons, which **(f)** appear as two distinct clusters in the feature-space. The spike raster, mean waveform (with SDs), and ISI histogram of unit 1 **(g-i)** shows it to be a typical regular, moderate frequency neuron (mean rate: 35 spikes/sec, irregularity metric: 0.03), while unit 2 **(j-l)** can be seen to be a representative slower, irregular unit (mean rate: 10 spikes/sec, irregularity metric: 0.80). The fact that dissimilar neurons were regularly recorded simultaneously supports the presence of neuronal dichotomy in the investigated basal ganglia nuclei.

(b) Spike detection in heptode mode, waveform validation and alignment

Spikes were detected using manual amplitude thresholding in the heptode mode (fig 2.7). Whenever the signal from any channel exceeded the set threshold, the system would record data from all seven channels for a duration of 0.8 ms (32 samples for a signal with 40 KHz sampling

rate). Following a dead time of 0.2 ms, the detection algorithm continues until the last sample of the signal.

(c) Waveform parameters for feature space.

After waveform validation of the recorded action potentials, the spike data were then plotted in a multi-dimensional feature space with various waveform parameters at each coordinate (fig 2.9). For single core electrode recording, principal component analysis (PCA) is predominantly used for spike sorting. However, for multi-core electrodes such as with the heptode system, various other waveform parameters are also helpful. Spikes from the same neuron tend to cluster in separate groups in the feature space.

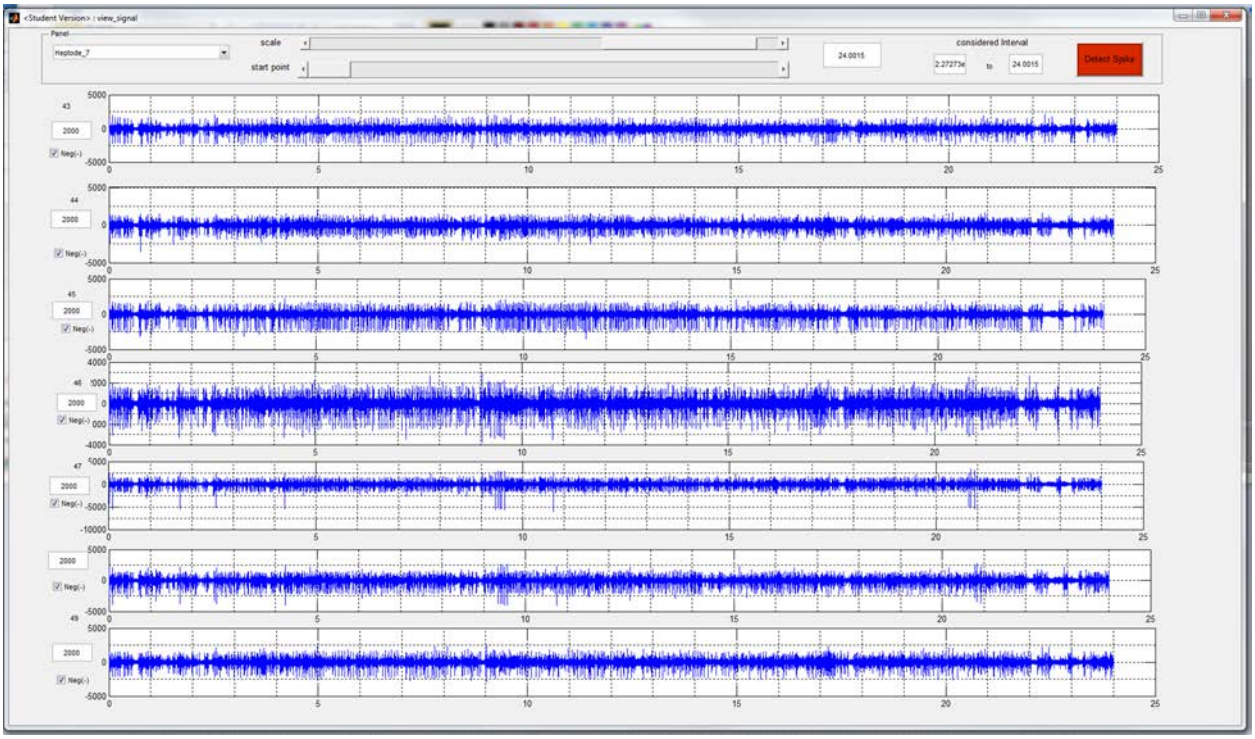

Fig 2.8. Display of high frequency spike signal from a seven channel heptode.

Some of the important waveform features used are as follows:-

1. Waveform Shape: *Principal component analysis (PCA)* is supposed to be best feature for sorting spikes from single core electrode. PCA is a dimensionality reduction technique that reduces the number of variables using orthogonal transformation. This method translates the origin and rotates the orthogonal axes, such that most of the variability in the data points lie along the single axis (called first principal component, PC1) and rest in PC2 and PC3. Variances reduces with the order of PCs, thus higher order PCs are noise. In context of spike sorting, the first three PCs holds more the 95% of the spike waveform shape information (i.e. variability among all the waveforms collected from an electrode site). Thus, when these components are plotted in a two or three dimensional feature space, the waveforms with similar shape tend to cluster together (Fig 2.8). For multicore mode, PCs of different channels can be plotted on different axes for sorting.

2. Waveform Size: Different neurons in the vicinity of the recording electrode tip manifest different amplitudes. This variation depends upon the distance between the neuron and electrode tip, properties of the surrounding fibers, and the membrane properties of the neuron itself. Changes in the size of the waveform can be then used to sort the different units. The most commonly used features are waveform peak (maximum amplitude above zero crossing), valley (minimum amplitude below zero crossing), Peak-valley (distance between peak and valley), spike width (temporal distance between the start and end of the waveform) and peak-valley full width at half maximum.

   For the multicore electrode mode, the same waveform size feature for each channel can be used on different axes for sorting. This feature increases the reliability of the spike sorting,

since the relative change in amplitude of a neuronal unit between adjacent electrode sites will show corresponding changes based on distance between the neuron and the sites.

3. Window discriminator: This technique is also used for online spike sorting. For waveforms that show clear distinction in amplitude and/or waveform shape. The user defines 2-4 windows within the waveform space, and all the waveforms are assigned to particular category if the waveform crosses all the user-defined windows.

4. Template Matching: A set of characteristics of waveform(s) are selected as the template(s). This is then followed by assigning the rest of the spikes using template matching.

5. Damping vector (DV): This sorting parameter considers properties like the volume conduction, attenuation effect and electrode impedance for spike sorting. This feature depends upon the position of electrode with respect to electrode channel/ site.

$$Spike\ waveform, v(n) = h(t) \times w(t) + E_n(t)$$

Where, h(t) is the damping vector and $E_n(t)$ is the error of nth electrode.

h(t) is obtained by minimizing energy of error of each electrode. This indicates position of target nuclei and then can be used as the feature for spike sorting in feature space. Different clusters are formed with DV at different neurons.

The damping vector technique is used for multi-core electrodes and use the fact that the ratio of two spikes amplitudes detected at adjacent electrodes remains constant for a neuronal unit and varies for different units. This feature helps in separation of overlapping spikes and treatment of burst spikes.

(d) Spike Clustering:

Once distinct clusters are produced in the feature space (fig 2.8 and fig 2.9) the clusters are then separated using different clustering techniques. For sorting various clustering techniques are used: manual, semi-automatic and automatic. The manual clustering technique includes user designed contours around each cluster. Any data points that lie within the contour boundaries are considered action potentials from the same neuronal unit. Semiautomatic techniques like K-mean clustering require the user to define number of clusters and the initial centers of the clusters. An iterative algorithm is then used to assign each waveform to one of the user-defined cluster centers, based on nearest Euclidian distance in the feature space. This is followed by the re-computation of the cluster centers based on the center of mass for the sorted data points. The re-computaion of cluster centers and the reassignment of the data points is repeated until no more waveform changes clusters. Details of the K-mean clustering can be found in Chapter 3. Some fully automatic clustering techniques are also utilized, which includes a mean shift clustering technique and a valley seeking technique which applies to inter-point distances to automatically determine the number of clusters and the cluster memberships.

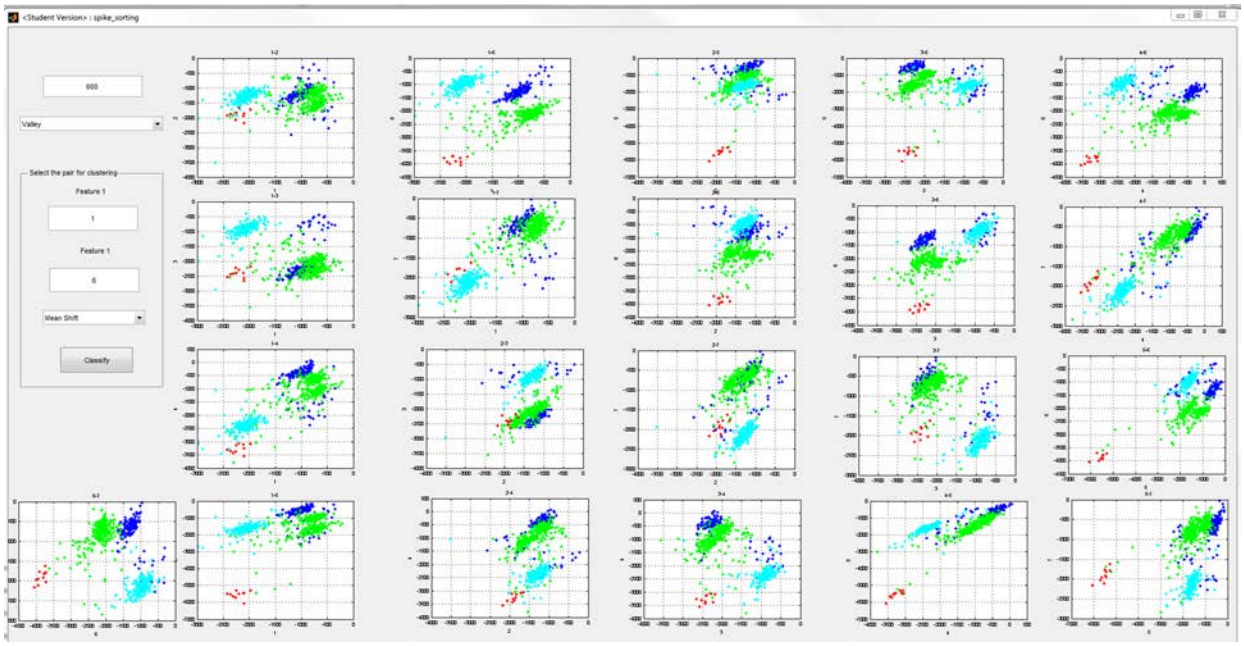

Fig 2.9. Feature space showing waveform valley data for different combinations of heptode channels. **A.** Waveform data from data from signals shown in fig 2.7. The figure also shows clustering technique used to sort the clusters (mean-shift).

(e) Post clustering cleaning and validation

Once all the waveforms are sorted, the validation of sorted spikes is important. Limitations of waveform sorting, level of background noise, electrode drifting with time due to movement, and change in neuronal baseline with varying conditions (lesion, movement, etc) could increase variability in the waveform shape as well as discontinuity in the temporal relationships. In order to overcome these errors, the waveforms are further validated and cleaned:-

(i) The waveforms with inter spike interval (ISI) is less than the absolute and relative refractory period of the neuron were invalidated.

(ii) The waveforms of a single unit are aligned and overlaid over each other. In case the width of the waveforms is abnormally wide, the spike sorting-clustering technique are rechecked or

repeated with stricter limitations (fig 2.10. bottom). The high variability in the waveform shapes of a single neuron indicates discontinuity or drifting of the electrodes or invalid sorting technique.

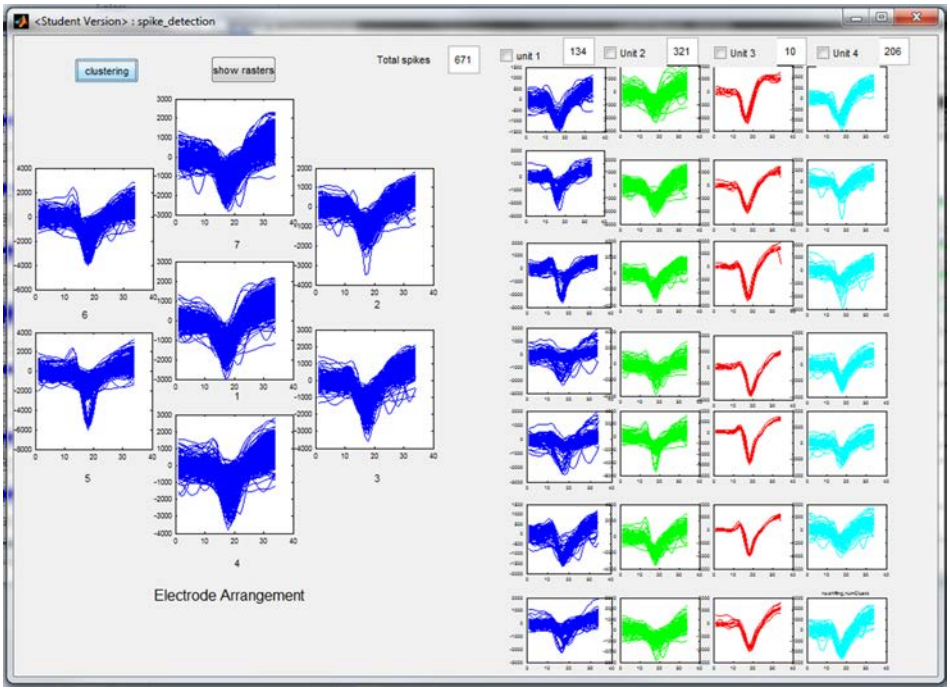

Fig 2.10. Output of the heptode mode spike detection (left) and post-clustering waveform groups.

2.3. CONCLUSION

The above results helped in accurate localization of the desired targets. Although the circumference of the heptodes are in the order of 100 μm, considering the small size of the rat's brain, any electrode track could produce considerable damage to the brain and ultimately will result in altered brain signals. Thus, in order to avoid collecting unreliable data, optimized targeting strategies need to be pre-planned to collect 'simultaneous data' with minimum tracks.

The track plans and orientation estimate in MATLAB helped target the desired regions with minimal error to reduce tissue damage as much as possible. The spike sorting technique is important for reliable estimation of the spike train, firing rate, and discharge pattern of the neurons. The NeuroPAM software implements many sophisticated techniques currently present in the field with additional modification and innovations particularly for seven core heptodes.

CHAPTER 3

A NOVEL TRI-COMPONENT SCHEME FOR CLASSIFYING NEURONAL DISCHARGE PATTERNS

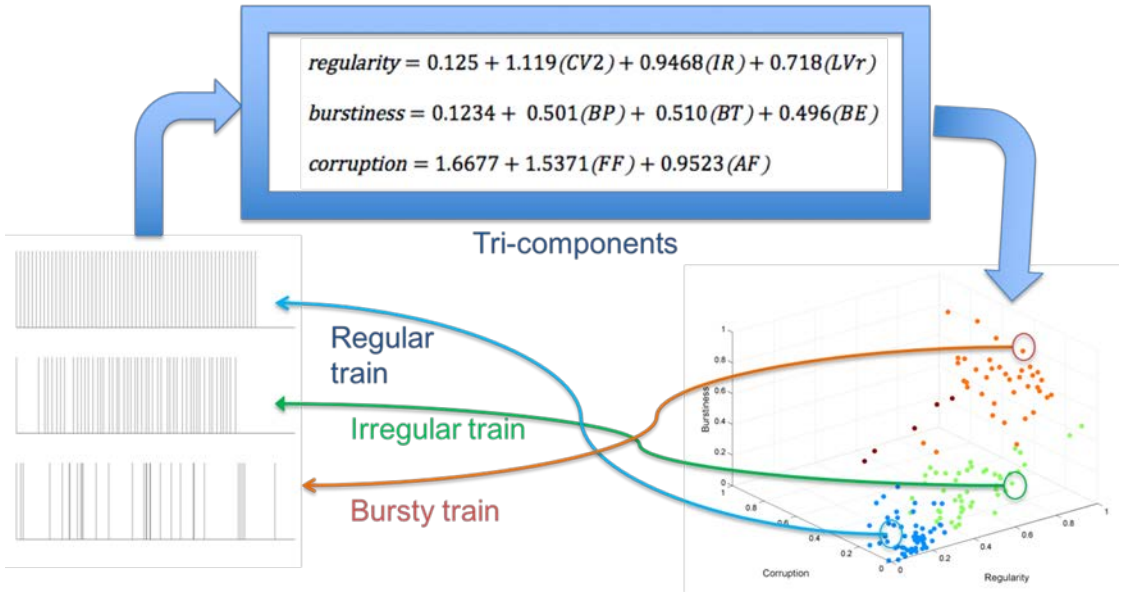

Fig 3.1. Tri-component scheme

3.1. INTRODUCTION

The pattern of neuronal spike trains has commonly been thought to be a largely stochastic process with information chiefly coded by the discharge rates. More recently however, increasingly, researchers have recognized that information is conveyed to a major extent by the temporal patterns of occurrence of discharges. As such, reliable objective metrics are needed to characterize neuronal discharge patterns to understand the intricate signaling between different nuclei. Such metrics must be able to effectively delineate three main features in the spike train: Poissonian irregularity, burstiness, and non-stationarity. Possionian irregularity indicates the level of randomness in spike occurrence, which can be modeled as Poisson point process.

Burstiness is the property of a spike train to intermittently increase in firing rate. Irregularity and burstiness are required to classify the spike pattern, while non-stationarity is needed to define the variability and extent of noise in the signal. Presently, no published analysis programs allow satisfactory categorization of the greatly varying neuronal discharge patterns encountered throughout the brain.

Limitations posed by subjective neuronal classification schemes (Kaneoke & Vitek, 1996) have led to the development of objective metrics. Since spike trains can be modeled as a Poisson process and defined by their inter-spike interval (ISI) distribution (Mitra & Bokil, 2007), several metrics have been introduced based on objective characterization of the ISI distribution. Coefficient of variation (CV) of ISI (Feng & Brown, 1999) (Christodoulou & Bugmann, 2001) is commonly used to describe the variability in discharge activity over the spike train, though it does not differentiate the various ISI patterns. Other metrics, including asymmetric index (AI), skewness (Sk) (Doane & Seward, 2011) and kurtosis (kr), have been used to define the shape of ISI histogram. Global measures, such as CV and AI, are however limited due to their sensitivity to discharge rate (Holt, et al., 1996) (Shinomoto, et al., 2009) and further, do not adequately account for non-stationary signals and corruptions in the spike train. To overcome these limitations, local variables have been developed, which compare adjacent ISIs, and as such, are relatively insensitive to rate variations. The local ISI metrics include CV2, the coefficient of variation for a sequence of two ISIs (Holt, et al., 1996) (Taube, 2010); IR, the difference of the log of two adjacent ISIs (Davies, et al., 2006); LV, local variation of ISIs (Shinomoto, et al., 2003); and LVr, a local variation parameter with refractory period information (Shinomoto, et al., 2009).

Another technique for measurement of regularity and burstiness is based on inspection of the shape and the location of peaks of the autocorrelation histogram (ACH) of spike trains (Paladini, et al., 2002; Perkel, et al., 1967). Markus et al. (2011) objectified this technique by quantifying the shape defining features of the ACH. However, the reliability is limited for non-oscillatory irregular trains and for non-stationary trains, including trains with varying underlying firing rates (Holt, et al., 1996). ACH techniques are limited in their ability to detect the multiple features which define burstiness. Because these classification techniques are robust and reliable for oscillatory spike trains, they were used for additional support for the initial visual subjective classifications. However since ACH classification parameters would not have strengthened the classification scheme, this methodology was not incorporate into the final objective algorithm.

Towards the present aim of defining robust metrics for characterizing diverse neuronal discharge patterns, available classification metrics on representative simulated spike trains and on a large data set of extracellular neuronal recordings from the primary motor cortex (MC), several basal ganglia nuclei, hippocampus, and thalamus in normal and dystonic rats were extensively tested. To account for non-stationarity in spike trains, Fano factor (FF) (Eden & Kramer, 2010) (DeWeese, et al., 2003) and Allan factor (AF) (Gaudry & Reinagel, July 25, 2007) were also assessed, which estimate spike count variability and provide additional measures of the burstiness of the spike train (Anteneodoa, et al., June 12, 2010). Since FF and AF are sensitive to Poissonian noise and to across trial variability (Churchland, et al., 2010), these metrics are able to detect local variations in pattern or rate. Two additional novel metrics, post spike suppression (PSP) (Benhamou, et al., 2012) and residual metrics (Maimon & Assad, 2009) were also

assessed, but were found not to be particularly useful. Because current metrics, including CV, LVr, and density histogram (Leblois, et al., 2010), were also inadequate for delineating burstiness, a new burst discrimination metric was developed. In the prior study (Baron, et al., 2011), reliable burst detection parameters for the customizable interval method (Plexon Inc. Neuroexplorer MaxInterval Method) were established. It was also determined that other popularized burst detection metrics, including the Poisson surprise method (Legéndy & Salcman, 1985) (Kaneoke & Vitek, 1996), were unreliable. The burst discrimination metric introduced here first delineates bursts in the spike train using the interval method and then defines the burstiness of the spike train based on burst parameters (‘burst percentage’ (BP), ‘burst tendency’ (BT), and ‘burst entropy’ (BE)).

It was establish here that individual metrics cannot reliably classify diverse neuronal discharge patterns. Therefore, a novel tri-component classification scheme was developed based on weighting combinations of desirable metrics using multiple metric optimization (MMO) and feature space clustering. Furthermore, transitions from regular to irregular discharge firing and form non-bursty to bursty lack clear unique designations. Therefore, rather than defining specific threshold cut-offs, this issue was obviated by utilizing multiple metrics to initially approximate the relevant features of the spike trains and applied then to multidimensional semi-supervised clustering to finalize the classifications of the spike trains. The comprehensive tri-component classification methodology is demonstrated here to dependably classify neuronal spike trains from diverse regions of the brain in the normal and in a representative diseased state.

3.2.METHODS

3.2.1. Delineation of bursts and development of novel burstiness metrics

As mentioned in the introduction, after determining from the simulations that available metrics could not adequately delineate burstiness, three new burstiness metrics: 'BP', 'BT', and 'BE' were developed. These new metrics, as well as the parameters chosen to define neuronal bursts using the interval method, are detailed below:

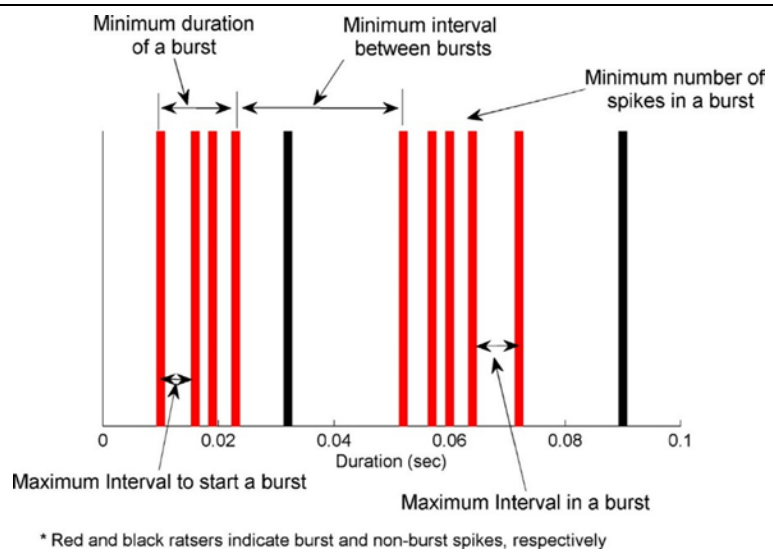

Fig 3.2. Parameters to delineate burst.

3.2.1.1. Detection of bursts using the interval method:

The interval method (Chen, et al., 2009) (Plexon Inc. Neuroexplorer MaxInterval Method) incorporates five definable parameters to delineate individual bursts (fig 3.2). Based on previous extensive visual inspection of spike trains in rats, values for each of these parameters were chosen and subsequently modified until they proved to be highly reliable in delineating individual bursts in the spike train (Baron, et al., 2011). The final derived values are as follows: max. interval to start a burst = 6 ms, max. inter-spike interval in a burst = 9 ms, min. interval

between bursts = 20 ms, min. burst duration = 5 ms, and min. number of spikes in a burst = 3 (fig 3.2). Using these parameters, the interval method was demonstrated to provide superior detection of bursts compared with the also popular Poisson surprise method (Legéndy & Salcman, 1985) (Kaneoke & Vitek, 1996).

3.2.1.2. Novel metrics to estimate burstiness:

(i) Burst percentage (BP): percentage of spikes in bursts:

$$BP = \frac{total\ number\ of\ spikes\ in\ bursts}{total\ number\ of\ spikes} \qquad \text{EQ (3.1)}$$

(ii) Burst tendency (BT): tendency to discharge in bursts versus in single spikes or doublets:

$$BT = \frac{number\ of\ burst\ events}{total\ number\ of\ spikes} \qquad \text{EQ (3.2)}$$

[0: non-bursty to 1: max. bursty]

(iii) Burst entropy (BE): measures the quantity of information, which is conveyed by the temporal sequence of burst events within the spike train. (Strong, et al., 1997). According to information theory, the information content of series of events (e.g., burst events) can be estimated using Shannon entropy (Shannon, 1948) (Borst & Theunissen, 1999) by the following formula:

$$BE = -\sum_{b=1}^{k} f_b \log_2 \frac{f_b}{l} \qquad \text{EQ (3.3)}$$

where, f_b = normalized burst count in b^{th} window, l = length of window, k = total number of windows

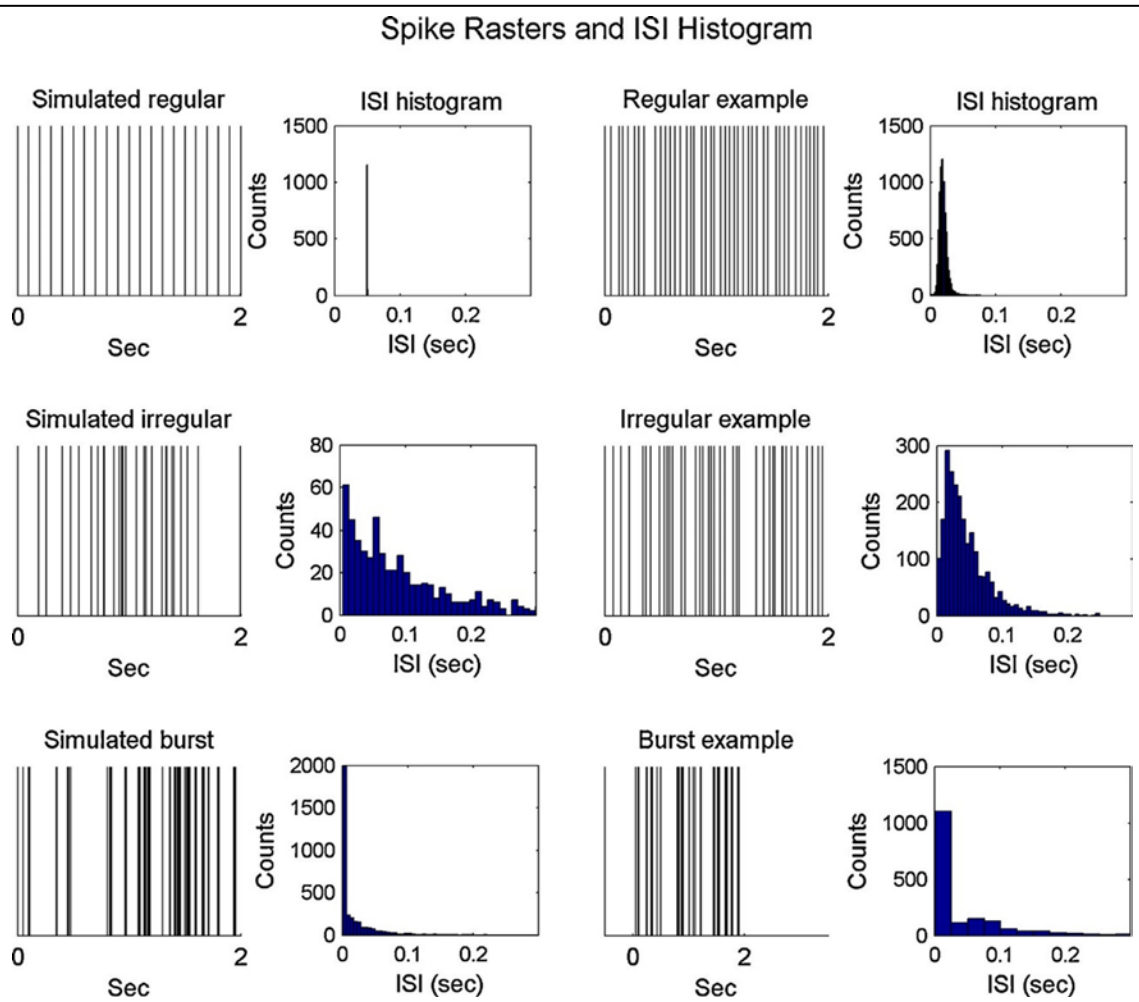

Fig. 3.3. Spike rasters and ISI histograms of the three principal spike train patterns. Examples of the standard simulated spike trains (first column) and extracellular neuronal recordings (third column) for the three principal spike train patterns are shown, along with their corresponding ISI histograms. The ISI histogram of the simulated regular standard train is a straight line (since all of the ISI's are equally spaced), while that of regular, tonic discharging neurons are narrow unimodal. The ISI histograms of irregular trains (simulated and neuronal) are skewed, generally with a late trailing tail, while burst trains are largely bimodal, with an early short interval peak.

3.2.2. Testing of objective metrics on simulated data sets.

Although many of the aspects of their performance were either already well-established or predictable, objective metrics on simulated data was systematically tested. For consistency, each simulated spike train was generated for 60 s in duration. Any simulated spikes occurring within the designated absolute natural neuronal refractory period (2 ms) (Heeger, 2000) (Anon., 2012) were rejected. Refer to the appendix for details on the methods used to generate the simulated spike trains and for simulation examples.

Stationary rate. Performance of each metric was first assessed on 10 spike train iterations (mean firing rate = 50 Hz) of each of the three principal basic firing patterns: 1) an equally spaced regular spike train, 2) a Poissonian irregular train, and 3) a third order (i.e., three spikes per burst) burst train (fig 3.3). The performance of each metric was assessed from its ability to assign distinct values to the three sets of examples of the basic firing patterns, as determined by the non-parametric Kruskal-Wallis test.

Varying frequency. The influence of spike rate on individual metrics was assessed by simulating the three basic patterns of discharge activity while varying the mean spike frequencies in 10 Hz increments from 1 to 101 Hz (10 iterations for each of the 11 frequencies for each of the three patterns, total 330 trains). Metrics which showed excessive firing rate sensitivity preventing adequate pattern discrimination, based on the Kruskal-Wallis test, were rejected from further consideration. Subsequently, Tukey-Kramer multiple comparison tests (MATLAB function:

multcompare) were run on each accepted metric to determine which pairs of the patterned groups (regular, irregular, and bursty) were specifically well discriminated.

Varying irregularity. To assess a representative spectrum of varying spike train regularity, a continuum of spike trains was simulated from very irregular to regular spiking. The present trains were generated by randomly generating ISIs from a gamma distribution by varying its shape parameter (κ) while adjusting the scale parameter to maintain the desired mean rate (Miura, et al., 2006) (Miura, et al., 2007) (Maimon & Assad, 2009). Using each of the 11 frequencies tested above (1:10:101), 12 κ levels were generated (0.25, 0.5, 1, 4, 8, 16, 32, 64, 128, 256, 512 and 1024) for 10 iterations each for a total of 1320 trains. Correlation coefficient (MATLAB function: corrcoef) was then used to assess the ability of individual metrics to define the irregularity in the spike train.

Varying burstiness: The following representative burst train scenarios were simulated: 1) 11 burst trains with a Poissonian background irregularity and varying frequencies (1:10:101), 2) 11 burst trains with similar burst spike arrangements and varying frequencies, 3) 11 burst trains with a similar oscillatory background and varying frequencies, 4) 8 burst trains with varying mean burst order (BO; spikes per burst: 1-8), 5) 8 burst trains with varying inter-burst events and similar timing and characteristics of the bursts, and 6) 8 burst trains with varying burst percentages (total number of spikes in bursts/ total number of spikes, 10%-60%). Each burst train here was ranked on the basis of total burst content (as defined by burst events/total events) predetermined during programming of the burst-generator. Correlation coefficients between each

metric value and the different programmed burst content were then used to determine the ability of individual metrics to delineate the level of burstiness of the trains.

Non-stationarity and noise. Non-stationary and corrupt signals were subsequently generated by randomly varying the firing rate and pattern throughout the simulation by randomly introducing events from another pattern (for instance, corrupting a Poissonian spike train by randomly introducing 10-50% epochs of burst events). One hundred different simulated non-stationary and corruption trains (no corruption, regularity variations, rate variation, burst corruption) were then assessed here for each of the three discharge patterns (regular, irregular and bursty). The Kruskal-Wallis test and the Tukey-Kramer multiple comparison test were then used to estimate the extent to which individual metrics could still reliably differentiate between the three basic spike patterns in the face of the imposed interferences in the signal.

Each of the simulate spike trains were also visually inspected for confirmation of objective classifications. Such features as linearity between consecutive ISIs, clustering of spikes, and inconsistencies in pattern along the length of the train were considered (Martinson, et al., 1997). Additionally, the shapes of each corresponding ISI histogram and ACH were inspected to verify the accuracy of the initial subjective classifications. A characteristic unimodal narrow ISI histogram curve indicates a regular train, while a skewed long tail histogram indicates an irregular train. For burst trains, ISI histograms show bimodal peaks, while a central peak in the ACH correspondingly signifies a burst train.

Most of the ISI based metrics (CV and local variables, CV2, IR, LV and LVr) measure normalized dispersion in the ISI distribution, thereby generating values of ~1 for Poissonian, < 1 for regular, and > 1 for bursty and non-stationary trains. Similarly, FF values are ~ 1 for Poissonian, < 1 for sub-Poissonian, and > 1 for super-Poissonian trains. AI (mode/mean ISI) is equal to one when an ISI histogram fits a Gaussian distribution. Kr of a standard normal ISI distribution is 3. A positive value of Kr indicates a peak and a negative value indicating a flat distribution. Sk is zero for a symmetric ISI distribution, with negative and positive values indicating leftward and positive skewedness, respectively. The shape parameter of the Gamma distribution 'k' is equal to 1 for an exponential distribution that indicates a Poisson process, while larger k values indicate increasing regularity. Threshold levels for classification of the trains was set for each of the metrics based on comprehensive comparison of their outputs and classifications derived from visual inspection. For example, the following final criteria was established for CV and the local variables: regular < 0.66, Poissonian irregular = 0.66-1.2, and bursty and non-stationary > 1.2. Similarly, for FF, the criteria were set as: regular < 0.52, Poissonian irregular = 0.52-1.51, and bursty and non-stationary > 1.51. For AI, the measurable criteria was set as: regular > 0.80, irregular 0.3-0.8, and < 0.3 bursty.

3.2.3. Multiple metric optimization

Based on the results of the simulations, it is affirmed that combinations of metrics are required to adequately characterize spike trains into the desired categories. After rejecting inadequate metrics, each of the chosen metrics was assigned to its relevant category: regularity, burstiness, or corruption. Then for each of these three categories, proxy metrics, combining and weighting

individual metrics, were derived using multiple metric optimization (MMO) based on linear regression (Shah, 2009).

(i) Each of the three proxy metrics was formulated to best define the corresponding feature of spike trains. The training datasets for MMO of each metric was obtained from a subset of the above data pool, with independent control of the corresponding feature. For instance, for the regularity metric, a total 168 spike trains were generated by varying the rate and regularity levels of the train (Appendix) were utilized. Since the shape parameter κ controls the regularity level of a train, it was used as the response variable for the regression. Similarly, for the burstiness and corruption metrics, the trains simulated by varying the total burst percentage (n = 140 trains) or degree of corruption in the train (n = 90 trains), respectively, were used for regression with burst percentage and corruption percentage as the response variables, respectively (Appendix).

(ii) Some metrics tend to generate abnormally high values for particular spike trains, for example, those with super-Poissonian structures. Since the maximum values of these metrics still indicate a super-Poissonian feature even after excluding these outliers, 95% winsorization was applied to reduce the difference between the extreme outliers and the second largest value in the dataset. Winsorization is the transformation of data by limiting extreme values to reduce the effect of possible unauthentic outliers. Subsequently, to highlight the difference between regular and non-regular and burty and nonbursty metric values, maximum-minimum normalization was carried out.

This normalization permits reliable comparisons between the values generated from different metrics and integrates the chosen sets into single optimized metrics.

(iii) To estimate the coefficients of the new proxy metrics, generalized linear model (GLM) regression (MATLAB function '*glmfit*') on the training datasets (step i above) was applied. The response variable was assumed to be normally distributed. The significance of the regression coefficients was estimated by dividing the estimated weights by the standard deviation of the estimate (α =0.05).

Subsequently, the reliability of the proxy metrics will be cross-validated based on their performance separately on simulated data and recorded neuronal data. The simulated test data set here consist of 600 spike trains generated by varying regularity level, mean firing rate or various burst parameters in the three principal spike train; 200 different spike trains corrupted with 10% corruption; and 200 spike trains corrupted with 20% corruption. Similarly, for the real test dataset, neuronal spike trains (n = 147), recorded from the globus pallidus (GP, rodent equivalent of GP externa, entopeduncular nucleus (EP, rodent equivalent of GP internus), subthalamic nucleus (STN), MC, hippocampus, and thalamus in 10 head restrained, unsedated normal and dystonic rats were used.

3.2.4. Neurophysiological recordings

On the day of recording, the rat's head was immobilized by clamping a custom stainless steel head fixture into a custom stereotaxic positioner (Chaniary, et al., 2011). Inhalation anesthesia (isofluorane 2-2.5%) was briefly delivered and a 3.5 mm burr hole (2 mm caudal, 1.5 mm lateral

to the bregma) was drilled into the skull exposing the underlying duramater. After 30 min., allowing for full recovery from effects of anesthesia, neuronal recording sessions were initiated. A mini-xyz-manipulator or an Eckhorn heptode manipulator (both from Thomas Recording, Giese, Germany) was mounted onto a Kopf stereotactic arm and single-unit extracellular activity was recorded using ultra-fine 100 μm Thomas Recording microelectrodes. Each nucleus was readily identified by its characteristic neuronal firing patterns. The location and firing patterns of neurons and the borders of encountered nuclei along each microelectrode track were plotted with the aid of superimposable transparencies generated from sections of a Paxinos and Watson atlas (Paxinos & Watson, 2007). The locations of microelectrode tracts were later confirmed histologically from silver-stained sections. Neuronal spike activity was collected for a minimum of 120 sec at a sampling rate of 40 kHz and was amplified and band pass filtered (gain = 50, bandwidth 0.07-8 kHz) using Sort Client (Plexon Inc., Dallas, TX). The quality of neuronal isolation was continuously monitored online using Sort Client. All experiments were approved and monitored by the McGuire Veterans Affairs Institutional Animal Care and Use Committee (IACUC) and performed in accordance with regulatory guidelines.

3.2.5. Offline analysis and spike sorting

All stored spike data were analyzed offline using Offline Sorter (Plexon Inc.) and MATLAB (Mathwork Inc. version 7.14). Recording epics with movement related artifacts were removed. For each data set, the 3-D feature space based on the Principal Component Analysis (PCA) of the waveforms was visualized and individual units were sorted into distinct clusters using a combination of automated (valley-seeking) and manual (K-means clustering, contours and waveform crossing method) sorting techniques. The individual waveforms of separated clusters

were then inspected for potential loss of the neuronal signal and any artifacts in the signal were removed. Neuronal recordings were accepted only if a unit had more than 300 discharge potentials and showed high quality separation from background noise and from other units. The timestamps of the selected spike trains were saved for further analysis.

3.2.6. Tri-component and subjective neuronal classification

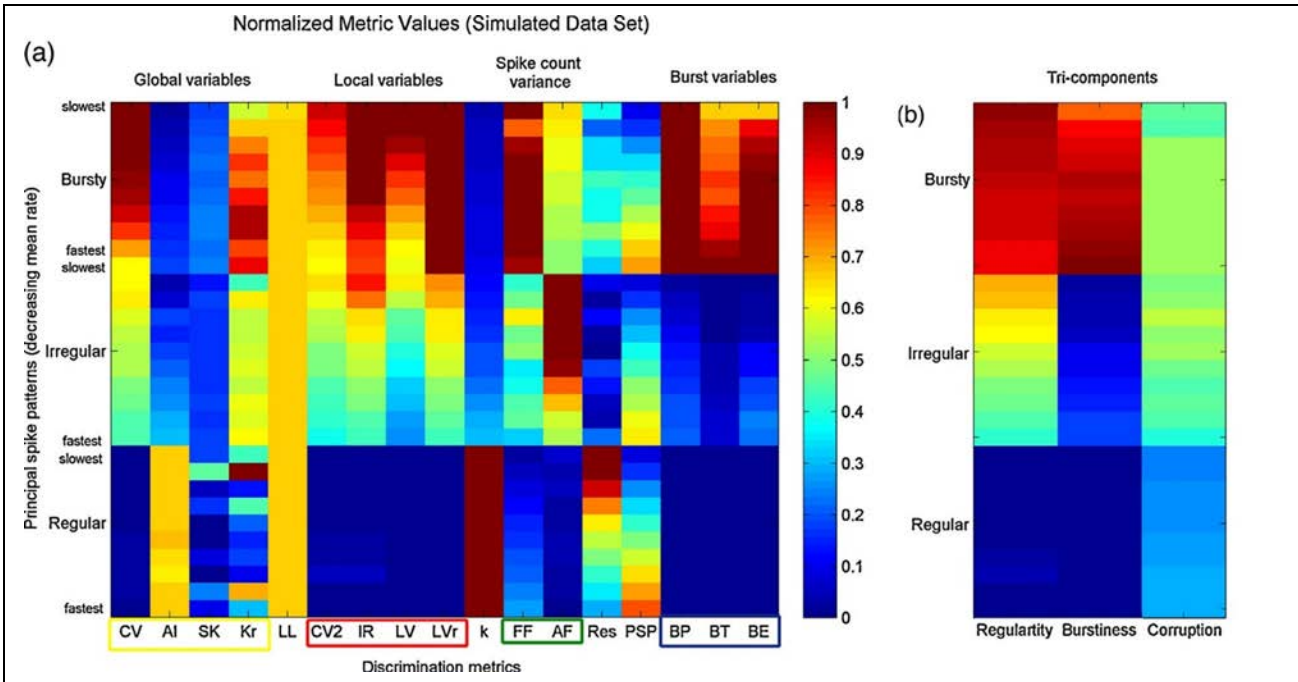

Fig. 3.4. Normalized color coded metric values derived from simulated spike trains for the three basic firing patterns (regular, irregular and bursty), with varying mean firing rates. (a) Performance of analyzed objective metrics show variable quality discrimination of the three principal spike patterns. (b) The distinct regularity and burstiness values of the new metrics indicate their superior discrimination, regardless of rate, while the consistently low corruption values for the simulated non-corrupt trains indicate the reliability of the corruption metric.

Each recorded neuronal spike train was plotted in a three dimensional feature space with the axes representing the three proxy metrics (irregularity, burstiness and corruption). Subsequently, the unsupervised learning algorithm K-mean clustering (MacQueen, 1967) (Amorim, 2011) was used to classify the spike trains into regular tonic, irregular, and bursty, and non-stationary based

on the nearest centroid. The simulated standard spike trains would serve as the initial group centroids for this clustering. After assigning all the recorded spike data points to the nearest centroid, the new positions of the cluster centroids were recalculated. The data point assignments and centroid recalculations would then be repeated until the centroids were fixed at their final positions.

Each of the recorded neuronal spike trains were also subjectively classified by extensive visual inspection of their complete spike trains as described above for the subjective classifications of the simulated trains (refer to Section 2.2). For the occasional units with conflicting classifications, the spike trains were re-inspected, and if still uncertain, such spike trains were rejected from further analysis. The final subjective classifications were designated as the gold standard for purposes of cross-validating the tri-component classifier.

3.2.7. Data processing and statistical analysis

Neuroexplorer and Offline Sorter (Plexon Inc.) were used for preliminary data processing, spike sorting and analyses. MATLAB (Mathwork Inc., version R2012A) was used for further data processing and statistical analysis. MATLAB was also used for scripting spike train simulation algorithms, as well as for evaluation of the metrics, application of MMO, and cluster based categorization of the data sets. The performance evaluation of the analyzed metrics and the generated new proxy metrics on each of the simulated data sets were based on calculation of correlation coefficient between the independent varying feature of the spike train (ex. rate, regularity, stationarity) and the metric generated values. The significance level for all the statistical tests in this paper were set at $\alpha = 0.05$ (5%). The classification performance and

discriminatory power of the newly generated algorithm were then cross-validated against the subjective classifications using the following parameters and ratings (Demsar, 2006) (Sokolova & Lapalme, 2009):

$$Classification\ Accuracy(CA) = \frac{TP+TN}{TP+TN+FP+FN} \qquad \text{EQ (3.4)}$$

$$Average\ Accuracy(AA) = \frac{\sum_{i=1}^{l} \frac{TP_i+TN_i}{TP_i+TN_i+FP_i+FN_i}}{l} \qquad \text{EQ (3.5)}$$

$$Discriminatory\ Power(DP) = \frac{\sqrt{3}}{\pi}\left(log\frac{Sensitivity}{1-Specificity} + log\frac{Specificity}{1-Sensitivity}\right) \qquad \text{EQ (3.6)}$$

DP <1 poor, ~3 good, fair otherwise

Where, TP is true positive, TN is true negative, FP is false positive and FN is false negative.

$sensitivity = \frac{TP}{TP+FN}$; and $specificity = \frac{TN}{TN+FP}$ EQ (3.7)

l Indicates number of different firing patterns, in this case, regular, irregular and bursty.

3.3. RESULTS

3.3.1. Performance of the classification metrics on simulated data sets

3.3.1.1. Performance on principal spike patterns (stationary and different mean frequencies)

For standard homogeneous simulations, a majority of the metrics, including CV, FF, AF, and the local variables (CV2, LV/LVr and IR) generated largely discriminatory values (Kruskal–Wallis test, $p < 0.005$) for the three basic spike patterns (regular, irregular, and bursty), regardless of mean firing rate (Fig. 3.4a values are normalized to a 0–1 scale); Fig. 3.4a. CV, AI and local ISI variables were able to discriminate between regular and non-regular trains (Tukey–Kramer, all $p < 0.05$). Among the ISI metrics, only LVr fully discriminated between irregular and bursty patterns (Tukey–Kramer, $p = 0.040$). LL and PSP uniformly performed poorly, with LL not showing appreciable discrimination variance (Kruskal–Wallis, $p = 0.356$) and PSP values being largely dependent on the mean firing rate (Kruskal–Wallis, $p = 0.432$). Sk and residual were also universally ineffective ($p > 0.053$). The latter four metrics were rejected from further analysis. As anticipated, BP, BT, and BE distinguished bursty from non-bursty trains (multicompare, $p < 0.05$) with different firing rates, but did not distinguish between regular and irregular trains ($p > 0.056$).

3.3.1.2. Performance on varying properties of firing patterns.

Global variables. Using the methodology described by Hosimoto et al., regular, Poissonian, and bursty patterned spike trains were simulated by generating equally spaced, random, and alternating small and long ISIs, respectively (Fig. 3.5a and c), while maintaining a constant ISI distribution (Fig. 3.5b). In contrast, CV and AI were sensitive to the overall ISI distribution and

thereby could not discriminate between the three patterns (CV: $p = 0.67$).Additionally, CV and AI generated abnormal and inconsistent values in the presence of noise or non-stationarity in the signal.CV, for example, ranged from 0.74 to 1.7 for the same spike train with increasing levels of corruption from 0 to 20%. Although kr discriminated the standard trains ($p < 0.05$), it was too sensitive to extreme outlier values in the ISI distribution. Thus the global metrics were rejected from further consideration.

Local variables. The local variables were all favorably sensitive to the arrangement of the spikes sequences in the train and overall, generated higher values for trains with clustered spikes (fig 3.5a). They reliably discriminated regular from irregular simulated trains with corruption levels of up to 25% of the entire train (Kruskal-Wallis test, $p < 0.05$; classification accuracy of > 85%) and effectively defined the level of simulated irregularity (Appendix, Section 5) (cross-correlation coefficient, r ranges from -0.702 to -0.805, $p < 0.005$) (fig 3.6a and 3.6b). Their effectiveness in discriminating highly diverse irregular from bursty trains was however more limited. As the mean rate or the total burst content of the spike train increases, the instantaneous probability of a spike to occur increases and thus, the variance of a spike train reduces. The reduced instantaneous variance leads to a reduction in the local metric values, thus overlapping with the metric values for near-Poissonian trains (fig 3.4 and 3.7). Similarly, a burst train generates lower values for the ISI metrics if an equally spaced single type BO is superimposed on a regular baseline. Moreover, highly irregular (low $\kappa = 0.25$-0.5 of the gamma distribution), non-bursty trains generate higher metric values and further prevent adequate discrimination between irregular and bursty trains (fig 3.7).

Burst metrics. BP, BT and BE effectively discriminated the burst content of the signal (r = 0.76-0.88, $p < 0.005$) irrespective of the intra-burst variability and any noise in the signal. Since these

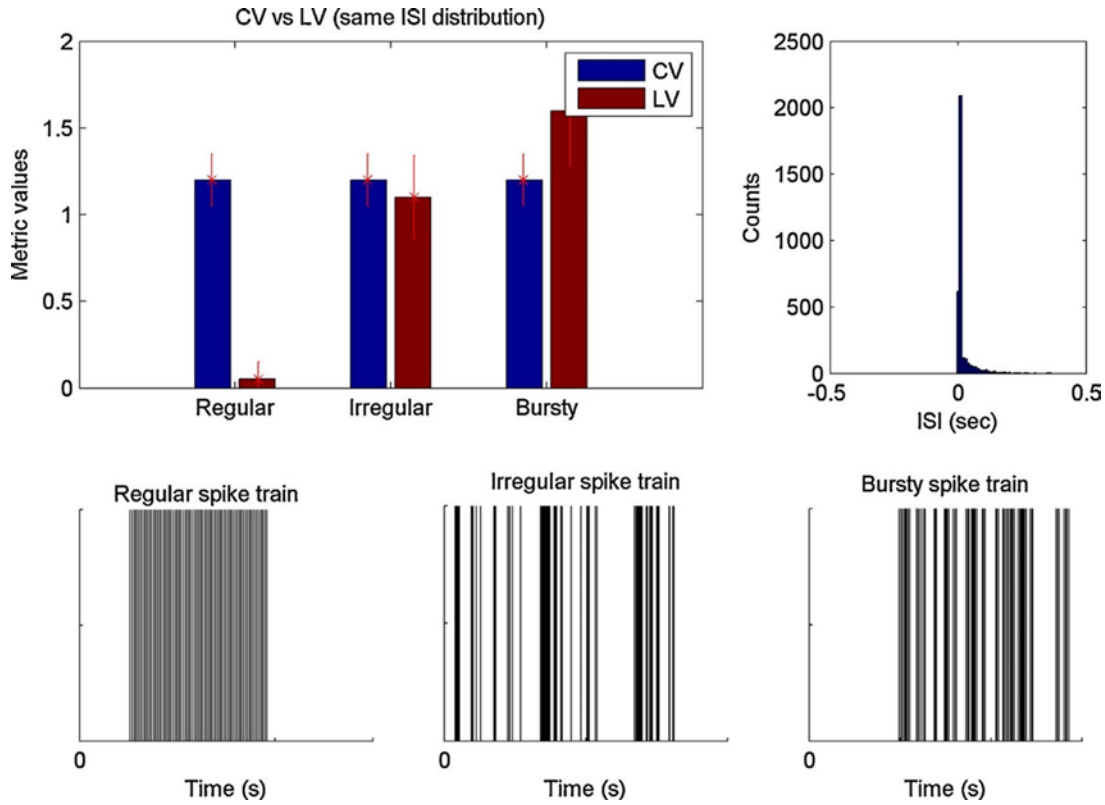

Fig. 3.5. Comparison of coefficient of variance and local variation of ISI's. The figures illustrate (a) discriminatory performance of CV and LV on three representative simulated spike trains (regular, Poissonian, and bursty), with (b) equivalent ISI distributions, but (c) highly dissimilar spike trains. The local variables, including LV, are able to effectively discriminate between the three spike arrangements, while the global variable CV is unable to discriminate between such trains with similar ISI distributions. Error bars indicate standard error.

metrics chiefly measure the frequency of burst events, their values remained relatively constant with increasing BO (fig 3.8a), and declined with increasing numbers of non-burst events (fig 3.8). BP and BT had higher values for pure burst trains, while BE, which reflects both burst and non-burst activity, oppositely, had lower values for pure burst trains. Moreover, increasing the spike rates while maintain the spike/burst arrangement produced reductions in BE, but not BP and BT values (fig 3.8c).

FF and AF. FF and AF were observed to complement each other and together, to effectively delineate non-stationary events in spike train. FF and AF effectively discriminated supra-Poissonian (spike count variance larger than a Poisson process with the same mean) features in spike trains, by generating distinctly high values for spike trains with intermediate corruption events (short duration changes in the spike pattern or rate) (fig 3.9). In contrast to FF, AF was more sensitive to transient alterations in the pattern (κ) than to rate fluctuations. Additionally, in the presence of burst epochs, AF generates lower values, while FF generate higher values (fig 3.4).

3.3.2. Development of tri-component classification metric:

The experiments on the simulated spike trains affirmed that to effectively extract pertinent signalling information from diverse natural spike trains, multiple metrics would need to be integrated in combinations. As each of the local variables were largely effective and complementary in distinguishing regular from irregular spike trains, regardless of noise and non-stationarity, these metrics were combined using MMO to formulate a "regularity metric". After normalizing each of the three metrics, relative statistical weightings were derived using "generalized linear model" (GLM) regression. The final proxy 'regularity metric' is as follows:

$$regularity = 0.125 + 1.119(CV2) + 0.9468(IR) + 0.718(LVr) \qquad \text{EQ (3.8)}$$

BP, BT and BE were observed to be effective and complementary burst detection metrics and upon weighting their relative strengths, the following 'burstiness metric' was derived:

$$burstiness = 0.1234 + 0.501(BP) + 0.510(BT) + 0.496(BE) \qquad \text{EQ (3.9)}$$

Lastly, as FF and AF were affirmed to be effective and complementary indicators of non-stationarity, a "corruption metric" was generated upon weighting these two metrics:

$$corruption = 1.6677 + 1.5371(FF) + 0.9523(AF) \qquad \text{EQ (3.10)}$$

Analyses of regression indicate that each of the predictor metrics has a positive and significant impact on the corresponding discharge features (all $p < 0.05$). Refer to Table 3.2 for statistics for the GLM regressions.

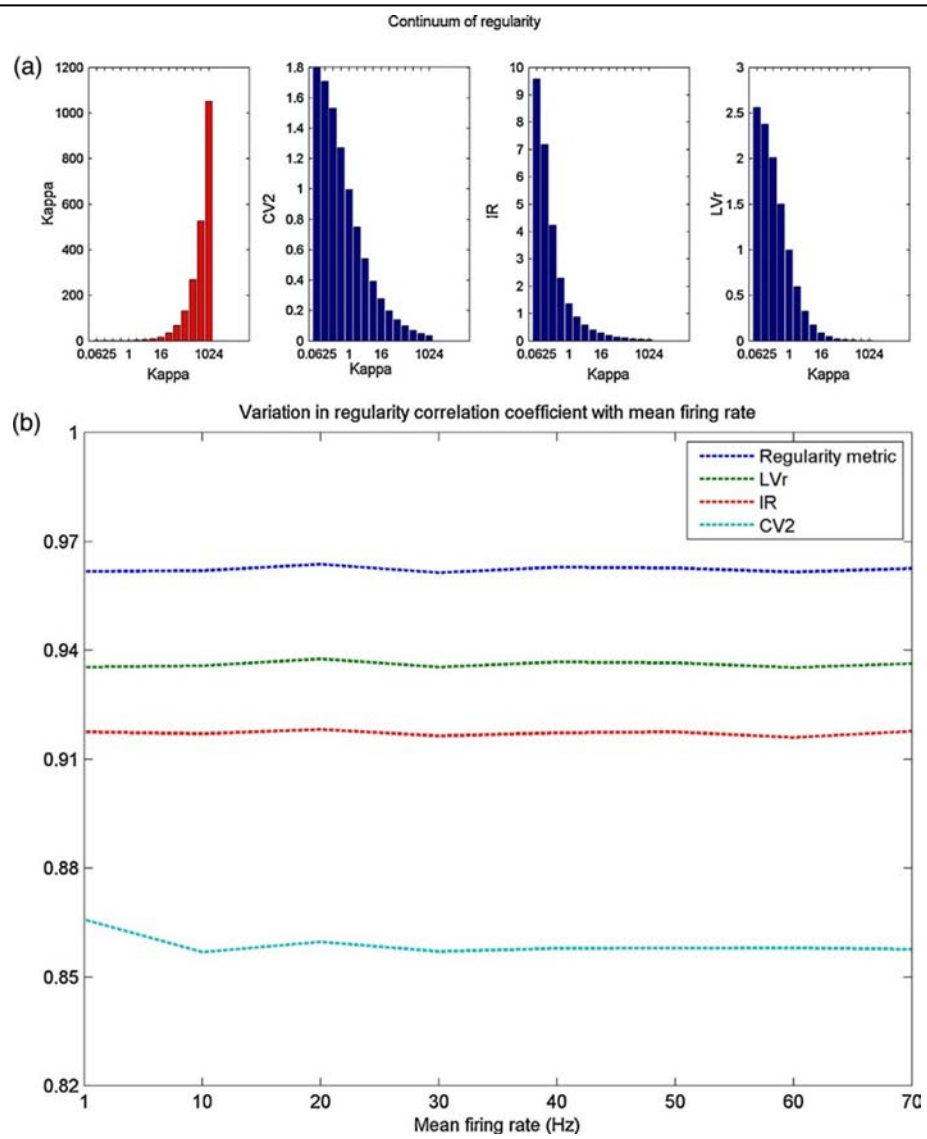

Fig. 3.6. Discriminatory effectiveness of local variables and new regularity metric on a continuum from irregular to regular patterned spike trains. (a) With exponentially increments in _ (shape variable of gamma distribution, red histogram) and rate held at 50 Hz, CV2, IR, and LVr values can be seen to define the extent of irregularity in the simulated spike trains. (b) Although the correlation coefficients of the local ISIs and the new regularity metrics all indicate desirable insensitivity to rate, the new metric can be seen to show superior delineation of the regularity level of spike trains.

3.3.3. Performance of the tri-component classification metric on simulated data

Fig 3.4b demonstrates the outputs of the tri-components on the three principal spike patterns with varying rates. The regularity metric effectively discriminates the three patterns irrespective of the

rate variations ($p = 0.0023$). Similarly, the burstiness metric effectively generates discriminatory values for burst trains ($p = 0.0123$). Fig 3.6b demonstrates the cross-correlations of the local ISI and the new weighted regularity metric with respect to the underlying dependent variable 'κ' of the gamma ISI distribution. The correlation coefficients of these metrics are all effectively insensitive to mean rate (all $p>0.05$). Further, the correlation coefficients of the tri-component regularity metric are greater than the individual ISl local metrics, thereby demonstrating its superiority in delineating the level of regularity of spike trains($r =0.87$, $p = 0.007$). Fig 3.9b demonstrates that the tri-component classification algorithm provides superior overall classification accuracy over individual metrics at different levels of corruption. The new algorithm provides an average accuracy of > 83% even with corruptions of up to 30%. Fig 3.11 compares the classification accuracy of various metrics on a large simulated data pool ($n= 1000$), further demonstrating the superiority of the tri-component classification in discriminating all three principal patterns (av. accuracy = 0.93; CI: 0.91-0.95).

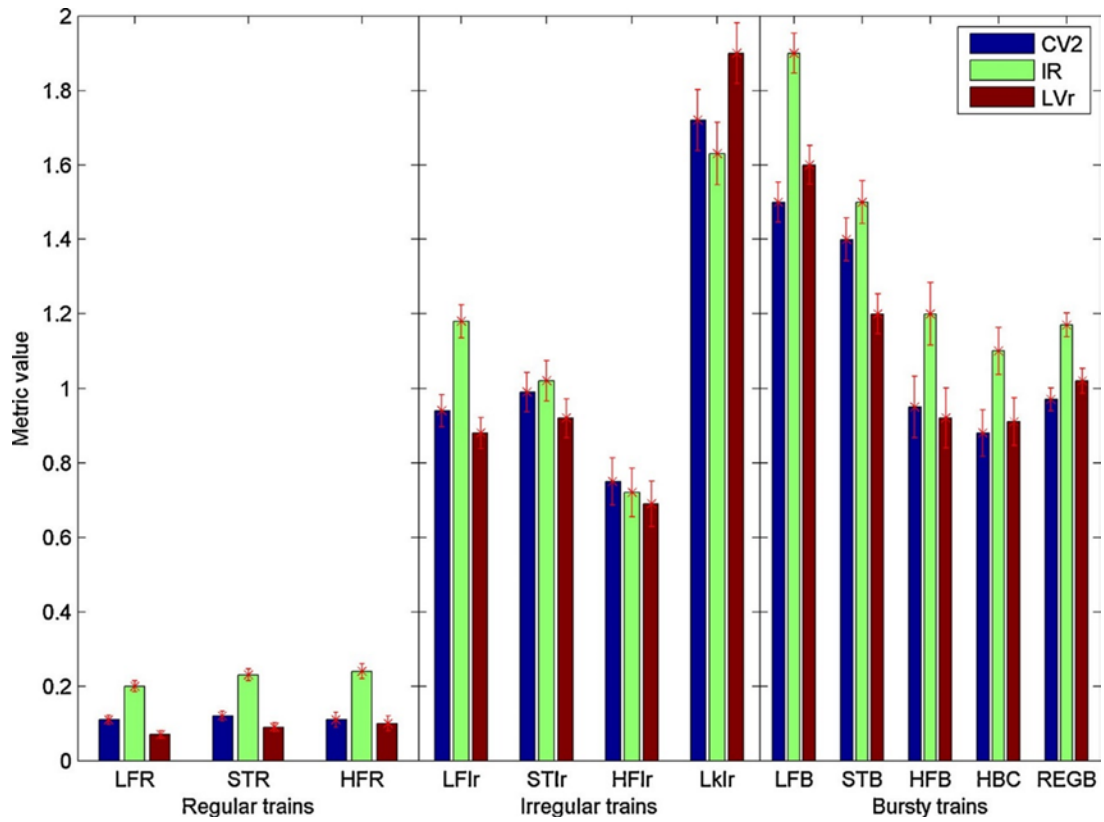

Fig. 3.7. Limitations of local variables in discriminating irregular from burst trains. As illustrated for simulated spike trains, the local variables CV2, IR, and LVr have limited ability to distinguish irregular from bursty trains. LFR = low frequency (1–40 Hz), STR = standard (50–60 Hz), and HFR = high frequency (70–100 Hz) regular spike trains; LFIr = low frequency (1–30 Hz), STIr = standard (50–60 Hz), HFIr = high frequency (70–100 Hz), and LkIr = low kappa (highly) irregular (_: 0.0625–0.5) spike trains; LFB = low frequency (1–30 Hz), STB = standard third order (50–60 Hz), HFB = high frequency (70–100 Hz), HCB = high content (BP > 68%), and REGB = regular baseline (50–60 Hz) burst trains. Error bars indicate standard error.

Table 3.1 : Cross-validation of tri-component classification of neuronal spike data set

	Regular	Irregular	Bursty	Non-stationary	Total
Subjective characterization	57	51	39	0	147
Objective classification	56	49	37	5	147
Tri-component concordant classification (true positives)	54	46	35	0	135
classification accuracy	0.96	0.95	0.96	--	0.96
error rate	0.03	0.05	0.04	--	0.04
precision	0.96	0.94	0.95	--	0.92
discriminatory power (DP)^	2.90	2.45*	2.67*	--	2.60

***** These relatively lower values to a large extent reflect that several of these trains were only correctly classified as highly non-stationary and rendered uncategorizable by the tri-component classifier.

^ DP <1 poor, ~3 good, fair otherwise

Table 3.2. Statistics for the estimated coefficients of the GLM regression

Proxy metrics	Constituent predictor metrics	Coefficient estimates	Standard error	P value	95% Confidence Interval	
Regularity Dfe = 164	CV2	1.119	0.134	0.0087	0.851	1.387
	IR	0.946	0.021	0.0299	0.904	0.988
	LVr	0.781	0.035	0.0012	0.689	0.873
	Constant	0.125	0.010	0.0098	0.104	0.146
Burstiness Dfe = 136	BP	0.501	0.036	0.0079	0.429	0.573
	BT	0.510	0.087	0.0331	0.337	0.683
	BE	0.496	0.124	0.0291	0.247	0.744
	Constant	0.123	0.023	0.0021	0.077	0.169
Corruption Dfe = 87	FF	1.531	0.028	0.0000	1.474	1.587
	AF	0.952	0.148	0.0063	0.656	1.247
	Constant	1.667	0.062	0.0422	1.543	1.791

* Dfe = degree of freedom.

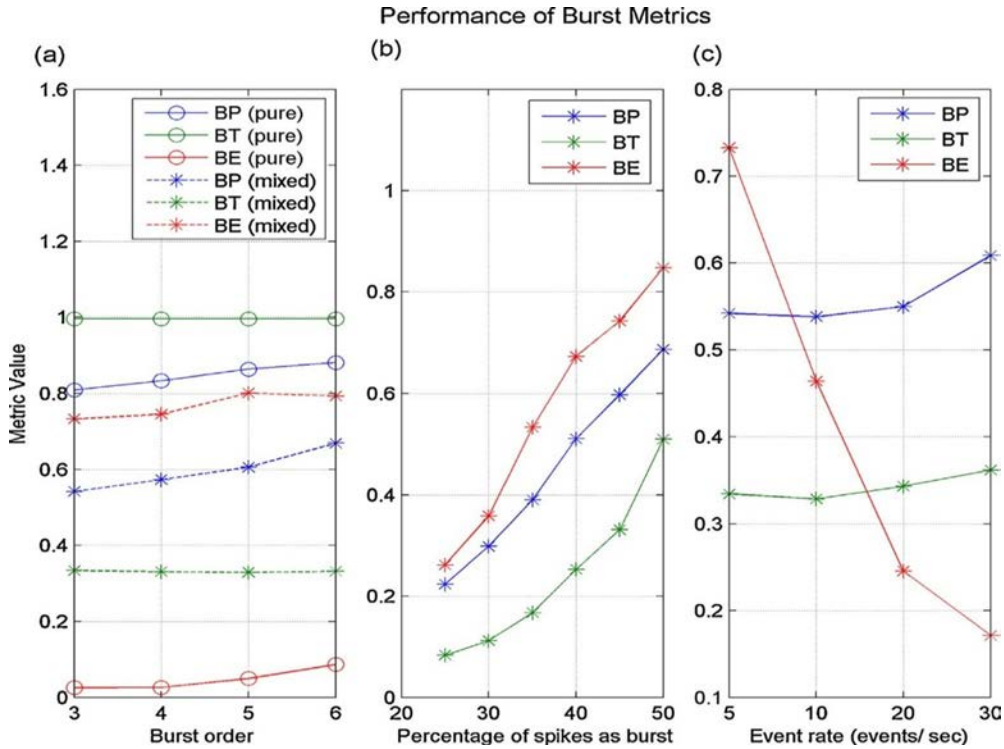

Fig. 3.8. Performance of novel burst metrics (burst percentage, burst tendency, and burst entropy). (a) The left figure illustrates that BP and BT generate higher values for pure burst order (BO) simulated spike trains, while BE generates higher values for mixed BO trains. All three metrics can be seen to be largely independent of the BO. Note: BO of a pure burst train indicates the number of spikes in the burst, while a mixed third BO train, for example, has single spikes, doublets, and triple spike events. (b)The middle figure illustrates that all three metrics increase appreciably with increasing percentage of the total spikes in bursts (burst spikes/total spikes). (c) The left figure illustrates that BP and BT values increase to a modest extent, while BE values reduce appreciably with simulated increasing event rates ('events' refer to individual spikes, doublets or bursts).

3.3.4. Assessment of the tri-component classification metric on real neuronal spike data

The table 3.1 shows the cross-validation results comparing the classification of the tri-component metric to that of the subjective classifications of the neuronal recordings. The tri-component algorithm showed 95.9% (CI: 0.91-0.98) overall concordance with the subjective classifications with a high discriminatory power of 2.6 (defined in Section 2.7). Five recorded spike trains were highly non-stationary and rendered uncategorizable by the MMO classifier, thereby lowering the

apparent accuracy of the cross validations. Fig 3.10 illustrates the K-mean clustering results from the recorded spike data. The receiver operating characteristic (ROC) curve (Swet, 1996) parameterized by true and false positive rates illustrated in fig 3.11b demonstrates the appreciably better performance of the tri-component classifier compared to individual popular metrics.

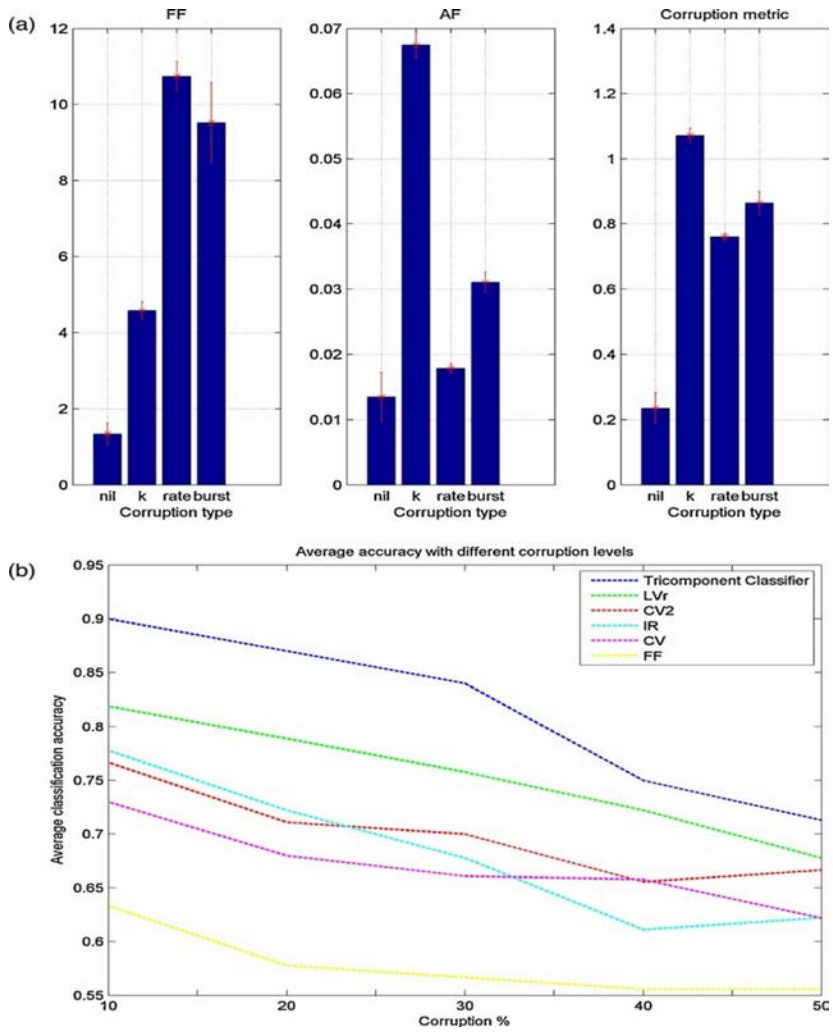

Fig. 3.9. Performance of discriminatory metrics under non-stationary conditions. (a) FF, AF and combined novel corruption metric performance on different types of corrupt spike trains. The figures show means and SEs for 'nil', representing a range of principal simulated spike patterns (regular, irregular and burst) of non-corrupted trains; kappa (k), representing a range from 10 to 40% pattern corruption in a Poissonian train; rate, representing ranges of 10–40% rate corruption in a Poissonian train; and burst, representing ranges of 10–40% burst corruption in a Poissonian train. The combined figures illustrate that FF and AF each are good at distinguishing particular aspects of corruption, while the novel corruption metric, which combines both FF and AF, is able to take advantage of the different merits of each metric. Error bars indicate standard error. (b) The tri-component classifier is demonstrated to provide better overall classification accuracy than other metrics.

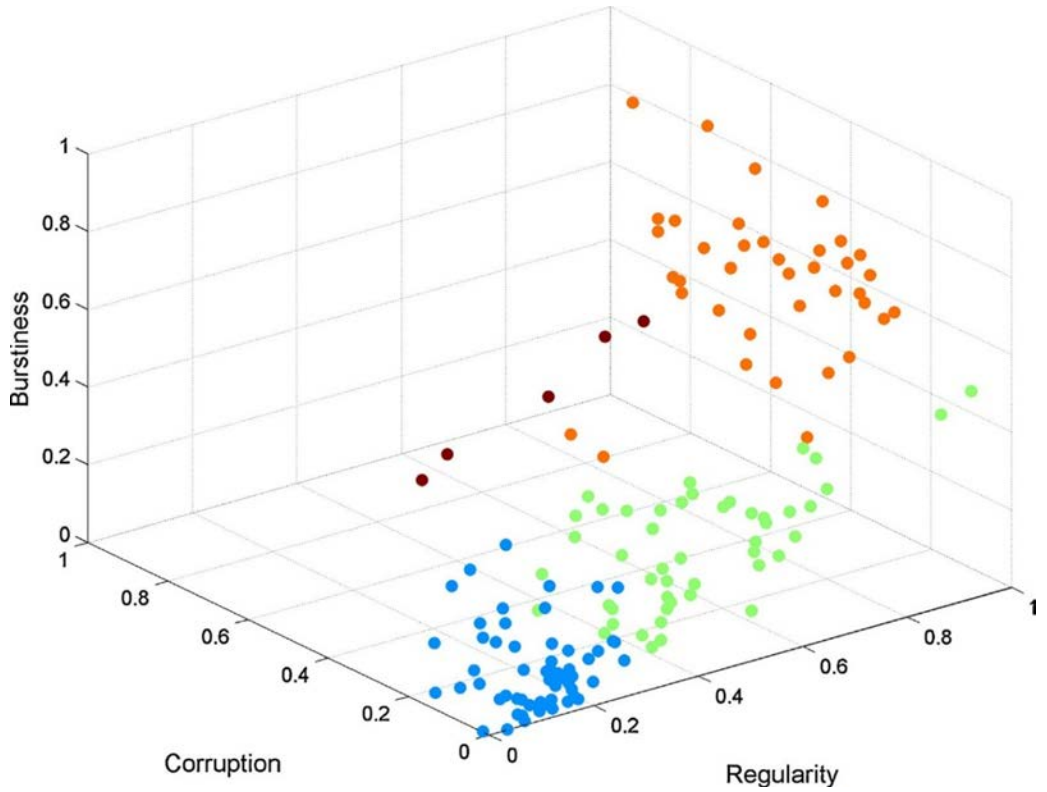

Fig. 3.10. 3 D scatter plot classification of representative neuronal recordings. The figure illustrates K-mean clustering distributions of multi-site extracellular neuronal recor-dings (n = 147) from normal and dystonic rats with the novel proxy classification metrics ('regularity', 'burstiness', and 'corruption') plotted on each axis. Blue dots = regular, green = irregular, orange = bursty, and brown = non-stationary trains.

3.4. DISCUSSION

The purpose of this chapter was to develop an algorithm which can reliably define the basic underlying discharge patterns of neuronal spike trains recorded in real time irrespective of local variations in the signal. Results showed that the tri-component algorithm introduced here is able to effectively discriminate among the highly diverse spike arrangements encountered throughout the brain, even in the presence of natural and artificial corruptions in the recorded spike trains. The reliability of the algorithm was affirmed by cross-validation on 147 neuronal spike trains

recorded in vivo from diverse regions of the brain in both the normal and a representative diseased state. The algorithm offers a much needed robust, rapid, and automated means to categorize neurons into the three basic encountered discharge patterns: regular, irregular and bursting. The algorithm, in turn, obviates the need for time consuming, subjective estimation of neuronal discharge patterns.

From systematic testing of available classification metrics on simulated spike data, it can be affirmed that individual metrics were limited in their ability to discriminate the multiple features of the spike trains. Many of the popular metrics were unacceptably sensitive to such features as the rate or spike arrangements, such that they generated different values for similar pattern configurations. Such metrics were rejected from further consideration. Additionally, different simulated spike configurations were often observed to alter various metrics in equivalent ways, thereby limiting the robustness of individual metrics. For instance, FF was found to effectively delineate transient changes in the baseline rate and unusual burst events (Lerchner, et al., 2004) . In contrast, AF, which has low sensitivity to slower variations (Gebber, 2006) was found to be more sensitive to transient changes in the regularity pattern. Such examples lead to recognize the need to develop an algorithm incorporating multiple metrics dedicated to detecting each of the three identified patterned features of the spike train: *regularity*, *burstiness*, and *corruption*.

After identifying desirable metrics from their performance on the simulation spike trains, multiple metric optimization on the spike simulations to weight the relative strengths of the metrics towards developing the novel tri-part classification algorithm was used. Subsequently, a large data set of highly diverse normal and pathological neuronal recordings from diverse

regions of the brain in normal and dystonic rats were extensively inspected and subjectively classified. These classifications were used as the gold standard to validate the proposed algorithm. Ultimately, the three proxy metrics developed here were affirmed to effectively isolate the desired features in the feature space and to very closely approximate the results of this

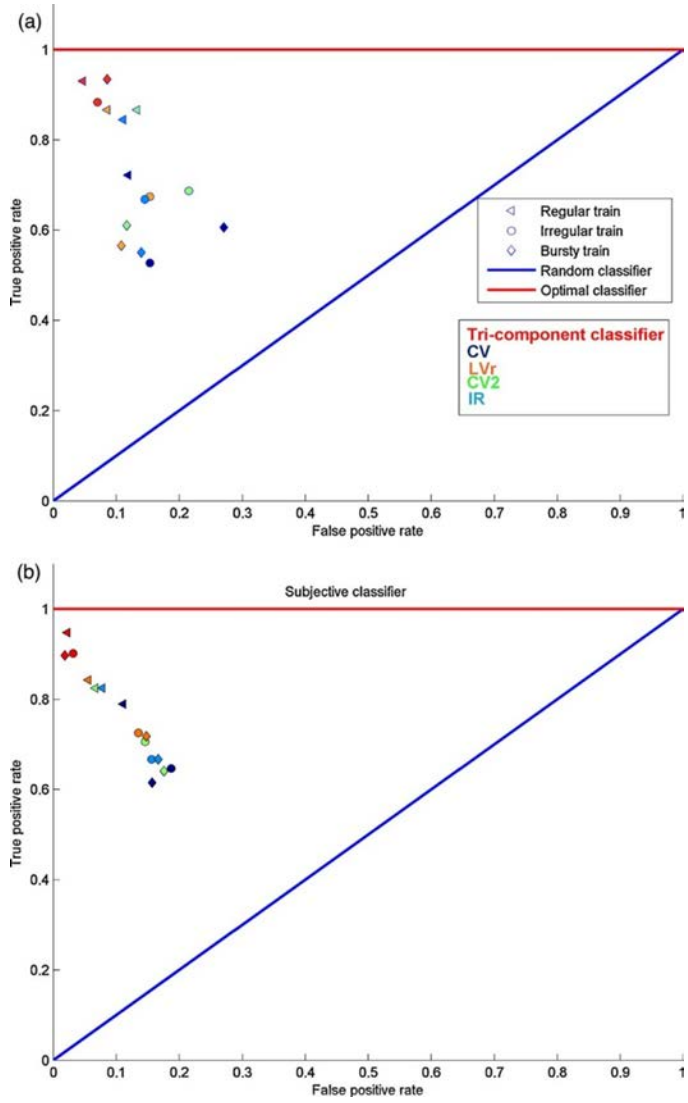

Fig. 3.11. Receiver operating characteristic (ROC) curve comparing performances of classification metrics. (a) The tri-component classifier is demonstrated on a large simulated data pool to provide superior discrimination of all three principal patterns over individual metrics (CV and the local metrics). True and false positive rates indicate the performance verses that of an 'optimal' classifier derived from user controlled simulations. (b) The tri-component classifier is demonstrated here to well outperform the individual metrics in classifying diverse representative neuronal spike trains. The performance of the objective metrics is cross-validated with respect to subjective "gold standard" classifications.

meticulous subjective analyses.

The ‘regularity’ metric (equation 3) detects the local variability between adjoining spikes in the train and as such, is able to discriminate any sub-Poissonian tonic arrangement in the spike train. Although, the contributing local ISI metrics generate higher values (>1) for typical burst patterns, their tendency to also generate misleading high values for particular non-regular trains (e.g., irregular and high frequency burst trains and non-homogeneous bursty trains) limits its use for discriminating bursty from irregular spike trains. The ‘bursty’ metric (equation 4) incorporates several burst metrics which assess the burst content of spike trains and together were shown to provide a reliable metric for discriminating bursty trains from non-bursty trains. Although such properties as BO (average number of spikes in a burst), intraburst spike pattern (Brochini, et al., 2011), bursts per minute, and average burst duration are defining burst properties of neurons, they do not specifically address the burstiness of neurons and so were not incorporated into the burstiness metric. All popularized metrics initially tested here, including ACH based parameters, CV, local ISI metrics, and FF and AF, assess burstiness based on defining cluster tendencies in the spike train, but all ultimately proved to be unreliable. For instance, in the clustered spike simulations, none of these metrics could reliably distinguish ISIs below the absolute refractory limits or greater than an acceptable intra-burst interval range. Ultimately, these techniques proved to be too restricted to be used to detect the multiple features which define burstiness. The third (‘corruption’) metric (equation 5) measures the spike count variability across the spike train, such that non-stationary trains generate higher discriminable values than stationary trains.

The tri-component 3D feature space defines the pertinent features of spike trains from multiple perspectives. Further, the semi-supervised K-mean clustering incorporates two particular advantages to the algorithm. First, the user has control over defining the centroids for each pattern defining category, while the ultimate designation of each train is automated. Second the technique is adaptable to any shift in population response and introduction of noise. Moreover, the final centroids of the clusters reveal useful insight into the instability and variability of the studied neuronal populations.

The estimated classification accuracies of at least 94% for each of the three proxy metrics on highly diverse representative neuronal recordings support the reliability of the developed algorithm. This assertion though largely relies on the contention that the intensive, subjective characterization of the recorded spike data used as the gold standard here was itself highly accurate. Although the subjective assessments were meticulously performed by experienced and skilled investigators, it can be acknowledged as a limitation to validating the discrimination algorithm. Nevertheless, the fact that the two independent means of classifying these data produced very similar results is most supportive of each other. Furthermore, in at least some instances, the algorithm was likely to be more reliable than the subjective categorizations. For instance, while five spike trains were subjectively characterized as irregular or slightly bursty, these appeared, upon re-inspection, to be correctly designated by the tri-component classifier as non-stationary/ uncategorizable. It can be further suggested that the purported slightly lower discriminatory power of the algorithm for irregular versus bursty trains may in fact be accounted for by false negatives due to apparent limitations in the ability to fully subjectively discriminate

non-stationary spike trains. Moreover, the non-stationarity in the recorded signals chiefly reflected the natural changing environment of the biological system.

As discussed, the classification algorithm was ultimately validated on representative neuronal recordings from multiple brain regions in both the normal and a pathological state. The neuronal sample included recordings in dystonic animals, a condition associated with highly irregular discharge patterns and prominent bursting (Baron, et al., 2011). Nevertheless, considering the vast variability in biological systems and the focus here on rodents, it cannot be exclude that additional naturally occurring spike train features were omitted which could have altered the final algorithm. Therefore the proxy metrics should be carefully assessed by others and modified, if necessary, to best capture any newly encountered biological features. Additional considerations will be to specifically modify the algorithm to account for phasic alterations in the spike train associated with, for example, movement.

The presented algorithm could provide a much needed automated and universally accepted neuronal pattern discriminatory method. As such, the algorithm could importantly advance comparisons of data between laboratories studying similar and different pathological conditions or investigating different species and animal models; for example comparing data from rodents with data collected from more restrictive investigations in humans. Also, the application of the present algorithm and its component metrics can be extended to provide more detailed insight into numerous aspects of complex signaling. For instance, because the regularity metric and its components linearly follow the level of irregularity (as was shown in fig 3.6), these metrics can be used to determine whether a particular nucleus contains a single versus two or more distinct

neuronal populations or alternatively, a continuous spectrum of discharge types. Additionally, identified bursty neuronal populations can be further sub-categorized based on the mean BO of the neuron, burst rate, inter-burst, and intra-burst properties. Further, the regularity metric and corruption metric can be used to define localized variations in signaling and thereby help to characterize changes in signaling related to salient biological features.

CHAPTER 4

PRESERVED DICHOTOMY BUT HIGHLY IRREGULAR AND BURST DISCHARGE IN THE BASAL GANGLIA IN ALERT DYSTONIC RATS AT REST

4.1. INTRODUCTION

Dystonia is a devastating condition characterized by ineffective, twisting movements, prolonged co-contractions, and contorted postures (Kernich, 2003). Despite its prevalence, the etiology for two-thirds of dystonia cases is not known and the underlying pathophysiology remains poorly understood. Although some investigators suggest a role for the cerebellum, most evidence from strokes (Münchau et al., 2000), from microelectrode recording studies in humans undergoing globus pallidus internus (GPi) ablation or deep brain stimulation (DBS) surgery (Vitek et al., 1999) (Lenz et al., 1999) (Zhuang, Li and Hallett, 2004) (Starr et al., 2005), and in animal models of dystonia (Chiken, Shashidharan and Nambu, 2008) (Nambu et al., 2011) (Baron et al., 2011) (Richter and Loscher, 1993) (Loscher et al., 1989) suggest a principal role of the basal ganglia in most forms of dystonia. Compared to normal monkeys, neuronal discharge activity in the GP externus (GPe), subthalamic nucleus (STN) and GPi in humans with dystonia shows reduced rates and prominent discharge irregularity (Lozano et al., 1997) (Zhuang, Li and Hallett, 2004) (Vitek et al., 1999). In one study (Zhuang, Li and Hallett, 2004), approximately 80% of neurons in GPe and STN were found to show irregular and grouped discharge activity with intermittent pauses and low frequency burst activity. Comparable abnormal alterations have also been reported in GPi in humans with dystonia relative to the

discharge characteristics in normal monkeys (Hashimoto, 2000) (Lenz et al., 1999) (Lozano 1997) (Zhuang, Li and Hallett, 2004). Although specific alterations in basal ganglia neuronal discharge activity are likely to account for most of the characteristic motor features of dystonia, to date, the abnormally patterned discharge activity has not yet been systematically investigated in animal models of dystonia.

The present study was designed to define and compare single cell activity in GP (rodent equivalent of GPe), STN, and the entopeduncular nucleus (EP, rodent equivalent of GPi) in alert, head restrained jaundiced dystonic Gunn rats (Chaniary et al., 2009) and healthy control rats at rest. Although normal and abnormally patterned basal ganglia discharge activity have been described previously in many rodent studies, these reports were regularly compromised by a number of technical limitations, including the frequent use of anesthesia, infrequent control for the influence of movement in alert animals, and inadequate methodology to effectively differentiate different types of neurons. A novel multiple metric optimization neuronal classifier based on a representative large set of simulated spike trains was developed previously. Subsequently, a subset of the data from the present study, along with diverse representative neuronal recordings from the cerebral cortex, hippocampus and thalamus, were used to validate the algorithm (Kumbhare and Baron, 2015). The new algorithm as described in chapter 3, in turn, was used here to classify an extensive normal and dystonic neuronal pool in GP, STN and EP as regular, irregular, or burst predominant.

While DBS surgery is highly beneficial for treating primary dystonias, the surgery is largely ineffective for most secondary forms of dystonia, including kernicterus and thus, alternative

mechanistic based strategies for reversing the underlying pathophysiology are critically needed. Presently, It's been postulated that definable changes in neuronal rates and, in particular, in patterned discharge activity, in GP, STN and EP would correlate with the severity of dystonia.

4.2. EXPERIMENTAL PROCEDURES

4.2.1. Animals and induction of dystonia.

A total of 34 juvenile non-carriers and non-jaundiced heterozygous (Jj) *Wister* rats, affirmed as clinically normal, were used for control studies. A total of 65 juvenile homozygous (jj) *Wister* Gunn rats were used to generate the dystonia model (Byers, Paine and and Crothers, 1955) (Perlstein, 1960) (Günay, Edgerton and Jaeger, 2008) (Volpe, 2008). The induction, clinical, and EMG features of the dystonia model have been described previously (Chaniary et al., 2008) (Chaniary et al., 2009) (Shaia & Shapiro, 2002). The jaundiced Gunn rat is a well-established clinical and pathological model which closely resembles human kernicterus (Byers, Paine and Crothers, 1955) (Perlstein, 1960) (Volpe, 2008). Gunn rats are genetically deficient of UDP glucuronosyl transferase, the principal liver enzyme responsible for bilirubin clearance. Homozygous recessive (jj) pups appear normal apart from being jaundiced in the first weeks of life. Free unbound bilirubin blood levels are highest at 16–17 days of age when levels of blood albumin, which binds bilirubin and normally keeps it out of brain, are relatively low (Schutta and Johnson, 1969). At 16 days of age, the animals received an intraperitoneal injection of sulfonamide (100 mg/kg) to displace bilirubin from albumin, allowing appreciable quantities of bilirubin to cross the blood-brain barrier (Diamond and Schmid, 1966) (Diamond and Schmid, 1968). The rats became prominently dystonic within minutes to hours after injection. Of these animals, 25 developed very mild to moderate generalized dystonia and comprised the

experimental group. Of the remaining animals, 14 were severely affected and did not survive the acute bilirubin encephalopathy, 10 with a clinical score (CS) $\geq$ 3.5 (described below) were deemed too weak to survive the surgery, 9 were unaffected and not further studied, and 7 spontaneously recovered from the dystonia and were not included in this study. The experimental group was compared with homozygous jj controls given saline and heterozygous Nj controls given either sulfonamide or saline. All experiments were approved and monitored by the Hunter Holmes McGuire Veterans Affairs Institutional Animal Care and Use Committee (IACUC) and performed in accordance with regulatory guidelines.

4.2.2. Scoring of dystonia and EMG recordings

The behavior of the animals was subjectively assessed daily and a CS between 0 and 5 was assigned on the day of surgery based on the severity of the movement disorder (0 – normal, 1 – slight limb dystonia and gait abnormality, 2 – mild limb dystonia and gait abnormality and a prolonged righting reflex, 3 – moderate limb dystonia and gait abnormality and an impaired righting reflex, 4 – severe dystonia with failure of ambulation and no righting reflex, and 5 – moribund, including seizures and agonal respiration (Chaniary et al., 2008) (Chaniary et al., 2009). For scores midway between categories, 0.5 was added. The animals were also video recorded while ambulating in a Plexiglass box with gridlines and hindlimb paw spread was later determined as an objective measure of the severity of the dystonia (Chaniary et al., 2009). Additionally, EMGs were recorded from surgically implanted thin Teflon coated (50 μm bare, 110 μm coated) stainless steel wires (A-M systems, Carlsborg, WA, USA) in hip and stifle (‘knee’) antagonist muscle pairs and monitored on and off-line for evidence of movement of the

animal and for objective confirmation of dystonia and its severity. Due to frequent technical issues with maintaining the wires, EMGs were variably recorded from 0-4 muscles.

4.2.3. Surgery

Surgeries were carried out under 1.5-4% general isoflurane anesthesia (with 1 L/min O_2) on day 30-47. Throughout the surgery, the body temperature was maintained at 35 ± 1 ^{o}C with a regulatory heating pad and respiratory rate was constantly checked using an audio monitor. Ophthalmic ointment was applied to protect the eyes. The head and hip area were shaved and disinfected using Betadine scrub solution. After the animal was draped, an incision was made along the sagittal plane of the head using sterile techniques. The exposed area of the skull was thoroughly cleaned and dried to assure no soft tissue or fluid covered the site of implantation. A custom stainless steel head fixture was firmly secured to the animal's skull using miniature screws positioned just below the ridges of the parietal bone of the skull. The fixture was further secured using epoxy to seal the bone-fixture interface. Relevant hindlimb muscles were surgically exposed and Teflon coated 50 μm stainless steel fine wire electrodes (A-M systems, Carlsborg, WA) were inserted via a 30 gauge needle and sutured into antagonistic hip muscles, the gluteus superficialis (hip flexion) and the gluteus medius (hip extension) (Chaniary et al., 2008). To assure correct placement of the wires, the wires were stimulated electrically (Grass Technologies, West Warwick, RI, USA) and the expected hindlimb responses verified. The EMG wires were tunneled together subcutaneously and passed through the opening over the skull and then soldered to a micro-circuit board. The board in turn was secured to a removable Teflon cap, which covered the head holder in-between experiments and was secured to the stereotaxic apparatus during the recording sessions. The incision was sutured and cleaned with

3% hydrogen peroxide solution. Local anesthetic, bupivacaine (0.1-0.55 ml) was injected into the incision. The analgesic, buprenorphine (0.25-1.6 mg/kg, i.p.) was administered prior to discontinuing the isoflurane. After the surgery and subsequent recording sessions, the head fixture chamber was filled with saline and sealed using a plastic cap holder. After the initial surgery, the animal was returned to its cage and allowed 24 h for recovery. No overt signs of stress, pain or change in behavior were evident after implantation of the head fixture.

Generally, the following day, the rat's head was immobilized by clamping the head fixture into a custom stereotaxic positioner (Chaniary, et al., 2011). A dial test indicator (Chaniary, et al., 2011) was used for precise positioning and alignment of the skull. Under isoflurane anesthesia, a 3.5 mm burr hole, centered at 2 mm caudal and 1.5 mm lateral to the bregma reference point, was drilled into the skull exposing the underlying dura mater, targeting the hemisphere contralateral to the study hindlimb. Buprenorphine (0.25-1.6mg/kg, i.p.) was administered prior to discontinuing the isoflurane. In most rats, after 30-50 min., allowing for full behavioral recovery from effects of anesthesia, neuronal recording sessions were initiated with additional substantial time transpiring during initial target delineation prior to data collection. The animals all appeared fully alert during the subsequent neuronal recordings, requiring brief interruptions of data collection during periods of motor activity. However, to control for potential residual drug effects and a lack of acclimation to the head restraint, the recording sessions were delayed for ~48 hrs after placement of the burr holes in two non-carrier rats, during which time the rats underwent 2-3 hrs/ day of acclimation to head restraint. All rats were regularly monitored for apparent signs of pain, discomfort or altered sensorium following the surgery and during and after the recording sessions.

4.2.4. Neurophysiological Recordings

A mini-xyz microelectrode manipulator (Thomas RECORDING GmbH, Giese, Germany) was mounted onto a KOPF stereotactic arm. The posterior-lateral motor territories of GP, STN and EP based on findings in primates (Baron et al., 2002) were specifically targeted from online assessment of relations between neuronal discharge and active and passive limb movements and offline correlations between neuronal discharge and EMG activity. GP was chiefly targeted with a 10-15° medial-to-lateral approach in the coronal plane, while the STN and EP were mostly targeted with a 10-15° anterior-to-posterior approach in the sagittal plane (fig 4.1a). Extracellular neuronal activity was recorded using high impedance (1-2 MΩ), 100 μm Thomas RECORDING quartz-platinum microelectrodes. The location and firing patterns of cells and the borders of encountered nuclei along each microelectrode track were plotted (fig 4.1b) and transparencies generated from sections of the Paxinos and Watson atlas (Paxinos and Watson, 1982) were superimposed upon these plots. Each nucleus was identified by the electrode depth position (fig 4.1a-c) and characteristic neuronal firing patterns. For instance, although STN and EP showed similar discharge patterns, STN generally shows greater background activity and appreciably greater probability of encountering more than one neuron on a single microelectrode due to its comparatively higher neuronal density. Additional landmarks, including the optic track, internal capsule and length of cortex, thalamus, striatum and hippocampus, were used to precisely locate the targeted nuclei and specifically, their posterior-lateral regions. To reduce potential effects from damage due electrode passage, the number of penetrations was generally limited to 4-5 tracks per rat.

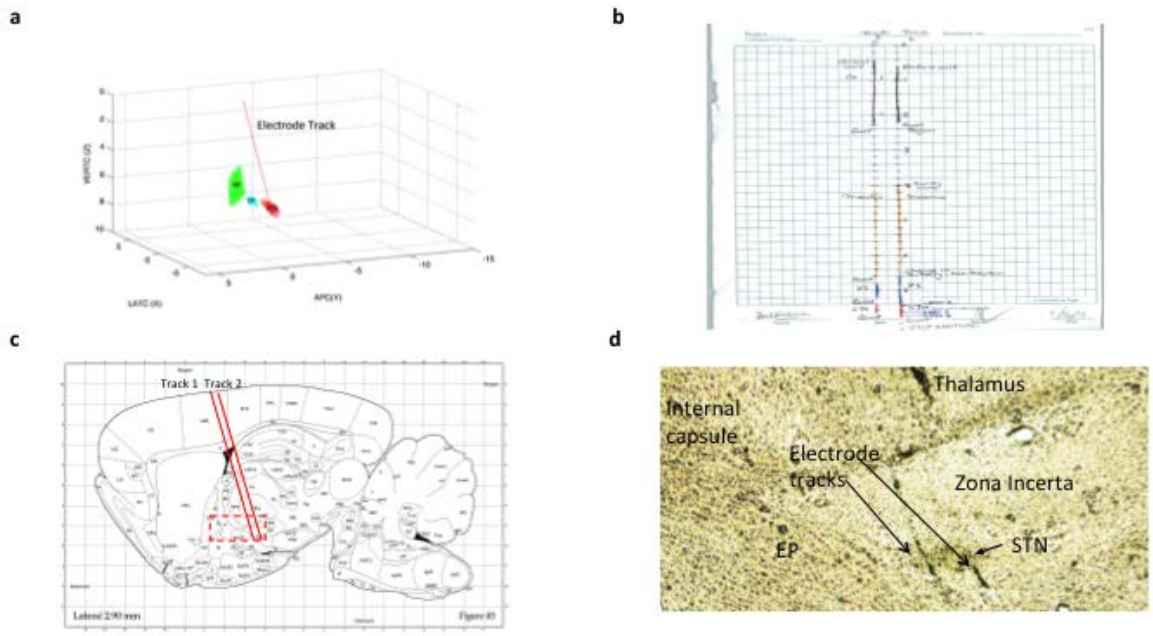

Fig. 4.1. Planning and plotting of recording tracks and histological reconstruction. (a) Illustrated is an example of STN targeting from one of the study experiments using custom programmed 3-D representations. The targeted electrode track (red line) depicts an appropriate planned trajectory for the initial microelectrode (using brain surface coordinates for microelectrode entrance, lateral = 2.9, posterior = 1.6, sagittal angle = 15^0. **(b)** Shown is the laboratory notebook plots of the two actual recording tracks, including designation of encountered nuclei. Each encountered neuron and its location are separately detailed in the notebook (not shown). **(c)** The tracks were subsequently superimposed on the Paxinos and Watson atlas (Paxinos and Watson, 1982) very close to their initial planned trajectories within the targeted motor territory of STN (at lateral 2.9 mm). **(d)** The histological silver stained sagittal reconstructions affirmed the illustrated microelectrode tracks to be accurately plotted during the recording sessions.

The recorded neuronal activity was displayed over an oscilloscope screen (Hameg Instruments, Mainhausen, Germany) and connected to an audio amplifier for aural monitoring of the signal. Neuronal spike activity was collected for a minimum of 120 sec at a sampling rate of 40 kHz and amplified and band pass filtered (gain = 50, bandwidth 0.07-8 kHz) using Sort Client 3.2.4 (Plexon Inc., Dallas, TX). Quality of neuronal isolation was continuously monitored online using Sort Client. The animals and EMGs were continuously monitored to assure that the animals were fully alert but not moving during data collection. Data collection was interrupted in the event of detected movement or changing background activity, most frequently indicating undetected

chewing movements. Any recorded movement epics were separated and not considered for the present further analyses.

The animal was intermittently hydrated and fed during the recording sessions. A laboratory veterinarian technician constantly monitored the rat during the entire experiment for apparent movement, agitation or change in level of alertness. The animals for the most part rested comfortably with occasional grooming movements, without signs of agitation or sleepiness throughout the 2-3 hour recording sessions. Infrequently, when a rat displayed excessive movement, recording sessions were terminated early and the rat was released and returned to cage. Only infrequently, recordings were carried out on a second day. In such cases, typically the rat was briefly anaesthetized and the dura mater was superficially scraped. Subsequently, Buprenorphine (0.25 mg/kg, i.p.) was administered prior to discontinuing the anesthesia. After the recording session, the animals consistently exhibited normal behavior (grooming, exploring naturally and eating) immediately after they were released into the gait assessment apparatus or cage, indicating showing no signs of overt distress, excessive sleepiness, or gait disturbances (in normal animals).

4.2.5. Histology

At the completion of the experiments, the rats were euthanized with pentobarbital (0.1 ml, 390 mg/ml i.p.) and immediately perfused via the ascending aorta with 200 ml of saline followed by 200 ml of 10% formalin. After fixation, the brains were frozen, blocked in the parasagittal plane, sliced in 50 μm sections on a cryostat, and alternate sections were silver stained (FD NeuroSilver™ kit II, FD Neurotechnologies, Ins.). Silver staining (fig 4.1d) permitted excellent

post-mortem visualization of the microelectrode tracks. The location of recorded neurons were then affirmed by identifying the location of the microelectrode tracks with the use of the Paxinos and Watson atlas and comparing these findings to that determined during the physiological recording experiments.

4.2.6. Spike Detection and Offline Sorting

The discharge spikes were extracted online via manual amplitude thresholding of continuous signals during the recordings and saved for offline spike sorting (fig 2.7) in MATLAB R2012a and Offline Sorter V 3.2.4, Plexon Inc. For more details please refer to section 2.2.2(a)
EMG signals were pre-processed and decomposed as described previously (Chaniary et al., 2008). Since the focus of the present manuscript was on analyzing neuronal activity during rest, the EMGs were used here (off- and online) chiefly to discard any movement epics from the analysis.

4.2.7. Pattern Discrimination and Classification

The spike rasters generated from the spike sorting were initially pre-analyzed by inspection of their mean waveforms and ISI histograms (fig 4.4 middle and bottom row). Spike trains were rejected if more than 5% of the ISIs were less than the absolute refractory period (2 ms) or the variance in the waveform shape were abnormally high. Subsequently, all adequate spike raster were subjected to the novel pattern discrimination algorithm. The formulation of the spike pattern discrimination algorithm and support for its accuracy were detailed in a previous manuscript (Kumbhare and Baron, 2015). Briefly, in order to characterize neurons into the three basic discharge patterns (regular, irregular and bursty), it is necessary to define three main features in the spike trains: Poissonian irregularity, burstiness and non-stationarity. The first two

features classify the spike trains and the third feature describes the level of noise and non-stationarity in the signal. The discrimination algorithm was developed utilizing multiple metric optimizations (MMO), which combines the weighted values of various discriminating metrics into new metrics that act as proxy metrics for each of the above three features. Local ISI variables (CV2, the coefficient of variation for a sequence of two ISIs; IR, the difference of the log of two adjacent ISIs, and LVr, local variables with refractory period information) are combined to form a new "irregularity metric" which distinguishes regular from non-regular trains. Novel burst percentage (BP), burst tendency (BT) and burst entropy (BE) metrics define the burst content in the spike train and are combined to generate "burstiness metric". Lastly, as Fano factor (FF) and Alan factor (AF) were affirmed to be effective and complementary indicators of non-stationarity, a "corruption metric" was generated upon weighting these two metrics. The assigned statistical weights of each of these metrics were determined from generalized linear model (GLM) regression using normal distributions on a large training data set. The final three proxy metrics are described in EQ (3.8)*, (3.9) and (3.10)
**redesignated 'irregularity' rather than 'regularity' for clarity.*

After calculating the tri-component values for each spike train, these data were plotted in a 3-D feature space. K-mean clustering (Macqueen, 1967), an unsupervised learning algorithm, was subsequently implemented as follows: 1) standard spike train simulations generated in the prior study (Kumbhare and Baron, 2015) served as the initial group centroids for clustering, 2) based upon the closest Euclidean distance from the group centroids, the neuronal recording data were assigned distinct clusters of firing patterns, 3) when all the observations were assigned, the

positions of the cluster centroids were recalculated, and 4) lastly, the object assignment and centroid re-calculations were repeated until the centroids were fixed at their position.

4.2.8. Further characterization of spike trains and correlation analyses

Burst detection and characterization: For each bursty neuron, individual burst epochs were delineated using the interval method, implementing the following previously established criteria (Baron et al., 2011) (Kumbhare and Baron, 2015): Maximum interval to start burst = 6 ms, maximum interval to end burst = 9 ms, minimum interval between bursts = 20 ms, minimum duration of burst = 5 ms, and minimum number of spikes in a burst = 3. Subsequently, the following parameters were defined: burst rate (or bursts per minute (BPM)), burst percentage (BP, percentage of spikes in bursts), intra-burst spike frequency, mean inter-burst interval, and burst order (BO, average number of spikes per burst).

Pause Detection: Pauses in neuronal discharge activity were defined based on following criteria: ISI duration > 300 ms, one spike only for duration > 500 ms, or ISIs $\geq$ 25 times the median interspike interval of the cell (Ko, et al., 2013) (Elias, et al., 2007).

Stationarity test: In addition to generating non-stationarity metric values, an additional stationarity test was employed to further address potential changes in rate or pattern activity (Tuckwell, 1989). Long stable spike recording periods of 15-20 min. during which the rat remained completely at rest were assessed here. Smoothened firing rate and regularity curves were plotted (bin size = 500 ms) to detect any significant transients or changes.

Oscillation trends: To assess for oscillatory activity, autocorrelations and power spectrums were determined for the spike trains using a bin size of 1/2*maximum frequency. The time axes were divided into small intervals and power spectrums for each interval were calculated.

Correlations with severity of dystonia: Effected animals were readily grouped into those with milder and those with more prominent dystonia. As such, to assess for correlations between the neuronal discharge activity and the severity of dystonia, affected rats were divided into two groups: ‘dyst-1’: CS 1-2 and ‘dyst-2’: CS 2.5-4. Also for purposes of assessing neuronal correlations of dystonia, neuronal recording data from normal animals (‘dyst-0’) were utilized here for control data.

4.2.9. Statistics

Statistical analyses were performed using MATLAB. Indifference between means of characteristic metrics of the two phenotypically similar groups (non-carriers and non-jaundiced heterozygous Gunn rats) and between different recording conditions were assessed with two one-sided tests (TOSTs) for equivalence (Schuirmann, 1987) (Wellek, 2010). The mean values were considered to be significantly equivalent ($\alpha = 0.05$) if the 90% confidence interval was within the defined zone of indifference (± 5 spikes/sec for discharge rates and ± 0.2 for the tri-components). The presence of unimodality versus bimodality was assessed using biomodality coefficient (BC) (Ellison, 1987) and Hartigan’s dip statistics (HDS) (Hartigan and Hartigan, 1985). Values of BC > 5/9 implies a bimodal or multimodal distribution. Similarly, HDS values < 0.05 indicate significant bimodality, with values 0.05-0.10 suggesting bimodality with marginal significance. Differences in population distributions within the same and between different groups (nuclei, neuronal types, or dystonia level) were assessed with one and two sample t-Tests. Difference between means of discharge rates, tri-component metrics, and burst parameters between groups were assessed using independent two sample t-Tests. Differences were determined to be

statistically significant for p values less than 0.05. Significance is designated in the tables and figures as follows: *p < 0.05, **p < 0.01, ***p < 0.005, ****p < 0.001.

4.3. RESULTS

4.3.1. Clinical characteristics of dystonic animals

Table 4.1 summarizes the clinical features of the animals. Of 49 dystonic animals, 7 rats were subjectively scored as slight to mildly dystonic (dyst-1) and 18 as moderate (dyst-2) and together compromised the dystonic recording cohort. The remaining 24 dystonic rats were severely affected (dyst-3) and either died or were considered too moribund to tolerate the surgery. EMG recordings from hip and stifle muscles in all rats were silent at rest and exclusively, in dystonic rats, showed characteristic 4-7 Hz co-activation of antagonistic muscle pairs during spontaneous movement (Chaniary et al., 2008).

Table 4.1. Summary of clinical characteristics and data collection

Groupings	Dyst-0	Dyst-1	Dyst-2	Dyst-3
Number of rats	34	7	18	24
Dystonia severity	None	Slight to mild	Moderate	Severe
Gait	Normal gait	Mild gait abnormality	Prominent spread of hindlimbs	Moribund with inability to ambulate
Righting reflex	Normal	Prolonged	Impaired	Absent
Final clinical score (mean ± SD (range))	0	$1.2 \pm 0.2^{D0***}$ (1-2)	$2.8 \pm 0.3^{D0\&D1***}$ (2.5-3)	$4.0 \pm 0.33^{D0,D1\&D2***}$ (3.5-5)
EMG during limb movement	No co-contractions	Occasional co-contractions in antagonistic muscle pairs	Frequent co-contractions of antagonist pairs and multi-joint	NA
Hind paw spread (mm)	35.4 ± 3.7	$40.2 \pm 2.3^{D0***}$	$47.2 \pm 4.6^{D0\&D1***}$	NA

Mean number of nuclei (GP, STN, EP) recorded per rat	1.6 ± 0.3	1.9 ± 0.2	1.3 ± 0.2	NA
Number of analyzable neurons	344	70	184	NA

**p < 0.05, **p < 0.01, ***p < 0.005, ****p < 0.001 (for all figures and tables).*

$^{D0, D1, D2}$denote significant differences from dyst-0, dyst-1, and dyst-2 groups, respectively.

Table 4.2. Patterned activity of neurons

Pattern	GP			STN			EP		
	Normal	Dyst-1	Dyst-2	Normal	Dyst-1	Dyst-2	Normal	Dyst-1	Dyst-2
Total	122	31	70	102	13	42	120	26	72
Regular	68 (55.7%)	1 (0.03%)	2 (0.03%)	51 (50.0%)	0	0	64 (53.3%)	1 (0.04%)	0
Irregular	51 (41.8.7%)	20(64.5%)	31 (44.3%)	46 (45.1%)	7 (53.8%)	23 (54.7%)	54 (45%)	17 (65.3%)	36 (50%)
Bursty	1 (0.01%)	9 (29.0%) ^{I*}	36 (51.4%) ^{D1*}	1 (0.01%)	6 (46.1%)	19 (45.2%)	0	7 (26.9%) ^{I*}	31 (43%)
Non-stationary	2 (0.02%)	1(0.03%)	1 (0.03%)	4 (0.04%)	0	0	2 (0.02%)	1 (0.04%)	5(0.07%)

Data expressed as number of neurons and values in parenthesis represent population percentage in the nuclei.

^{D1}denotes significant differences compared to dyst-1, ^{I}compared to irregular populations of the same nuclei.

4.3.2. Assessment for influences of strains of rats and recording conditions.

The two clinically normal groups, non-carriers (n = 15) and non-jaundiced heterozygous Gunn rats (n = 19), showed equivalent pattern metrics (irregularity, burstiness and corruption) and mean rates (all $p < 0.05$, two one-sided test for equivalency). After affirming that these neuronal properties were indistinguishable between these two groups, the data were combined for further analyses. Additionally, neuronal spike trains (n = 19) collected in GP in two drug free, non-jaundiced heterozygous Gunn rats after acclimating them to the head restraint for 2-3 hrs per day for 2 days were compared to GP recordings (n = 103) collected under the standard protocol of recording beginning 2-3 hrs after placement of burr holes under brief general anesthesia and 2-3 hrs after buprenorphine administration. The tri-component mean values and mean rates were

equivalent between both testing conditions (each $p < 0.05$, two one-sided test for equivalency), thereby supporting a lack of significant influence of drugs or head restraint on the neuronal recordings. These data were thus combined for further analyses.

4.3.3. Distinctive neuronal dichotomy in normal and dystonic rats.

Tri-component metrics histograms. In total, in the three basal ganglia nuclei, 344 neurons were recorded in 34 normal rats and 254 neurons in 25 dystonic rats (Tables 4.1 and 4.2). In normal and dystonic alert rats at rest, all three nuclei showed two physiologically distinct neuronal populations, with modest differences between nuclei (fig 4.2a-f). However, the neuronal properties differed markedly between normal and dystonic rats. In normal rats, the bimodalities of the three nuclei were apparent in the regularity spectrums (fig 4.2a; bimodality coefficient, BC: GP = 0.786, STN = 0.763, EP = 0.803; Hartigan's dip statistics (HDS): GP = 0.033, STN = 0.030, EP = 0.036, with each HDS, $p < 0.05$), while in dystonic rats, the bimodalities were revealed by the burstiness spectrums (fig 4.2e,f; dyst-1: BC: GP = 0.687, STN = 0.609, EP = 0.677; dyst-2: BC: GP = 0.792, STN = 0.777, EP = 0.806; HDS: each $p < 0.05$). While the normals had left-sided unimodal thin-tailed burstiness histograms indicating a scarcity of burst firing in these nuclei (fig 4.2d), the dystonics showed right-sided regularity distributions indicating a scarcity of regular tonic units (fig 4.2b,c).

K-mean clustering and additional pattern characterizations. Using K-mean clustering, the tri-component classifier grouped the combined normal rat populations into two distinct categories (fig 4.3a): 1) moderately fast and regular (38.1 ± 16.7 spikes/sec) and 2) slow and irregular (18.7 ± 7.9 spikes/sec). In individual nuclei, the numbers of regular tonic units exceeded irregularly

patterned neurons, but these differences did not reach significance (GP = 15.7%, $p = 0.107$; STN = 4.9%, $p = 0.612$; EP = 8.3%, $p = 0.359$).

In marked difference, in dystonic rats, regardless of clinical severity (fig 4.3b,c), neurons in all three nuclei were characterized as 1) slow and irregular (12.4 ± 6.4 spikes/sec) or 2) slow and bursty (14.8 ± 7.5 spikes/sec). Accordingly, large differences in mean burstiness metric values were evident between irregular and bursty neuronal populations in all three nuclei (0.03-0.17 vs. 0.87-0.95, each $p < 0.05$) in dystonics. The total burst percentage (BP) for bursty neurons was greater than 42% in all three nuclei vs less than 8% in the irregular dystonic populations (each $p < 0.05$). None of 23 bursty neurons in dyst-1 and 3/86 in dyst-2 rats showed oscillatory activity. None of these oscillatory neurons showed a dominant peak in their power spectra to indicate rhythmic discharge activity. No neurons in dystonic or normal rats exhibited significant pauses.

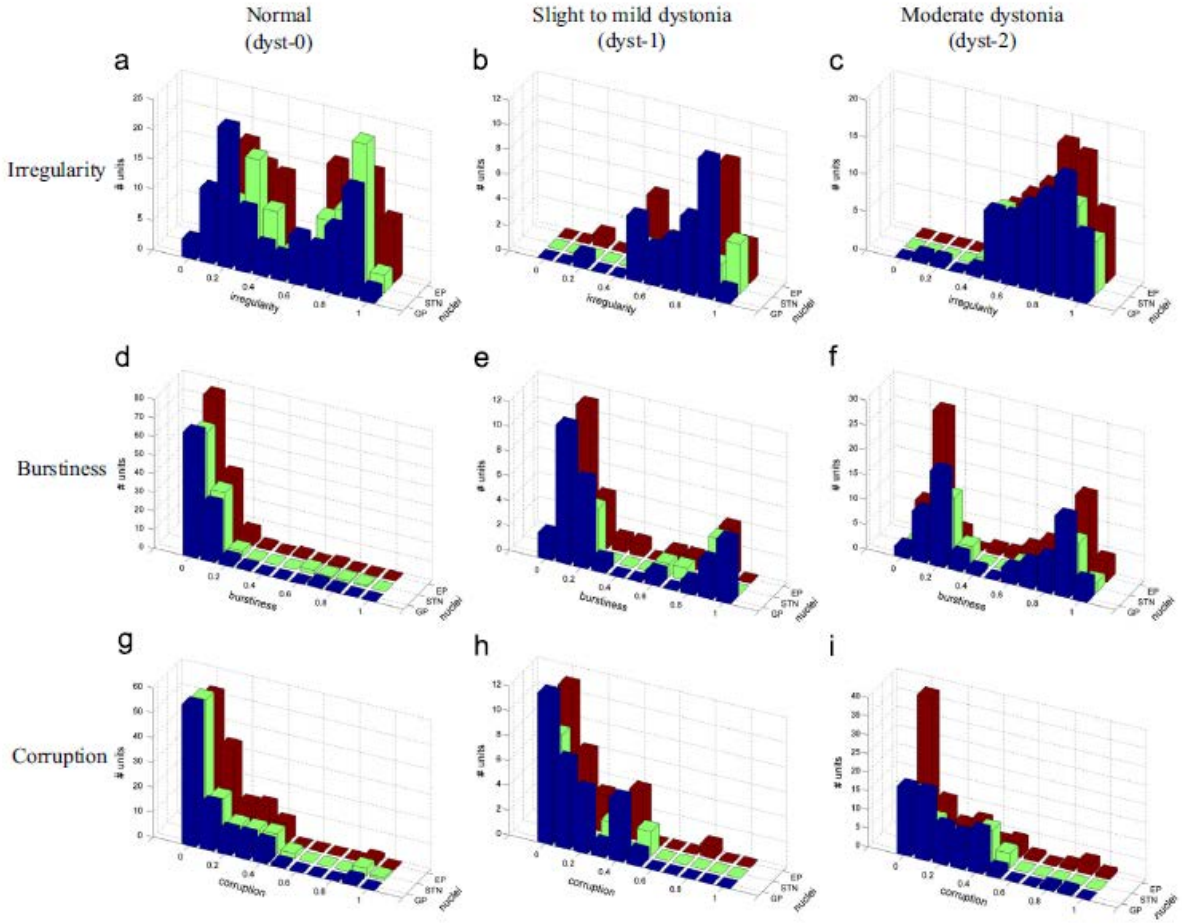

Fig. 4.2. Tri-component metrics histograms for GP, STN and EP grouped by severity of dystonia. Top row: (a) in normal (dyst-0) rats, distinct bimodalities in the regularity spectrums define two different populations (HDS all $p < 0.05$). In distinction from normal rats, in **(b)** slight to mild (dyst-1) and **(c)** moderately dystonic (dyst-2) rats, most units show relatively large irregularity values, indicating a scarcity of regular tonic units. **Middle row: (d)** in normal rats, the leftward short-tailed burstiness distributions indicate a paucity of normal burstiness in resting rats in all 3 nuclei. In contrast, in dystonic rats, **(e,f)**, distinct bimodalities in the burstiness spectrums define two different populations (HDS all $p < 0.05$), with the level of burstiness increasing with increasing severity of dystonia. **Bottom row:** leftward, short-tailed corruption metric distributions **(g-i)** indicate that the discharge properties of these neurons are highly stationary without appreciable change in discharge patterns over time, supporting a true physiological bimodality in these nuclei in normal and dystonic rats in the alert resting state.

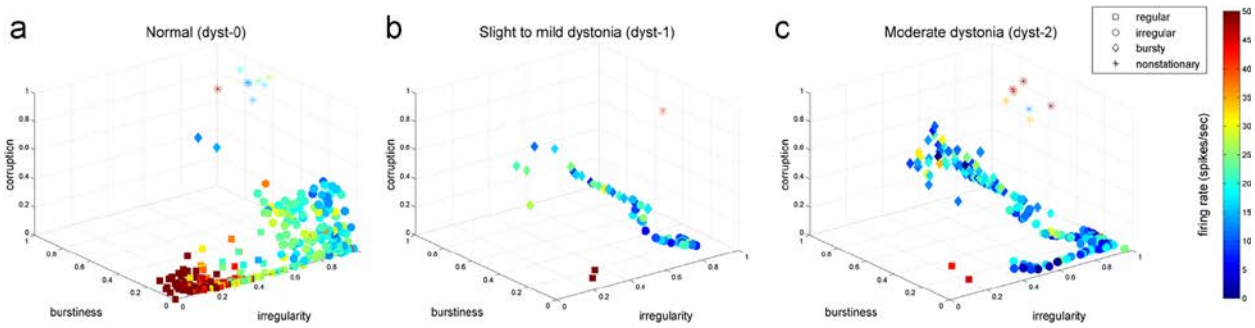

Fig. 4.3. K-mean clustering and rate distributions in 3D feature space. (a) In normal rats, the grouped neurons (GP, EP and STN) can be seen to be chiefly 1) moderately fast and regular or 2) slower and irregular, while **(b,c)** in dystonic rats, the neurons are overall abnormally slow and 1) highly irregular or 2) bursty. Because the semi-automated 3D K-mean clustering method simultaneously uses three independent metric properties to classify neuronal populations based on closest distance from adaptive group centroids (and not specific thresholds), modest overlap in single discriminatory metric spectrums is apparent.

Support for two distinct neuronal populations. Frequent simultaneous recordings of two distinct neuronal units from the same microelectrode (e.g., regular and slower irregular neurons in normal rats, fig 4.4) support the unlikelihood that the two defined neuronal patterns represent different behavioral conditions or levels of alertness or that the two types of neurons are spatially dispersed in the nuclei. Further, the leftward and short tailed corruption histograms (fig 4.2g-i) indicate low overall corruption values and that the neurons in all three nuclei in both normal and dystonic rats exhibited stable firing patterns without appreciable change in their characteristic firing patterns over time. Additionally, during longer recordings of 15-20 min from representative neurons (n = 6), the patterns and mean rates continued to remain fully stable (maximum deviation from mean value: instantaneous rate < 5 spikes/ sec and irregularity < 0.2) in alert rats at rest (fig 2.7).

Refer to Table 4.2 for a summary of the distribution of recorded neurons for each nuclei separated by severity of dystonia (dyst-0, dyst-1 vs dyst-2), to Table 4.3 for the details on discharge rates, and to fig 4.5 for examples of the characteristic discharge patterns, along with grouped interspike interval (ISI) histograms.

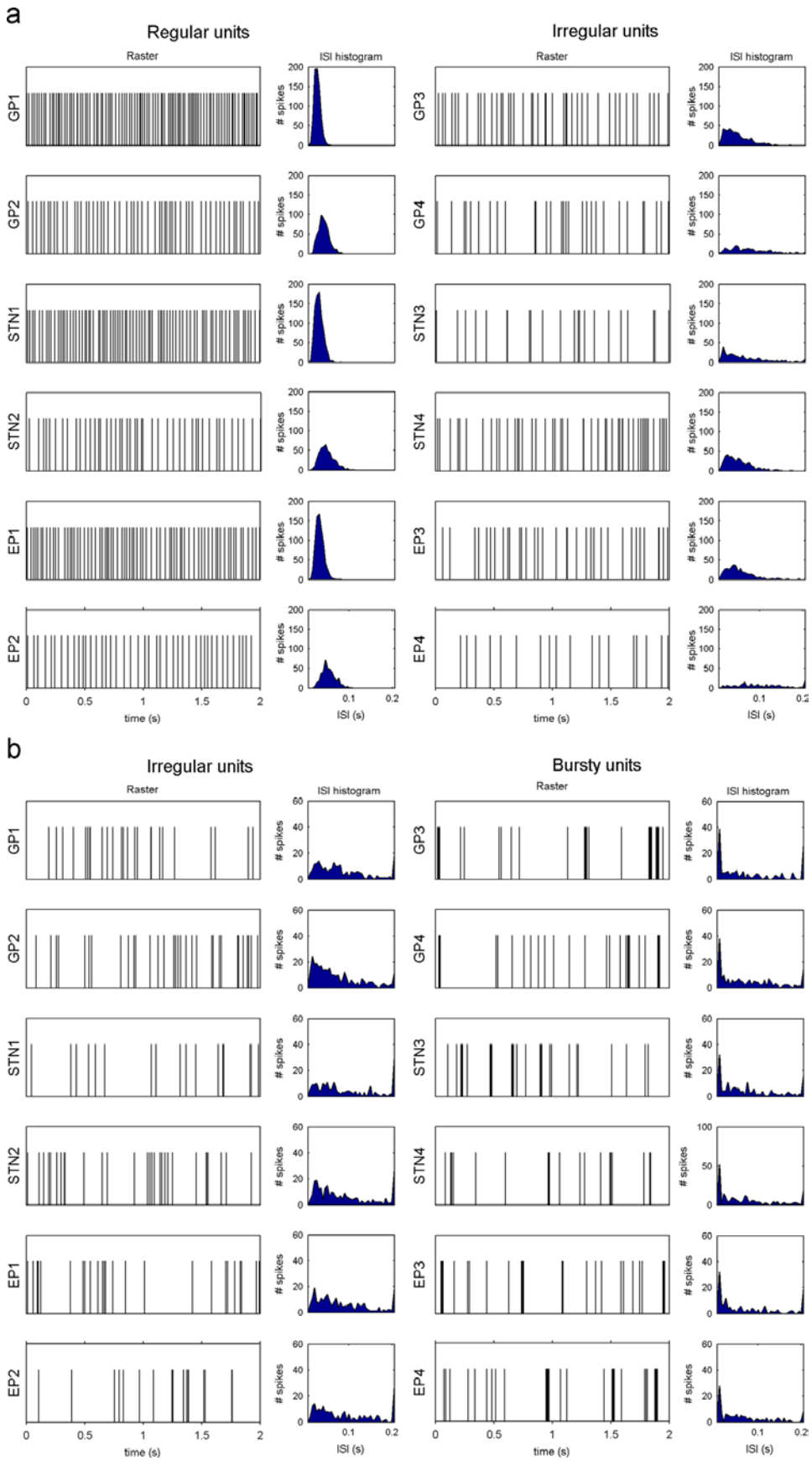
a
Regular units
Irregular units
Raster
ISI histogram
GP1
GP2
STN1
STN2
EP1
EP2
GP3
GP4
STN3
STN4
EP3
EP4
spikes
time (s)
ISI (s)
b
Irregular units
Bursty units

Fig. 4.4 Representative spike raters in normal and dystonic rats at rest. The figures illustrate two examples of spike rasters for each of the two principal types of neurons observed in each nucleus in normal and dystonic rats. (a) As evident from the raster profiles and ISI histograms, neurons recorded from the motor territories of GP, STN, and EP in normal alert, resting states were characterized by either moderately fast and regular or slow and irregular discharge activity, without appreciable bursting. (b) In contrast, in dystonic animals, neurons can be seen to discharge slowly in either an irregular or bursty pattern, with modest differences between nuclei.

4.3.4. Comparisons between nuclei and influence of severity of dystonia

Population distributions. In dyst-1 rats, GP and EP showed greater numbers of irregulars than bursty neurons (both GP and EP, $p < 0.05$; Table 4.2). In STN, the number of recorded neurons in dyst-1 rats was insufficient to adequately assess for potential similar differences ($p = 0.785$). In contrast, in dyst-2 rats, irregular and bursty neurons were distributed in comparable numbers in each nucleus (each $p > 0.539$). Among dystonic rats, 29% of neurons in GP, 46% in STN, and 27% in EP were classified as bursty in dyst-1 rats compared to 51%, 45%, and 43%, respectively in dyst-2 rats (Table 4.2), with differences reaching significance in GP ($p < 0.05$), but not in EP ($p = 0.152$) and STN ($p = 0.955$).

Rates. In normal rats, mean discharge rates were significantly higher in GP (37.4 ± 14.8) than in STN (28.8 ± 14.4, $p < 0.001$) and EP (32.0 ± 14.3, $p < 0.005$), with no differences between STN and EP ($p = 0.099$). The average grouped discharge rates for regular and for irregular patterned neurons did not differ significantly between nuclei.

Mean discharge rates were reduced by 51.3% in GP, 44.8% in STN, and 46.8% in EP in dyst-1 compared to normal rats and by 64.8%, 41.6%, and 62.4%, respectively, comparing dyst-2 to normal rats (all $p < 0.001$; fig 4.6a). Discharge rates were reduced by 23.8% in GP and 24.2% EP (both $p < 0.05$) in dyst-2 (av. 17-18 spikes/sec) compared to dyst-1 rats (12-13 spikes/sec), but did not differ in STN with increasing severity of dystonia ($p = 0.321$).

Among dyst-1 and dyst-2 rats, overall mean firing rates were significantly slower specifically in EP compared to STN in dyst-2 rats (by 41.6%, $p < 0.01$; fig 4.7a). Average discharge rates of irregular vs bursty neurons differed specifically in STN and EP in dyst-2 rats (dyst-1, GP, STN and EP: each $p > 0.411$; dyst-2, STN: $p < 0.05$, EP: $p < 0.01$, GP: $p = 0.171$; Table 4.3. Also, refer to fig 4.3b and c for collected rate distributions in dyst-1 and dyst-2 rats, respectively).

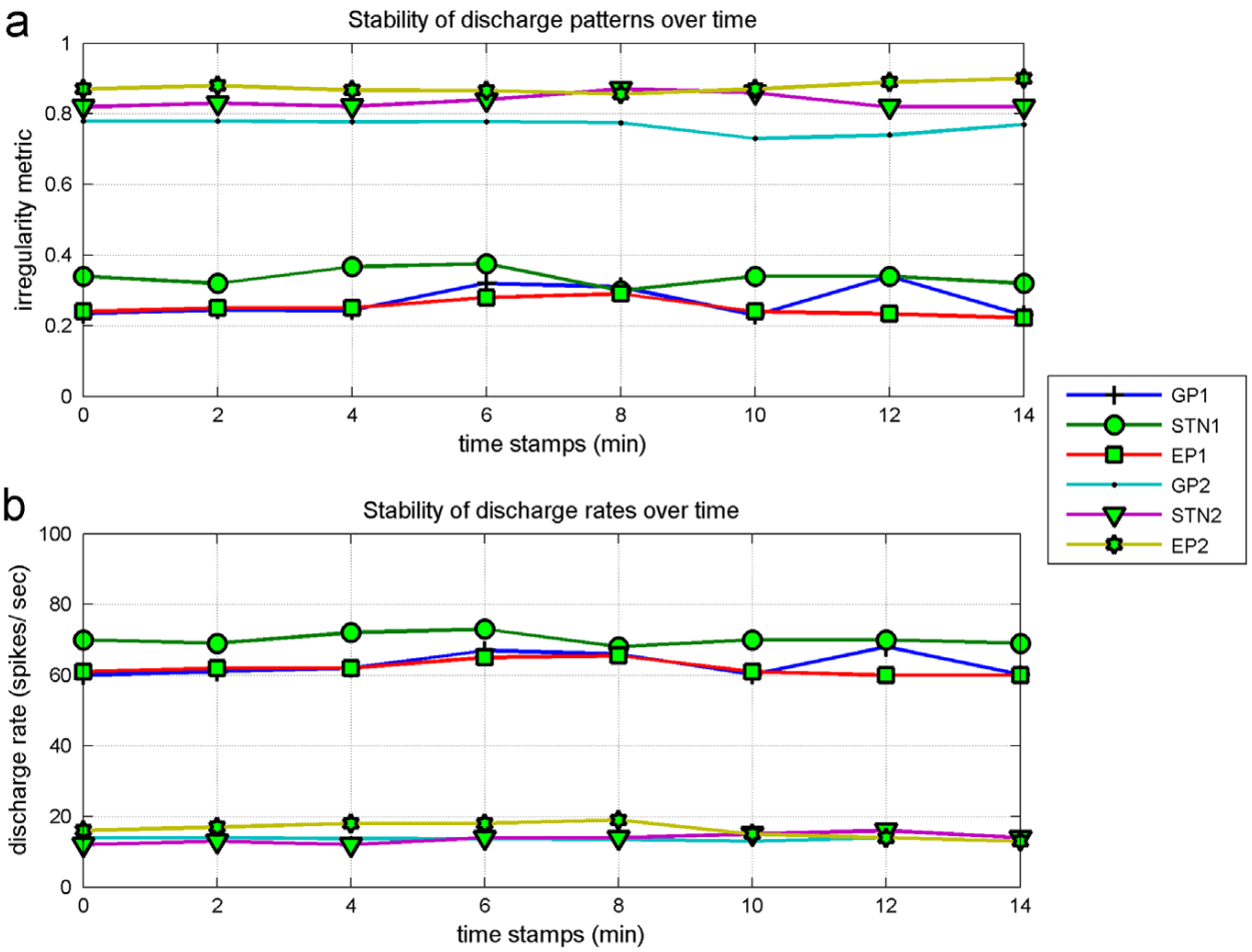

Fig. 4.5: Stability of discharge patterns and rates during prolonged recordings. a. The regularity-time and **b.** rate-time curves of 6 representative neurons from GP, STN and EP all demonstrate highly constant properties in rats in a resting state (14 min displayed). The prolonged recordings support the unlikelihood that a single neuronal population could account for the two distinct types of neurons demonstrated here in vivo.

Irregularity. In normal rats, in each nuclei, irregularity correlated strongly with discharge rates of regular discharging neurons ($r = -0.74$ to -0.82, all $p < 0.001$) and weakly with rates of irregular units ($r = -0.29$ to -0.35, all $p < 0.001$). In all three nuclei, neurons showed appreciably greater

overall irregularity in dyst-1 compared to normal rats (each $p < 0.001$; fig 4.6b). In GP and EP, but not in STN, neurons showed further increased irregularity in dyst-2 vs dyst-1 rats (GP: $p < 0.05$, EP: $p < 0.01$, STN: $p = 0.867$).

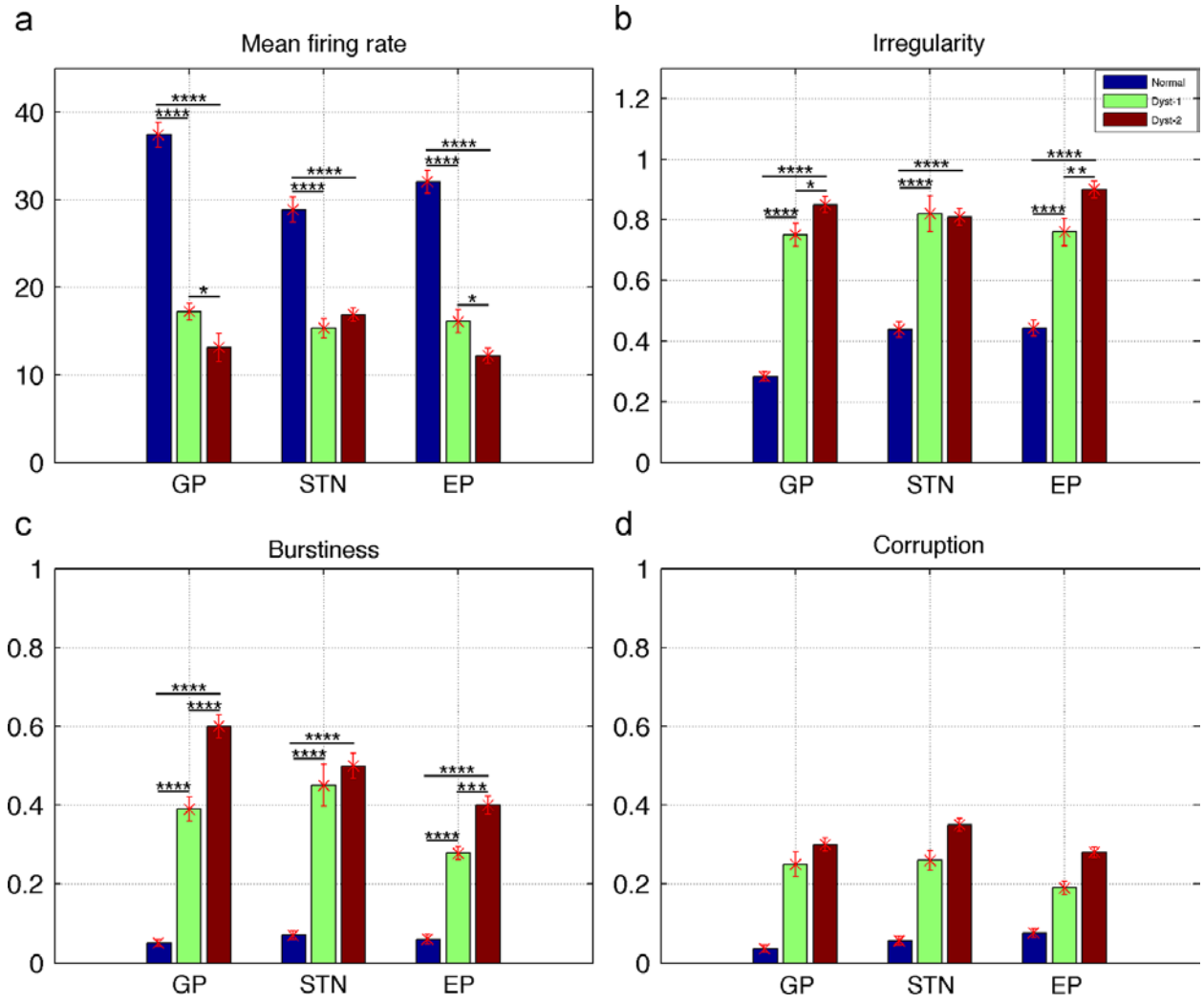

Fig. 4.6. Influence of severity of dystonia on neuronal discharge properties in GP, STN and EP. (a) Neuronal discharge rates were overall greatly reduced in dyst-1 compared to normal rats in all 3 nuclei, and mildly further reduced in GP and EP in dyst-2 compared to dyst-1 rats. **(b)** Neuronal discharge activity was appreciably more irregular in dyst-1 than normal rats, with the irregularity level in GP and EP increasing mildly in relation to increasing severity of dystonia. **(c)** With induction of dystonia, burstiness became prevalent in all 3 nuclei and was more prominent in GP and EP in dyst-2 vs dyst-1 rats. **(d)** With the induction of dystonia, non-stationarity levels increased, but remained within acceptable limits. Error bars indicate standard errors (for all figures). *$p < 0.05$, **$p < 0.01$, ***$p < 0.005$, ****$p < 0.001$ (for all figures and tables).

In dyst-1 rats, no significant differences in irregularity were observed between nuclei (each $p > 0.302$; fig 4.7b). Among dyst-2 rats, neurons showed greater overall irregularity in EP than in

GP and STN (both $p < 0.05$), without significant differences between GP vs STN ($p = 0.314$). Among irregular neurons, EP alone showed significant increment in irregularity in dyst-2 compared to dyst-1 rats (EP: $p < 0.05$, GP and STN: $p > 0.154$; fig 4.8a) and among irregular neurons, EP showed greater irregularity compared to STN ($p < 0.01$) and GP ($p < 0.05$) in dyst-2 rats.

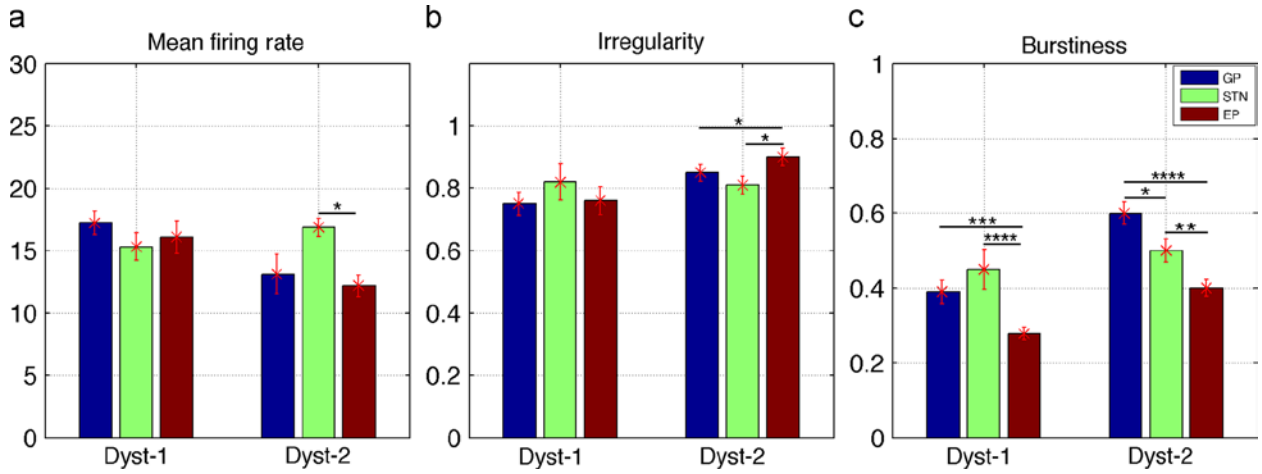

Fig. 4.7. Inter-nuclei comparisons at different levels of severity of dystonia (a) EP showed significantly slower mean firing rates than STN in dyst-2 rats. **(b)** EP showed greater irregularity than GP and STN in dyst-2 rats. **(c)** GP and STN showed significantly greater burstiness than EP in both dyst-1 and dyst-2 groups. GP showed significantly greater overall burstiness than STN in dyst-2 rats.

Burstiness. With increasing severity of dystonia, overall burstiness increased significantly in GP ($p < 0.001$) and EP ($p < 0.005$), but not in STN ($p = 0.429$; fig 4.6c). Comparing nuclei (fig 4.7c), GP and STN showed significantly greater burstiness than EP in both dyst-1 (GP vs EP: $p < 0.005$, STN vs EP: $p < 0.001$) and dyst-2 rats (GP vs EP: $p < 0.001$, STN vs EP: $p < 0.01$). While showing comparable burstiness in dyst-1 rats, GP showed greater burstiness than STN in dyst-2 rats, attributable to the increment in burstiness in GP (GP vs STN, dyst-1: $p = 0.304$, dyst-2: $p < 0.05$; fig 4.7c).

Among bursty neurons, no significant differences were evident in the level of burstiness between dyst-2 vs dyst-1 groups or between nuclei (fig 4.8b), except for modest greater

burstiness in EP than in STN in dyst-2 rats ($p < 0.05$; all other comparisons, $p > 0.160$). On the other hand, BP of bursty neurons was significantly greater in GP (av. 66-68%) vs STN (42-46%) and vs EP (49-51%; GP vs STN: $p < 0.001$ for both dyst-1 and dyst-2; GP vs EP: $p < 0.05$ for dyst-1 and $p < 0.01$ for dyst-2; table 4.4). EP bursty neurons had significantly higher BP than STN in dyst-2 ($p < 0.05$), but not in dyst-1 rats ($p = 0.336$). GP bursty neurons had considerably faster mean intra-burst discharge frequencies (av. 262-271 spikes/sec) than STN (190-241 spikes/sec) and EP neurons (189-230 spikes/sec) in dyst-2 rats (both $p < 0.001$), without significant differences between STN and EP ($p = 0.693$). Burst per minute (BPM) was greater for bursty neurons in STN (122/min) than in GP (av. 94/min) and EP (78/min) (GP vs STN: $p < 0.05$; STN vs EP: $p < 0.001$), while no differences were evident between GP vs EP ($p = 0.154$). The average burst order (BO) of bursty neurons was greater in GP and EP (both av. > 5 spikes per burst) compared to STN (av. 4 spikes per burst), with both differences $p < 0.05$. Average burst durations did not differ significantly between bursty neurons of different nuclei ($p > 0.23$).

Table 4.3. Resting discharge rates

Dystonia levels	Pattern	GP	STN	EP
Normal	Regular	$41.17 \pm 13.5^{I****}$	$38.21 \pm 18.1^{I****}$	$35.22 \pm 18.8^{I****}$
	Irregular	19.52 ± 7.4	19.01 ± 7. 4	17.07 ± 8.9
Dyst-1	Irregular	15.25 ± 3.9	14.61 ± 6.7	13.60 ± 5.1
	Bursty	16.85 ± 6.8	16.13 ±7.8	14.24 ± 9.2
Dyst-2	Irregular	14.60 ± 4.3	14.49 ± 7.8	11.6 ± 6.7
	Bursty	16.70 ± 7.4	$18.84 \pm 5.9^{D1*I*}$	$14.4 \pm 5.3^{I**}$

Data expressed as mean discharge rate (spikes/sec) ± SD.
^{D1}indicates significant differences compared to dyst-1, ^{I}compared to irregular populations of the same nuclei.

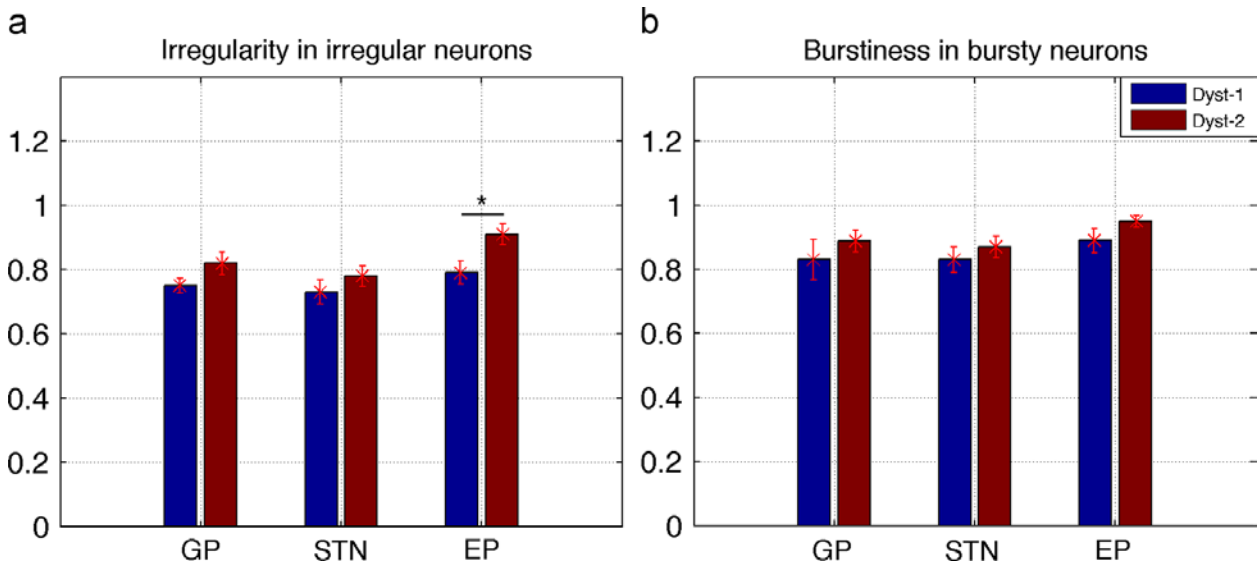

Fig. 4.8. Influence of increasing severity of dystonia on patterned activity in irregular and bursty neurons. With increasing severity of dystonia, **(a)** irregular neurons in EP, but not in GP and STN, were more highly irregular, while **(b)** bursty neurons in EP, STN, and GP did not show further increases in burstiness in dyst-2 compared to dyst-1 rats. EP is modestly burstier than STN in dyst-2 rats ($p < 0.05$, not indicated in figure).

Table 4.4. Characterization of bursty trains in GP, STN and EP in dystonic rats

Dystonia Level	Nuclei	Burst percentage (%)	Burst Order	Burst Duration (ms)	Mean Freq. in burst (spikes/sec)	Bursts Per Minute
Dyst-1	GP	68.1 ± 9.5	5.3 ± 2.2	24.2 ± 3.0	262.5 ± 57.2	109.1 ± 17.6
	STN	46.3 ± 10.4^{G***}	4.1 ± 1.8	17.3 ± 5.6	241.2 ± 52.6	108.6 ± 27.0
	EP	51.2 ± 16.5^{G*}	5.3 ± 1.3	23.5 ± 3.2	230.0 ± 60.1	82.4 ± 45.7
Dyst-2	GP	65.7 ± 29.0	5.7 ± 1.6	21.1 ± 7.9	271.4 ± 42.1	93.7 ± 53.1
	STN	41.8 ± 5.7^{G***}	3.8 ± 0.7^{G*}	20.2 ± 5.8	190.0 ± 45.4^{G***}	122.0 ± 28.8^{G*}
	EP	48.6 ± 11.0^{G**S*}	5.3 ± 1.2^{S*}	28.3 ± 6.6	189.3 ± 56.1^{G***}	78.2 ± 29.1^{S***}

^{G}denotes significance compared to GP, ^{S}compared to STN, and ^{E}compared to EP.

4.3.5. Histology

Silver stain reconstructions of recording tracks affirmed that the microelectrode tracks were localized within the targeted lateral half (purported motor regions) of GP, STN and EP. Fig 4.1d shows examples of two silver stained recording tracks traversing STN.

4.4. DISCUSSION

Due to such influences as anesthesia and inadequate control for movement in previous *in vivo* recording studies in rodents, the numbers of types and physiological characteristics of neurons in GP, STN, and EP has been controversial. While many *in vitro* physiological recording studies in rats suggested that GP is comprised of two types of neurons (Nambu and Llinaś, 1994) (Cooper and Stanford, 2000) (Urbain et al., 2000) (Bugaysen et al., 2010), equally many studies suggested that GP contains a single type of neuron (Chan et al., 2004) (Chan, et al., 2011) (Hashimoto and Kita, 2006) (Günay, Edgerton and Jaeger, 2008). In distinction, previous studies carried out *in vivo* largely revealed two distinct principal neuronal discharge patterns in GP (Mallet et al., 2012) (Benhamou et al., 2012). In STN, recording studies performed utilizing anesthesia had chiefly suggested STN to be comprised of a single population of neurons in rats (Hammond and Yelnik, 1983) (Hollerman and Grace, 1992) (Magill, Bolam and Bevan, 2000) (Kita, Chang and Kitai, 1983). Urbain et al. (Urbain et al., 2000) recorded in unanesthetized rats and also observed a single homogenous population of neurons in STN under varying levels of alertness. In difference from most *in vivo* descriptions in primates, anatomical and *in vitro* studies in rats and primates have largely suggested that EP and GPi are comprised of two distinct types of neurons (Tokuno et al., 1988) (Parent, 2001) (Nakanishi, Kita and Kitai, 1990). In the

only previous investigation of EP performed without anesthesia (Benhamou and Cohen, 2014), neurons were characterized in freely moving rats by a single irregular discharge pattern.

Presently, extracellular neuronal discharge activity was recorded from motor territories of GP, STN and EP in jaundiced dystonic Gunn rats and compared with that of normal rats under similar well-controlled, alert resting states *without movement*. Using the novel pattern classification algorithm, neuronal activity was defined by two dominant discharge patterns, which were similar for the three nuclei, but markedly differed between normal and dystonic conditions. In normal rats, neuronal activity in the three nuclei was heralded by moderately fast and regular (av. 35-41 spikes/sec) or slow and irregular (av. 17-20 spikes/sec) discharge activity compared to generally slower and highly irregular (av. 12-15 spikes/sec) or burst predominant (av. 14-17 spikes/sec) activity in dystonic rats. Burstiness was not a characteristic of neurons in normal rats *at rest*, while regular tonic discharge activity was not a feature of even mildly dystonic animals. Also, pauses in discharge activity were not a feature of neurons in normal and dystonic rats at rest. Further, burst neurons were largely non-oscillatory, and never rhythmical. Low corruption metrics values for each nucleus indicated that neuronal discharge properties remained stable throughout the recordings, supporting that the dichotomous patterned neurons represent two physiologically distinct populations. Extensive recordings from 344 neurons, each for at least 2 minutes and from 6 neurons for 15-20 min in the rest state affirmed that these neurons do not switch between the two basic discharge patterns defined in normal and dystonic rats.

The extent to which differences in intrinsic properties of neurons might contribute to the dichotomous *in vivo* grouping of neurons in the basal ganglia in rats at rest is not clear. Bugaysen et al. (Bugaysen et al., 2010), for instance, investigating cell-attached and whole-cell recordings, differentiated neurons in GP into 2 or 3 groups based on the width of action potentials and other cellular parameters. In contrast, Deister et al. (Deister et al., 2009) observed GP neurons *in vitro* to show the full spectrum from fast regular to slow irregular discharge firing over prolonged recordings. A harmonious explanation could be that GP, as well as EP and STN neurons have the capability of discharging from a spectrum of slower and irregular to faster and regular patterned activity, but that different afferent inputs dictate which of these two predominant normal discharge patterns are displayed at rest. With, for example, motor activity, and associated cortical afferent drive, these neurons show additional features of movement-related bursts and pauses in discharge activity.

Although GP, STN and EP showed similar resting discharge rates and patterns under normal and dystonic states, modest differences in patterned activity were evident between these interconnected nuclei. In dystonic rats, among irregular neurons, the discharge patterns were overall more irregular in EP compared to those in GP and STN, which was more evident in more effected (dyst-2) rats. Among bursty neurons, EP was modestly burstier than GP and STN. For bursty neurons, BPs were modestly greater in GP (av. 66-68%) compared to EP (49-51%) and STN (42-46%), while intra-burst frequencies of burst neurons in GP were considerably faster (av. 262-271 spikes/sec) compared to STN (190-241 spikes/sec) and EP (189-230 spikes/sec). BPM was however greater for bursty neurons in GP (av. 94-109/min) and STN (108-121/min)

than in EP (78-82/min), while BO was greater for GP and EP (both av. > 5 spikes per burst) compared to STN (av. 4). Average burst durations did not differ significantly between nuclei.

In all 3 nuclei, marked reductions in neuronal discharge rates occurred with induction of even mild dystonia. With increasing severity of dystonia, discharge rates in GP and EP were further mildly reduced. With increasing severity of dystonia, further moderate increases in burstiness and more modest increases in irregularity were evident in GP and EP, but not in STN. With the exception of reduced mean intra-burst frequencies in STN and EP, burst properties of bursty neurons (BP, BPM, BO, and burst duration) did not change with increasing severity of dystonia. While exceedingly rare in normal rats, 32% of neurons in GP and 27% in EP were classified as bursty in dyst-1 rats compared to 50%, and 43%, respectively in dyst-2 rats. Therefore, the increases in proportions of bursty neurons with worsening dystonia could chiefly account for the observed increases in burstiness and irregularity in GP and EP with worsening dystonia. The number of neurons recorded in STN in dyst-1 rats was insufficient to adequately assess for potential similar increases in the percentage of bursty neurons with worsening dystonia. Because kernicterus is associated with a loss of neurons in these nuclei, the alterations in the ratios of burst to irregular neurons with worsening dystonia may represent differential vulnerability of these two populations to the effects of bilirubin toxicity. Although the possibility that the observations here represent non-pathological epiphenomena cannot be excluded, the findings of prominent, highly abnormal burstiness in mildly affected Gunn rats and appreciably greater burstiness with increasing severity of the dystonia implicate burstiness as likely to be playing a principal pathological role in the manifestation of dystonia and its progression.

In mature organotypic cortex-striatum-STN-GP cultures prepared from normal rats, Plenz and Kital (Plenz and Kitai, 1999) observed that GP and STN neurons discharged in a burst fashion with prominent synchrony within and between these nuclei. Severing GP-STN connecting fibers altered the discharge of STN neurons to a regular tonic pattern. Because sectioning the cortical inputs to STN did not significantly impact this relation or the discharge rates in GP, the investigators suggested that GP-STN reciprocal connections serve as a basal ganglia pacemaker. Others however, have provided contrary evidence to suggest that cortical inputs might be necessary to drive burst activity between GP and the STN (Baufreton et al., 2005). Moreover, because the organotypic cultures lacked dopamine (DA) input and because burst activity is prevalent in Parkinson's disease (PD), a DA deficient condition, spontaneous burst activity in the basal ganglia has been suggested to be pathological. The findings of prominent bursting in GP, STN, and EP in dystonic Gunn rats and a lack of bursting in normal rats in an alert resting state support contentions that cortical or other external drive is normally required for bursting in these nuclei and that spontaneous bursting is therefore indicative of a pathological state. Bevan and colleagues (Sidibe et al., 1997) showed that electrical stimulation of GABA inhibitory potentials in GP *in vitro* hyperpolarizes STN neurons, producing rebound depolarization and in turn, prominent burst discharge activity. While the origin of spontaneous bursting in the basal ganglia in such conditions as dystonia and PD remains to be determined, this observation provides at least one plausible mechanism by which GP could contribute to pathological burst activity.

The present findings of slow, irregular burst discharge activity in dystonic Gunn rats are consistent with most observations in humans with various forms of dystonia undergoing DBS surgery (Lenz et al., 1998) (Merello et al., 2004) (Sanghera et al., 2003) (Vitek et al., 1999)

(Zhuang, Li and Hallett, 2004) (Starr et al., 2005) (Moll et al., 2014) (Schrock et al., 2009). Although modest differences have been reported between primary and secondary forms of dystonia, this has not been comprehensively investigated in part due to limitations of human studies, and the findings have differed between studies (Zhuang, Li and Hallett, 2004) (Lozano et al., 1997). Because GPi is by far the most commonly targeted nucleus for treating dystonia, it has been most extensively investigated in humans with dystonia. The discharge pattern has been described as dominated by grouped burst discharges on a particularly silent background, in difference from irregular tonic discharge activity in normal monkeys (Vitek et al., 1999). In one investigation of GPe (Vitek et al., 1999), the neuronal activity similarly showed reduced discharge rates and prominent burst activity compared to normal monkeys. In contrast, another group (Starr et al., 2005) did not find definite abnormalities in GPe apart from occasional atypical oscillations. In another study (Moll et al., 2014), patients with cervical dystonia showed reduced mean discharge rates in GPi, but not in GPe, on the side ipsilateral relative to the side contralateral to the direction of head turning. Of note, while the motor portion of GPi is specifically targeted during the DBS surgeries, the microelectrode tracks however may not necessarily similarly traverse the affected motor territory of GPe.

In one investigation of STN in dystonic patients (Starr et al., 2005), the neuronal discharge activity was dominated by irregular grouped discharges, but without clear alterations in the discharge rates compared to normal monkeys. In a larger investigation of STN in primary dystonias (Schrock et al., 2009), the discharge rates were found to average 26 spikes/sec compared to 36 spikes/sec in patients with PD. Prominent bursting was evident in both dystonia and PD subjects. Oscillatory activity was also evident in both groups, but was comparatively less prominent in dystonic subjects. Other groups have also reported neuronal oscillatory activity in

GPi, and to a lesser extent in GPe, in dystonic patients (Chen et al., 2006) (Moll et al., 2014). While oscillatory activity was not a characteristic feature of neurons in dystonic Gunn rats, this could potentially represent differences between various primary and secondary dystonias, differences in dystonia severity, or species differences. With respect to severity of dystonia, none of the rats had fixed dystonia or other features of more severe dystonia and oscillations were evident in 3/85 bursty neurons in moderately dystonia versus 0/23 bursty neurons in mildly affected rats. However, the sample sizes here were insufficient to adequately assess for potential correlations between oscillations and severity of dystonia.

In contrast to the extensive neurophysiological investigations in rodent and primate models of PD, only a paucity of studies have been previously conducted in animal models of dystonia. In MPTP-treated monkeys, Perlmutter and colleagues showed that transiently induced dystonia was temporally correlated with transient reductions in DA D2-like receptor binding in MPTP-treated monkeys (Perlmutter et al., 1997). This would be expected to produce disinhibition of striatal medium spiny GABAergic neurons and in turn, cause excessive inhibition of GP, consistent with findings of reduced discharge rates in GPe/GP in humans and dystonic Gunn rats. Early investigations of dystonia in rodents were limited to neurophysiological recording studies performed utilizing anesthesia in dt^{sz} hamsters, which exhibit paroxysmal dystonia in response to prolonged stress (Richter and Loscher, 1993) (Merello et al., 2004) (Loscher et al., 1989). Nambu and colleagues (Chiken, Shashidharan and Nambu, 2008) (Nambu et al., 2011) more recently recorded neuronal activity in a mouse model of human DTY1 genetic dystonia without the use of sedation. These mice however show prominent hyperkinesia with modest evidence of dystonia. The investigators reported reduced discharge rates, as well as bursts and pauses in GP

and EP, though did not control for movement or assess specifically for dystonia during the neuronal recordings.

In summary, in the present investigation of dystonic Gunn rats at rest, neurons in GP, STN and EP were found to exhibit marked reductions in discharge rates, an absence of regular tonic discharge activity, and prominent abnormal burst activity. The extent of neuronal burstiness, in particular, correlated with the severity of dystonia. As for normal rats, a distinct neuronal dichotomy (albeit, pathological) was evident in each of these nuclei, further supporting that, at least *in vivo*, two principal types of neurons exist in each of these nuclei. A number of groups have observed in humans that patterned discharge activity in GPi (Vitek et al., 1999) (Zhuang, Li and Hallett, 2004) and the thalamus (Zhuang, Li and Hallett, 2004) (Lenz et al., 1999) correlate with dystonic EMG activity. Further, Lenz and colleagues (Lenz et al., 1999) showed that the thalamic neuronal activation *preceded* the correlated dystonic EMG activity. Preliminarily, as it was reported (Baron et al., 2011) that, GP appears to show prominent abnormal synchronized neuronal silencing, while EP predominately shows abnormal synchronized activation preceding dystonic motor activity in Gunn rats. It was therefore postulate that on a background of highly irregular and bursty discharge activity, cortical motor-related signals lead to excessive non-selective silencing of GP/GPe neurons, which causes excessive, unselective disinhibition of EP/GPi and, in turn, produces excessive, unselective cortico-thalamic motor drive as the physiological basis of dystonia. Additional studies in humans and animal models will be important towards defining pathological differences in primary and secondary dystonias to account for the contrasting responses to DBS surgery in these conditions.

CHAPTER 5

PARKINSONISM AND DYSTONIA ARE DIFFERENTIALLY INDUCED BY MODULATION OF DIFFERENT TERRITORIES IN THE BASAL GANGLIA

5.1. Introduction

Despite their outward differences, the pathophysiology of PD and dystonia appear to be closely related. For instance, degeneration of dopaminergic neurons in the substantia nigra pars compacta causes the principal parkinsonian motor features in PD, while genetic defects in dopamine (DA) production lead to dopa-responsive dystonia (Knappskog, Flatmark, Mallet, Ludecke, & Bartholome, 1995). Further, dystonia is a common symptom of PD, while parkinsonism is often a feature of dopa-responsive dystonia. Both parkinsonism (Kuoppamaki, et al., 2005) and dystonia (Münchau, et al., 2000) have been reported subsequent to strokes in the globus pallidus (GP). Unfortunately, these reports do not however adequately define the involvement of GP externus (GPe) versus GP internus (GPi). Furthermore, besides destroying the local neurons, strokes equally damage often extensive fiber projections traversing the involved region.

Per the longstanding classical basal ganglia model (Albin, Young, & Penney, 1989) (DeLong, 1990), reduced DA levels cause DA D2 receptor mediated disinhibition of GABAergic indirect pathway striatal projection neurons, which, in turn, induces excessive inhibition of GPe. In support, neurons show reduced (and abnormally patterned) discharge activity in GPe in primate models of PD (Filion & Tremblay, 1991). Similarly, reduced and abnormally patterned activity is seen in GPe in patients with dystonia undergoing stereotactic surgery (Vitek, et al.,

1999). Consistent with these observations, we found that GP (rodent equivalent to GPe) neurons in jaundiced dystonic rats at rest show marked reductions in discharge rates, with increased irregularity and novel burstiness compared to normal rats (Kumbhare et al., 2015). With movement, multi-unit recordings of GP neurons in normal rats showed similar proportions of autonomous movement related activation or inactivation. In contrast, in dystonic rats, GP neurons showed highly synchronous, near universal *silencing*, preceding and persisting during abnormal dystonic motor activity (Baron M. , Chaniary, Rice, & Shapiro, 2011).

Alexander and colleagues (1986) proposed that the basal ganglia contribute to anatomically segregated motor, associative and limbic cortico-basal ganglia-thalamocortical loop circuits. Hoover and Strick (1993) further elegantly demonstrated the extent of anatomical segregation of basal ganglia-thalamocortical motor and pre-motor sub-circuits. We previously showed that local pharmacological inactivation of specific, discrete hotspots in GPi and the subthalamic nucleus (STN) ameliorated hypokinesia in parkinsonian monkeys (Baron, Wichmann, Ma, & Delong, 2002). In patients undergoing radiofrequency GPi ablation (pallidotomy), anteromedial motor territory lesions were observed to most effectively ameliorate dyskinesia, while central motor territory lesions most effectively improved akinesia (Gross, Lombardi, Lang, Duff, & Hutchison, 1999). In GPe, local injections of the (activating) muscarinic antagonist bicuculline in motor regions induced dyskinesia, in associative regions induced hyperactivity, and in limbic regions induced stereotypical behavior (François, et al., 2004).

From these observations, we postulated that on a markedly slow and highly irregular and bursting neuronal resting state in GPe, cortical drive produces profound regional inhibition of GPe as the basis for dystonia. Because of our present laboratory focus on understanding dystonia, our initial goal here was to determine whether silencing of GP outflow via neurotoxic

ibotenate lesions in rats would induce dystonia. Although prior studies in monkeys failed to demonstrate behavioral effects from reversible pharmacological inhibition (Baron, Wichmann, Ma, & Delong, 2002) or destructive lesioning (Soares, et al., 2004) of GPe, these studies were rather restrictive. If initially successful, we then planned to define the specific dystonia locus in GP via restricted lesions and assess the resultant alterations in neuronal discharge activity in STN and the entopeduncular nucleus (EP, rodent equivalent of GPi). Because the initial large injections variably induced dystonia *and* parkinsonism, we modified subsequent experiments, aiming to separately induce hemidystonia and hemiparkinsonism. If successful, this would implicate a principal role for reduced GPe activity in parkinsonism and dystonia and suggest that these conditions originate from similar physiological disturbances along separate basal ganglia sub-circuits. Additionally, to extend our findings to humans, we compared the anatomical sites in GPi for treating PD versus dystonia via deep brain stimulation (DBS) with that for inducing parkinsonism versus dystonia via GP lesions in rats.

5.2. Methods

Animals. Wistar heterozygous (non-jaundiced) Gunn rats (n = 14, seven males and seven females) and non-carriers (n = 5 females) were used for the animal studies. Animals were obtained from Harlan Sprague Dawley Inc., IN, USA and Charles River, MA, USA and maintained in the Hunter Holmes McGuire Veterans Affairs Medical Center animal facility for at least seven days prior to any procedures. Heterozygous Gunn rats and non-carriers show equivalent baseline behavior and neuronal properties (Kumbhare et al., 2015). Upon affirming that these groups show equivalent post-lesion behavioral and neuronal effects, these data were combined for the present analyses. All experiments were approved and monitored by the Hunter

Holmes McGuire Veterans Affairs Institutional Animal Care and Use Committee (IACUC) and performed in accordance with regulatory guidelines.

Surgery and target localization. The surgical procedures were described in detail previously in Chapter 4.

Prior to lesioning, the posterolateral motor territory of GP was initially mapped typically over 2-3 penetrations using ultrafine 100 µm microelectrodes (Thomas RECORDING GmbH, Giese, Germany) introduced via a Thomas RECORDING Eckhorn microelectrode manipulator. The location and firing patterns of neurons and the borders of encountered nuclei along each microelectrode track were plotted on graph paper. Transparencies generated from sections of the Paxinos and Watson atlas (1982) were superimposed upon these plots to determine the location of the recording tracts. The motor territory of GP was affirmed by identifying neurons whose discharge activity correlated with spontaneous rat movement.

Lesioning. Ibotenic acid (MW: 180.63, Sigma-Aldrich, MO, USA) was dissolved in phosphate buffered saline (0.12-0.15 M) to a pH of 7.4. A quartz glass microinjection pipette (outer diameter: 100 µm; Thomas RECORDING Inc.) was connected via a short tube to a Hamilton syringe (Model #705, 0.05 ml volume and 1.03 mm inner diameter) and the system was filled with the ibotenic acid solution. The syringe pump was set to deliver a volume of 0.4-1.2 µl at rates ranging from 0.08- 0.12 µl/min over an interval of 10 min. After the targeted portion of GP was well defined, the microelectrode was replaced with the pipette and ibotenate (0.12-0.15 M, 0.7-2.1 µl) was injected into GP over 1 to 2 tracks, at 1-2 depths (1-4 sites), at varying laterality (L3.2-4.2) (Table 5.1). The micropipette was left in place for an additional 10 minutes prior to removal. The rat was closely monitored for any signs of distress during the

entire injection session. After removal of the micropipette, the head chamber was sealed using the Teflon cap and the rat was returned to the laboratory observation cage.

Pre- and post-lesion neuronal recording. Baseline neuronal spike activity was initially recorded from GP, EP and STN (Kumbhare et al., 2015). Post-lesion neuronal activity was recorded from STN and EP beginning 4-18 hrs after symptom exhibition. Neuronal and EMG data were recorded during resting and movement epics for 60-120s at a sampling rate of 40-44 kHz and amplified and band pass filtered (gain=50, bandwidth 0.07–8 kHz) via an AlphaLab SnR data acquisition system (Alpha Omega Co. USA Inc., Alpharetta, GA). Neuronal signal processing and pattern analysis were detailed previously (Kumbhare & Baron, 2015) (Kumbhare et al., 2015). Pattern analysis was accomplished utilizing our tri-component classification algorithm to distinguish regular, irregular and bursting neurons.

Behavioral assessments. Between 3-4 hrs after ibotenate injection, the behavior of the animals was formally assessed and separate parkinsonian and dystonia severity clinical scores between 0 and 12 were assigned. Refer to Table 5.2 for behavioral scoring criteria. Also, EMGs recorded at the time of the neuronal recordings and in the home cage were assessed off-line for objective confirmation of dystonia and its severity.

Table 5.1. Clinical ratings in GP lesioned rats

Rat details		Injection sites			Ibotenate		Parkinsonism rating				Dystonia rating			
Effect	Rat #	Lat (mm)	Bregma (mm)	Depth~ (mm)	Molarity (ug/ml)	Volume (ul)	Forelimb flexion	Spontaneous movement	Induced movement	Score	Hindlimb extension	Trunk posture	Falls*	Score
Predominant parkinsonism	11	3.5	-1.6	4.1	0.12	0.7	3	3	3.5	9.5	0	0.5	0	**0.5**
	17	3.4	-1.7	3.9	0.14	0.9	3.5	3	3	9.5	0	0.5	0.5	**1**
	18	3.3	-1.7	4.2	0.14	0.8	4	3	3	10	0	1.5	0	**1.5**
	19*	3.4	-1.6	4.2	0.14	0.8	3	3	3	9	0	0	0	**0**
Predominant dystonia	12*	3.4	-1.5	2.8	0.13	0.8	0.5	0.5	0	**1**	3	3	3	9
	13	3.3	-1.6	2.8	0.14	1.2	1	0	1	**2**	3	3	3	9
	14	3.4	-1.7	3.0	0.13	0.9	2	0	1	**3**	3	3.5	2	8.5
	15	3.4	-1.6	2.8	0.15	0.8	1	0	0	**1**	3	3	3	9
	16	3.4	-1.6	2.9	0.14	0.9	0	1	1	**2**	3	4	4	11
Mixed parkinsonism/ dystonia	1	3.9	-1.6	3.2	0.12	0.4	1.5	3	2	**6.5**	2	2.5	2	6.5
		3.9	-1.6	3.8	0.12	0.4								
	2	3.7	-1.6	3.9	0.12	0.4	2	2.5	2.5	**7**	2.5	3	2	**7.5**
		3.7	-1.6	3.3	0.12	0.4								
	3	4.2	-1.6	4.2	0.12	0.4	0	0.5	0	**0.5**	0	0	0	**0**
		4.2	-1.6	3.4	0.12	0.4								
	4	3.7	-1.6	2.8	0.12	0.5	2	2.5	1	**5.5**	3	3	2.5	**8.5**
		3.5	-1.4	3.8	0.12	0.5								
	5	3.8	-1.6	3.6	0.12	0.6	1	3	3	**7**	1	1	1	**3**
		3.9	-1.5	4.0	0.12	0.6								
	6	3.8	-1.7	3.4	0.12	0.5	3	2	2	**7**	3	2	2	**7**
		3.8	-1.7	4.0	0.12	0.5								
		3.2	-1.7	3.6	0.12	0.5								
		3.2	-1.7	4.0	0.12	0.5								
	7	3.3	-1.6	2.8	0.12	0.7	2	3	2.5	**7.5**	3	3	2	**8**
		3.6	-1.6	3.4	0.12	0.7								
		3.6	-1.6	4.1	0.12	0.7								
	8	3.4	-1.6	3.3	0.12	0.8	2	3	3	**8**	3	3	2	**8**
		3.4	-1.6	4.3	0.12	0.8								
	9*	3.4	-1.5	3.4	0.12	0.8	2	2.5	3	**7.5**	2	2	2.5	**6.5**
		3.4	-1.5	3.9	0.12	0.8								
	10	3.4	-1.6	4.0	0.12	0.5	2	2	3	**7**	2.5	3	2.5	**8**
		3.4	-1.6	3.0	0.12	0.5								

* Indicates rats shown in supplementary video S1; ^Falls induced by dystonia; ~Depth = +10 mm for bregma

Histology. At the completion of the experiments, the rats were euthanized with pentobarbital (0.1 ml, 390 mg/ml i.p.) and immediately perfused via the ascending aorta with 200 ml of saline followed by 200 ml of 10% formalin. After fixation, the brains were frozen, blocked in the parasagittal plane, sliced in 50 µm sections on a cryostat, and alternate sections were silver stained (FD NeuroSilver™ kit II, FD NeuroTechnologies, Inc., Columbia, MD, USA).

Table 5.2. Parkinsonian and dystonia rating

Motor Disorder	Feature	Scores (total range: 0-12 each for parkinsonism and dystonia)
Parkinsonism	Forelimb/paw flexion posturing	0: none 1: rare forelimb/paw posturing; places paw when ambulates 2: occasional posturing; limited placement of paw 3. frequent posturing; without placement of paw 4: fixed posturing
	Spontaneous movement	0: Normal behavior, ambulation, sniffing, grooming. 1: mildly slower or reduced general activity 2: moderately reduced activity 3: severely reduced activity 4: near complete absence of spontaneous activity
	Activity response to mild audio or tactile stimuli	0: responds normally 1: mildly reduced overall response 2: moderately reduced response 3: severely limited response 4: no response
Dystonia	Hindlimb extension	0: never 1: rare and mild extension of hindlimb 2: common and moderate extension 3. frequent and prominent extension 4: fixed extension
	Truncal posturing	0: perfectly upright normal posture 1: slight and infrequent abnormal truncal posture 2: mild to moderate and frequent truncal flexion 3: moderately prominent truncal flexion and twisting 4: marked, fixed truncal flexion and twisting.
	Falling in response to impaired ambulation due to hindlimb spread and twisting of trunk	0: none 1: rare associated falls 2: occasional associated falls 3: frequent associated falls 4: fixed dystonia (no falls, but without attempts at ambulation)

Reconstruction of lesion volume. Using a light microscope (Nikon Eclipse E400), the silver stained sections were examined for confirmation of the location of the microelectrode tracks and definition of the ibotenic lesions. Individual lesions were reconstructed based on the location of silver stained cells and secondary inflammatory damage (Fig. 5.1*A*-*A”*). The defined lesions were then drawn on corresponding sagittal atlas sections (Fig. 5.1*B*-*B”*). The lesion coordinates were registered, interpolated, and reconstructed in a 3D region of interest, which includes GP

and surrounding regions (Fig. 5.1*C-C"*).

Development of lesion-effect probability model. A novel score-based spatial modeling algorithm was developed to define the distribution of efficacious lesions in the region of interest (ROI) for induction of parkinsonism and dystonia. The ROI was limited to the explored GP lesioned area in the 19 study rats. The following algorithm was applied separately for parkinsonism and dystonia symptom score sets:

1. The entire ROI was selected to encompass the lateral half (approximated motor region) of GP and the extent of lesion spread within GP, corresponding to lateral 2.1 - 4.8 mm, posterior 0.2 - 2.4 mm, and depth 1.8 – 6 mm. The approximated motor territory was based on extensive prior and current recordings and assessments for correlations between neuronal activity and active animal movement. The ROI was in turn modeled by a $28 \times 23 \times 43$ point grid system divided it into 27692 voxels, each of dimensions $0.1 \times 0.1 \times 0.1\ \mathrm{mm}^3$.
2. For each lesioned rat, parkinsonism and dystonia scale scores were separately assigned to each voxel that lies within the volume of lesion spread. Therefore, each voxel was assigned 19 different scores, equal to the number of lesioned animals. A NaN (not a number) score was assigned to any voxel outside of the lesion.
3. For each voxel, mean and standard deviation (SD) of the assigned scores was calculated. Voxels deemed sparsely sampled (< 3 non-NaN values) or with coefficient of variation (CV) > 1 were assigned NaN values, thereby excluding these data from further analysis (Fig. 5.2*A-A"*, *B-B"*)).
4. Next, *Global Moran's I function (GMI*) (Moran, 1950) (Ferstl, 2007), modified for 3d data, was used on the voxelated data to assess spatial autocorrelation. GMI classifies the

overall spatial distribution as clustered (GMI ~+1), dispersed (GMI ~-1) or random (GMI ≃ 0).

5. Next, *Getis-Ord GI* statistic* (Getis & Ord, 1992) (Ferstl, 2007) (Mitchell, 2005), modified for 3D data, was calculated providing a statistical hot-spot analysis using the local pattern of spatial association to identify local spatial clusters with high or low efficacy values in the ROI (Fig. 5.2*B-B”*,*C-C”*). For a statistically significant positive Z-values (GI*; z-score > 1.96 ($p < 0.05$)), the larger the Z-values, the more intense the clustering of hot spots.
6. The efficacy distribution maps (generated in steps 1-3) were subsequently filtered to include only significant z-scores (GI*) and generate final maps revealing the statistically significant hot spots (Fig. 5.2*E-E”*,*F-F”* and Fig. 5.3*A*).
7. Lastly, to assess the strength of the relationship between the location of the lesions and the severity of the induced motor behavior, parkinsonian and dystonia clinical scores for each rat were correlated with the degree of overlap of the corresponding hot spot (Fig. 5.3*B*,*B”*).

DBS surgery and post-operative programming optimization. Nine patients with dystonia (6 males, 3 females; 3 DYT1, 3 generalized idiopathic, 1 task-specific, and 2 torticollis) and 12 successive patients with PD (all males) who had undergone GPi DBS surgery at the Virginia Commonwealth University Medical Center or at the Hunter Holmes McGuire Veterans Affairs Medical Center in Richmond, VA were included in this study. Using microelectrode and intra-operative CT guidance (Vega, Holloway, & Larson, 2014), DBS electrodes (Medtronic Inc., Fridley, MN, USA) were implanted bilaterally or unilaterally (PD: n = 9 bilateral, 3 unilateral; dystonia: 7 bilateral, 2 unilateral). Preoperatively, stereotactic computerized tomogram (CT) and

a magnetic resonance image (MRI) were obtained with volumetric flair, FGATIR, and volumetric T1 with and without contrast sequences. The default targeting coordinates of 21 mm lateral, 2 mm anterior to and 4 mm deep to the midpoint of the anterior-posterior commissure plane were modified based on direct visualization of the GPi as seen on the FGATIR and flair sequences. The entry point was chosen to maximize targeting of a first microelectrode through as much of the motor GPi as possible, while avoiding sulci, vessels, and the ventricles. A second track was chosen for simultaneous passage of a second microelectrode 2 mm posterior or posterior-lateral from the first.

The surgical procedure was carried out with frameless stereotaxy utilizing the Medtronic Nexframe system and intraoperative O-arm image guidance (Kelman, Ramakrishnan, Davies, & Holloway, 2010). After making a burr hole, simultaneous recording along the 2 microelectrode tracks was carried out to assess the GPi boundaries and presence of motor responsive cells. The recording findings were marked on graph paper and compared with parasagittal Schaltenbrand and Wahren (S-W) transparency maps. An O-arm image was then obtained to image the microelectrodes and the image was merged with the pre-op CT and MRI images to determine the actual MER trajectories. At this time, the microelectrodes were withdrawn within its cannula and test macro-stimulation was conducted with the macrostimulation collars of the micro-cannulas. Finally, the MER data, clinical responses to the macro-stimulation, and the imaged locations of the trajectories were reviewed and the optimal track was identified.

Standard DBS 3389 and 3387 model leads (Medtronic Inc.) were inserted. Both model leads have four 0.5 x 1.5 mm contacts, with the contacts separated by either 0.5 mm (3389 model) or 1.5 mm (3387 model). Post-operatively, the programming nurse and physician used the Medtronic N'Vision clinician programmer to optimize the DBS stimulation parameters over

multiple sessions. This is done by assessing the effect of stimulation with each of the 4 electrode contacts using the various potential monopolar and bipolar (distal contact negative and the adjacent more proximal contact positive) settings, as well as optimizing the pulse width and frequency.

Reconstruction of optimized GPi DBS territories for PD vs dystonia. The location of the tip of the implanted DBS electrodes was determined using Medtronic's StealthMerge and Stealth3D visualization software by fusing a post-operative CT with a merged pre-operative CT and MRI. The coordinates of the post-operatively optimized electrode stimulation contact(s) were determined retrospectively from the location of the tip of the electrodes, the sagittal and coronal angles of the trajectory, and the geometry of the (shorter vs longer) stimulating electrode surfaces. For monopolar stimulation, the stimulation coordinate was determined by the center of the stimulating contact and for bipolar stimulation, by the geometric center of the two adjacent stimulation contacts. Delaunay triangulations were computed each for the Parkinson disease and dystonia DBS contact data sets.

Statistics. Statistical analyses were performed in MATLAB R2012. Indifference in neuronal discharge features between groups showing similar features were assessed with two one-sided tests (TOSTs) for equivalence (Schuirmann, 1987) (Wellek, 2010). The mean values were considered to be significantly equivalent (α=0.05) if the 90% confidence interval was within the defined zone of indifference (±5 spikes/s for discharge rates and ± 0.2 for the tri-components). One and two sample T-tests were used to compare population percentages within same and different groups. Two-way chi-square test was used to compare neuronal counts in different neuronal populations. Independent two-sample t-Test were used to assess for group differences in mean discharge rates, pattern discriminatory measures, and burst parameters.

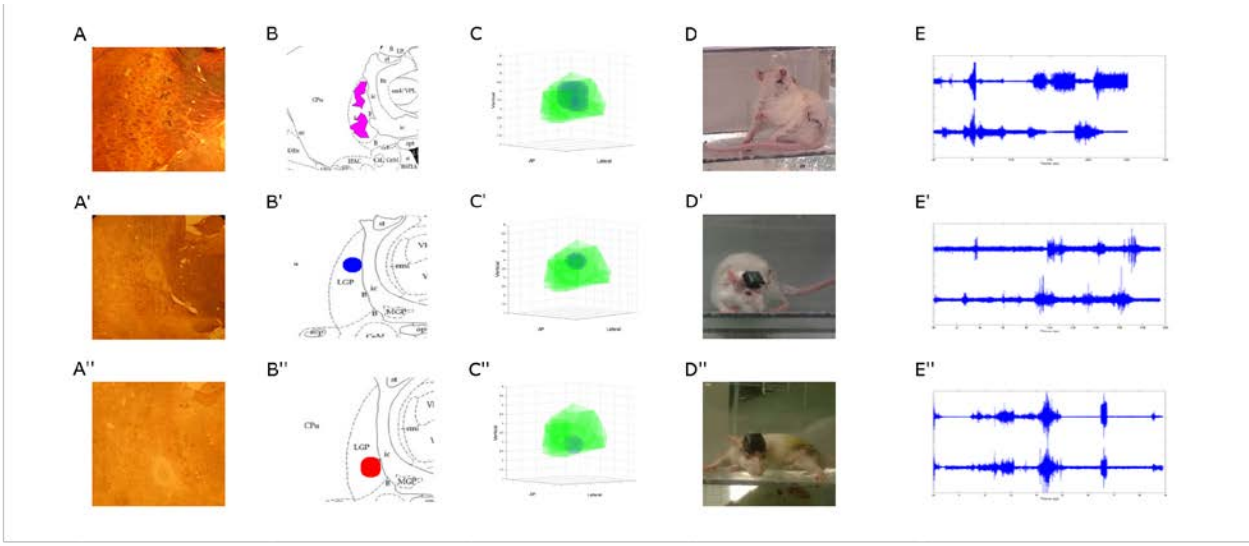

Figure 5.1. Ventral lesions in GP produce dystonia and dorsal lesions produce parkinsonism. ***A-A"***, Silver stained sagittal sections from ***A*** a rat (#6) with multi-site dorsal and ventral ibotenate GP lesions, ***A'*** a rat (#19) with an isolated dorsal lesion, and ***A"*** a rat (#15) with a ventral lesion. ***B-B"***, Corresponding lesions in **A-A"** superimposed on rat brain atlas sections (Paxinos & Watson, 1982). ***C-C"***, 3D figure of GP created from atlas sections depicting the full extent of the lesions. ***D-D"***, Photographs of resultant ***D*** mixed parkinsonism and dystonia from the combined lesions shown in ***A. D'***, predominant parkinsonism from the dorsal lesion shown in ***A'*** and ***D"***, predominant dystonia from the ventral lesion shown in ***A"***. The rats with dystonia in ***D*** and ***D"*** can be seen to display characteristic extension and spreading of the hindlimb, while the rats with parkinsonism (***D*** and ***D'***) show characteristic forelimb flexion posturing and fist clenching. ***E-E"***, Corresponding EMG recordings from antagonistic hip muscles, gluteus medius and gluteus superficialis show ***E'***, normal alternating agonist-antagonist contractions in the rat with predominate parkinsonism, ***E"***, characteristic dystonic co-contractions during movement in the rat with predominant dystonia, and ***E*** a mixed EMG pattern in the rat with parkinsonism and dystonia.

5.3. Results

Dystonia and parkinsonism induced by neuronal toxic lesions in GP

Between 30-60 min after the drug injections, all animals exhibited contralateral rotation and 18 of 19 rats developed dystonia and/or parkinsonism, with the clinical features reaching maximum intensity within 4 hrs. Refer to Table 5.1 for details of the individual injections and resultant clinical effects. To initially maximize the possibility of inducing behavioral effects, relatively large lesions (0.12 M, 0.8-2.1 µl over 2-4 sites) were made in the first 10 rats. Nine of these 10 rats developed mild to severe contralateral dystonia *and* parkinsonism (Fig. 5.1*A-D* and Movie). A single animal (#3), with the most laterally placed lesion (at L4.2), developed a relatively mild

rotation bias without additional overt behavioral features. By rat #8, it became evident that the severity of parkinsonism and dystonia correlated with more medial placement of the lesions within the motor territory. In response, all subsequent lesions were targeted to this region. In the last 9 rats (#11-19), single dorsal (n = 4) or ventral (n = 5) lesions (0.12-0.15 M, 0.7-1.2 µl) were made. Predominant prominent parkinsonism was consistently induced by the circumscribed dorsal lesions (Fig. 5.1*A'-D'*) and prominent dystonia by the ventral lesions (Fig. 5.1*A"-D"*).

Apart from predominant unilateral involvement, dystonia in GP lesioned (dyst-L) rats appeared identical to that in jaundiced Gunn rats (Chaniary et al., 2009). In both groups, with the head restrained, dystonia was not evident during periods of motor inactivity for up to 5-10 min. While unrestrained, dystonia was consistently evident during self-initiated movement in the hindlimb and to a lesser degree in the forelimb (Movie). In more severe animals, the affected hindlimb would often fully extend during contralateral rotation and frequently cause the animal to fall. All parkinsonian lesioned (park-L) rats showed prominent flexion posturing of the affected forelimb with mild to moderately reduced overall movement. The paw was held clenched with a paucity of movement of the forelimb. In contrast, the hindlimb was only more mildly affected.

Park-L rats consistently showed a normal pattern of alternating contractions of antagonistic hip muscle pairs during movement (Fig. 5.1*E'*). In contrast, dyst-L rats and to an extent mixed parkinsonian/dystonia rats showed characteristic dystonic co-activations of antagonistic muscle pairs (Fig. 5.1*E,E"*). In further objective support of parkinsonism and dystonia, respectively, neuronal activity in EP and STN in park-L and dyst-L rats demonstrated characteristic neurophysiological findings of these conditions (described below).

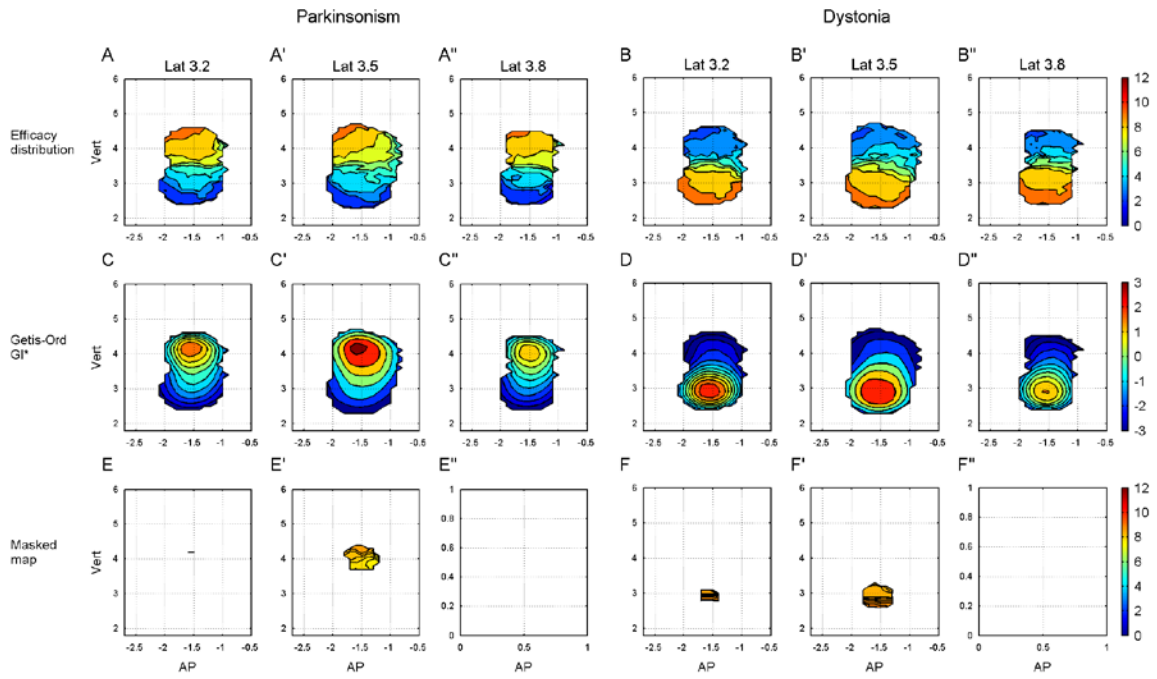

Figure 5.2. Parkinsonism and dystonia are induced by lesions in circumscribed, non-overlapping regions of GP. ***A,B***, 2D efficacy distributions for inducing parkinsonism ***A-A"*** and dystonia ***B-B"*** via GP lesions, plotted on three representative sagittal planes (L3.2, L3.5 and L3.8). The color bars indicate the color coded efficacy values. ***C,D***, Getis-Ord GI* statistics maps illustrate the z score values (color bar) for the efficacy distribution plots. ***E,F***, Masked maps created by thresholding the efficacy maps (z score threshold cut-off > 1.96) indicate the statistically significant hotspots for inducing parkinsonism ***E-E"*** and dystonia ***F-F"*** via GP lesions.

Hotspot delineation for inducing parkinsonism and dystonia with GP lesions

2-D efficacy distribution maps demonstrated the high efficacy dorsal region for inducing parkinsonism and ventral region for inducing dystonia within the medial portion of the (posterolateral) motor territory of GP (Fig. 5.2*A-A"*,*B-B"*). High global Moran's I function values for the parkinsonism (0.821) and dystonia (0.886) efficacy maps indicated strong spatial autocorrelations, both $p < 0.05$ (i.e., with less than a 5% probability that the distinct clusters resulted randomly). Getis-Ord Gi* statistics (Z scores) for the distribution maps revealed

progressively more strongly associated regions for selectively inducing parkinsonism and dystonia via GP lesions (Fig. 5.2*C-C”*,*D-D”*). Masked distribution maps demonstrated the two statistically significant high efficacy hotspots to be non-overlapping and to occupy closely similar anteroposterior and mediolateral regions (Fig. 5.2E-E”,F-F”). The hot spot for parkinsonism was centered at L3.59, P1.62, D4.04 and that for dystonia at L3.55, P1.64, D2.92 (for reference, D = 10 mm for bregma; GP is centered at approx. L3.3, P1.7, D3.4). Finally, after masking out insignificant and low efficacy spots, the final 3D model demonstrated 100% anatomical segregation of the parkinsonian and dystonia hotspots (Fig. 5.3*A*). For each lesion, the resultant clinical severity scores were highly correlated with the extent of overlap of the hotspots for both parkinsonism ($r = 0.899$, $p < 0.005$; Fig. 5.3*B* and dystonia ($r = 0.924$, $p < 0.005$); Fig. 5.3*B’*), affirming a strong relationship between the induced movement features and the specific regional involvement of GP.

Baseline neuronal properties in dorsal versus ventral motor regions of GP

We reasoned that regional differences in baseline neuronal discharge properties in GP could potentially contribute to the different behavioral features induced by dorsal versus ventral motor territory lesions. We thus compared the discharge properties of neurons (n = 58) encountered at variable depths within the motor territory of GP in normal rats (n = 12). These analyses revealed no relation between the discharge rates ($r = -0.130$, $p = 0.33$) or patterns ($r = 0.039$, $p = 0.76$) and the recording depth (Fig. 5.3*C,C’*). This suggested that the clinical differences between parkinsonism and dystonia are not attributable to the removal of physiologically different signals at the level of GP.

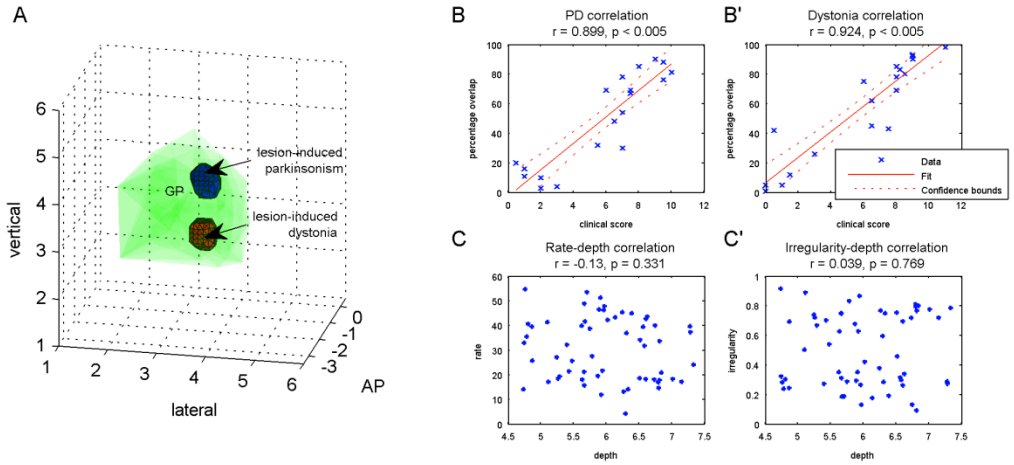

Figure 5.3. Parkinsonism and dystonia are produced by silencing of identically characterized neurons in GP along distinct motor sub-circuits. ***A***, 3D figure illustrating the distinct hotspots for inducing parkinsonism (blue) and dystonia (red) via ibotenate lesions in GP. ***B,B'***, Correlation between the extent of overlap of the hotspot for individual lesions (n = 19) and the severity of induced parkinsonian ***B*** and dystonic ***B'*** features. The linear regression and the confidence intervals (CI) are shown. ***C,C'***, Correlation between the discharge rates ***C*** and irregularity properties ***C'*** of neurons in GP (n = 58 neurons) and the depth of the corresponding recordings in GP in normal rats

Neuronal discharge properties in EP and STN in dyst-L and park-L rats

We next considered that if GP silencing plays a principle role in various dystonias, then the resultant 'downstream' alterations in STN and EP in dyst-L rats should closely resemble those in other experimental dystonia models, including kernicterus. Towards this aim, 26 neurons were recorded in the motor territories of EP (n = 16) and STN (n = 10) in 4 dyst-L rats *at rest*. Previously reported neuronal recordings collected under the same conditions in normal and dystonic kernicterus rats (dyst-K) (Kumbhare et al., 2015) were used for comparison. The induction, clinical, and EMG features of the jaundiced dystonia model were described in detail previously (Chaniary et al., 2008) (Chaniary et al., 2009) (Shaia, et al., 2002). In normal rats

(Fig. 5.4*A*), the neuronal populations in GP, STN and EP are similarly characterized by regular tonic (range across the three nuclei: 52-56%) and slower irregular populations (42-46%), without notable bursty neurons (<1%). In dyst-K rats, discharge rates in GP, STN and EP are appreciably slower (Fig. 5.4*B*), and while a dichotomous distribution is maintained (Fig. 5.4*A*), the patterns are highly irregular (52-57%) or bursty (41-46%).

Similar to dyst-K rats, average resting discharge rates were appreciably reduced in EP (51%, $p < 0.001$) and STN (37%, $p = 0.002$) in dyst-L rats vs controls (Fig. 5.4*B*). As for dyst-K rats, neurons were distributed between highly irregular and bursty populations (irregular vs bursty: EP, 56% vs 37%; STN, 51% vs 42%; Fig. 5.4*A*). Also similarly, neuronal irregularity was moderately increased and burstiness markedly increased in STN and EP in dyst-L compared to normal rats (all $p < 0.001$; Fig. 5.4*C*,*D*). None of the principal neuronal properties, including discharge rates, irregularity, and burstiness, differed in STN and EP between dyst-K and dyst-L rats (two one-sided tests for equivalence TOST, all $p < 0.05$). The findings of equivalent neuronal properties in EP and STN in dyst-L and dyst-K rats thus strengthen our clinical and EMG impressions of dystonia and support a common pathological role for GP silencing in various forms of dystonia.

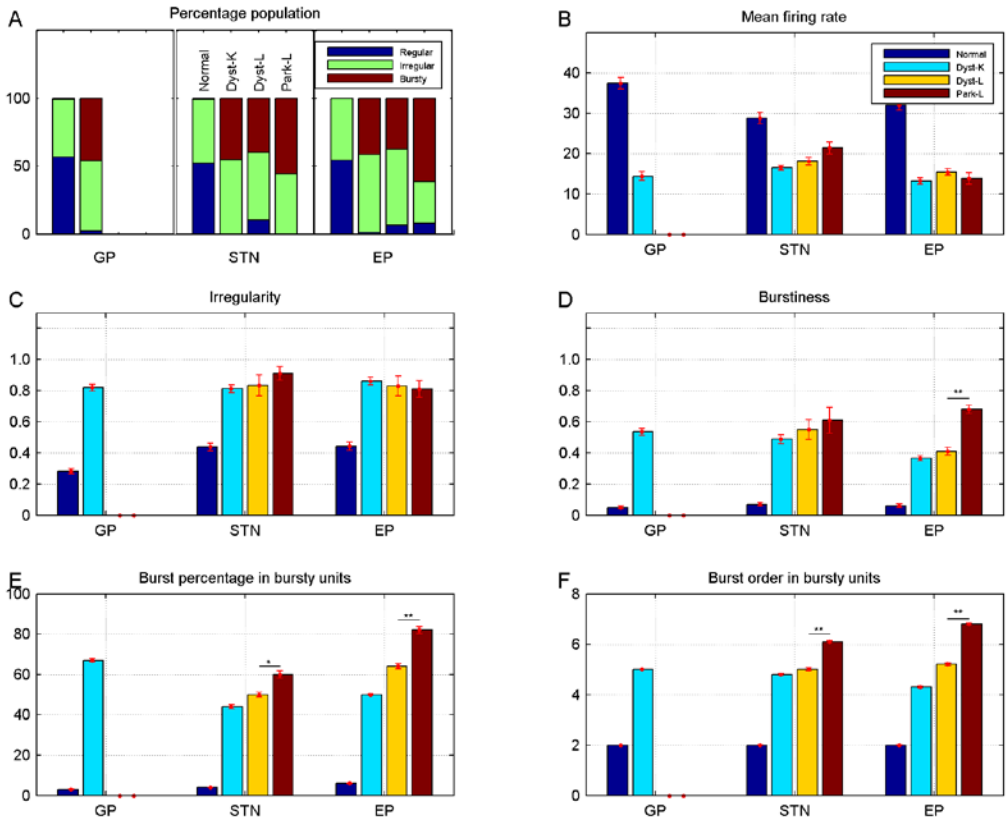

Figure 5.4. Neuronal properties in STN and EP are nearly identical between dyst-L and dyst-K rats, while neuronal properties are distinguished in park-L rats by oscillatory burst activity in EP. Neuronal recordings in GP in normal and dyst-K rats and recordings in STN, and EP in normal, dyst-K, dyst-L, and park-L rats, illustrating: ***A***, percentages of regular, irregular, and bursty populations, ***B,*** mean firing rates, ***C***, irregularity, ***D***, burstiness, **E**, burst percentages (percentage of burst discharges/ total discharges) for bursty neurons and ***F***, burst order (average number of discharges per burst) for bursty neurons. *$p < 0.05$, **$p < 0.001$. The error bars indicate SEM.

Although baseline discharge properties were similar throughout the motor territory of GP, we were interested in establishing whether dorsal and ventral lesions produced different effects on 'downstream" neurons in STN and EP, as predicted from recording studies in humans with PD and dystonia. Towards this aim, 22 neurons were recorded in EP (n = 13) and STN (n = 9) in 3 park-L rats at rest and compared to the recordings collected in dyst-L rats. Similar to dyst-L rats, mean discharge rates in park-L rats were highly reduced in EP (56%, $p < 0.001$) and STN (25%, $p < 0.05$) vs controls (Fig. 5.4*B*). Compared to dyst-L rats, park-L rats showed similar neuronal

populations, except for a higher percentage of bursty neurons in EP (bursty = 64%, irregular = 27%, regular = 9%; Fig. 5.4*A*), though this did not reach significance ($p = 0.209$). As for dyst-L rats, neuronal irregularity was highly increased and burstiness dramatically increased in STN and EP in park-L compared to normal rats (all $p < 0.001$; Fig. 5.4*C,D*). Except for a trend ($p = 0.072$) towards faster discharge rates in STN in park-L vs dyst-L rats (21.4 $\pm$ 4.5 vs 18.1 $\pm$ 2.9), no significant differences in discharge rates (EP: $p = 0.323$) or irregularity (EP: $p = 0.798$, STN: $p = 0.371$) were evident between park-L and dyst-L rats. Burstiness (reflective of the proportion of burst neurons, burst percentages (BP) and burst tendencies (Kumbhare & Baron, 2015)) was moderately greater among EP ($p < 0.001$), but not STN neurons ($p = 0.569$) in park-L compared to dyst-L rats (Fig. 5.4*D*). Burst neurons in EP in park-L rats exhibited a particular high mean BP (82% vs 48% in dyst-L; difference, $p < 0.001$; Fig. 5.4*E*), indicating a tendency to fire in a relatively pure burst mode. Burst neurons in STN also showed a significant ($p < 0.05$), though comparatively small increase in overall BP in park-L (60%) vs dyst-L rats (51%). Moreover, exclusively in EP in park-L rats, 42% of the burst trains were oscillatory (freq. range = 0.5-7 Hz; representative neuron in Fig. 5.5*A-D*). Additionally, the average burst order (discharges/ burst) of burst neurons in EP and STN were greater in park-L than dyst-L rats (EP: 6.5 vs 5.2, STN: 6.0 vs 5.1, each $p < 0.001$; Fig. 5.4*F*). The neuronal features in park-L rats are consistent with those in humans with PD and therefore support our impression of parkinsonism in these animals.

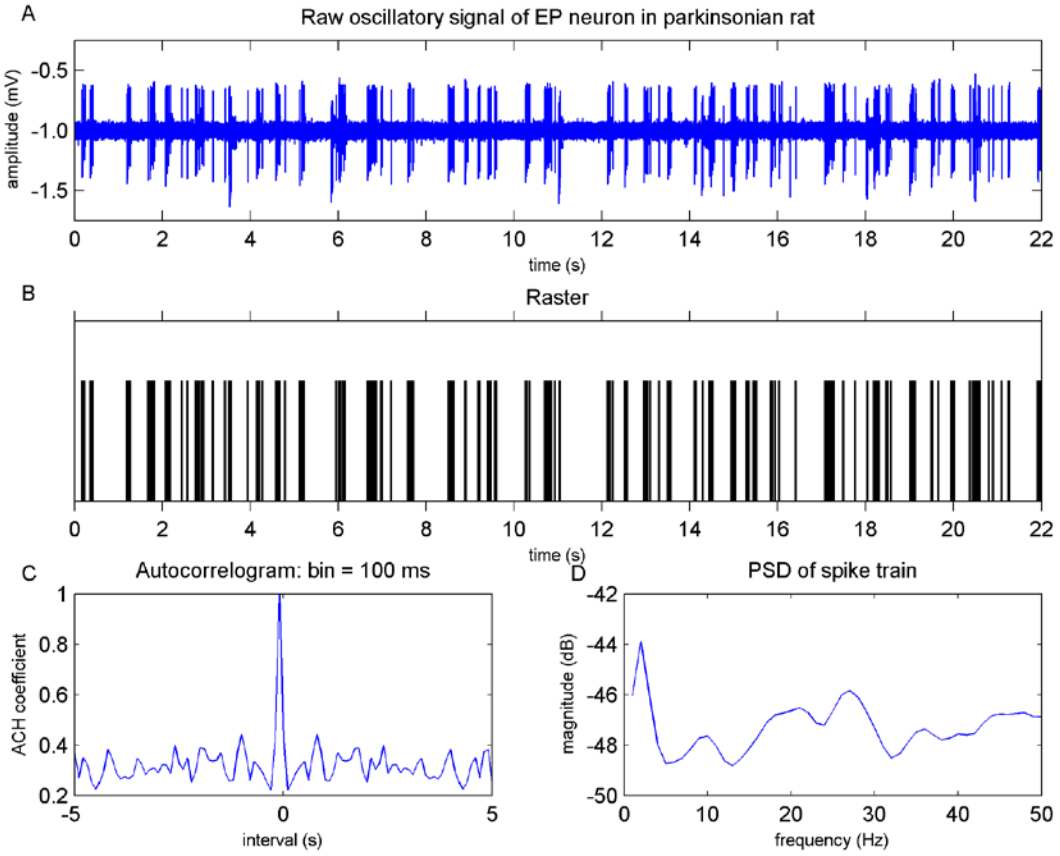

Figure 5.5. Example of an oscillatory neuron in EP in a park-L rat. ***A***, 22 sec segment of a raw EP signal, ***B***, corresponding spike raster, ***C***, autocorrelation histogram (ACH) of the spike train, and ***D***, power spectral density (PSD) of the spike train.

GPi DBS efficacy sites in PD versus dystonia patients

Comparing the location of the DBS contacts utilized to treat 12 subjects with PD and 9 subjects with dystonia revealed the efficacious region for PD to be located relatively dorsal to that for treating dystonia (Fig 5.6). The density of stimulation across subjects for treating PD was centered at L21.5, A5.1, D2.0, while that for dystonia was centered at L21.4, A3.6, D-0.05. The relative DBS efficacy distributions for PD and dystonia are thus anatomically consistent with the dorsal-ventral distributions for inducing parkinsonism and dystonia via GPe lesions in rodents.

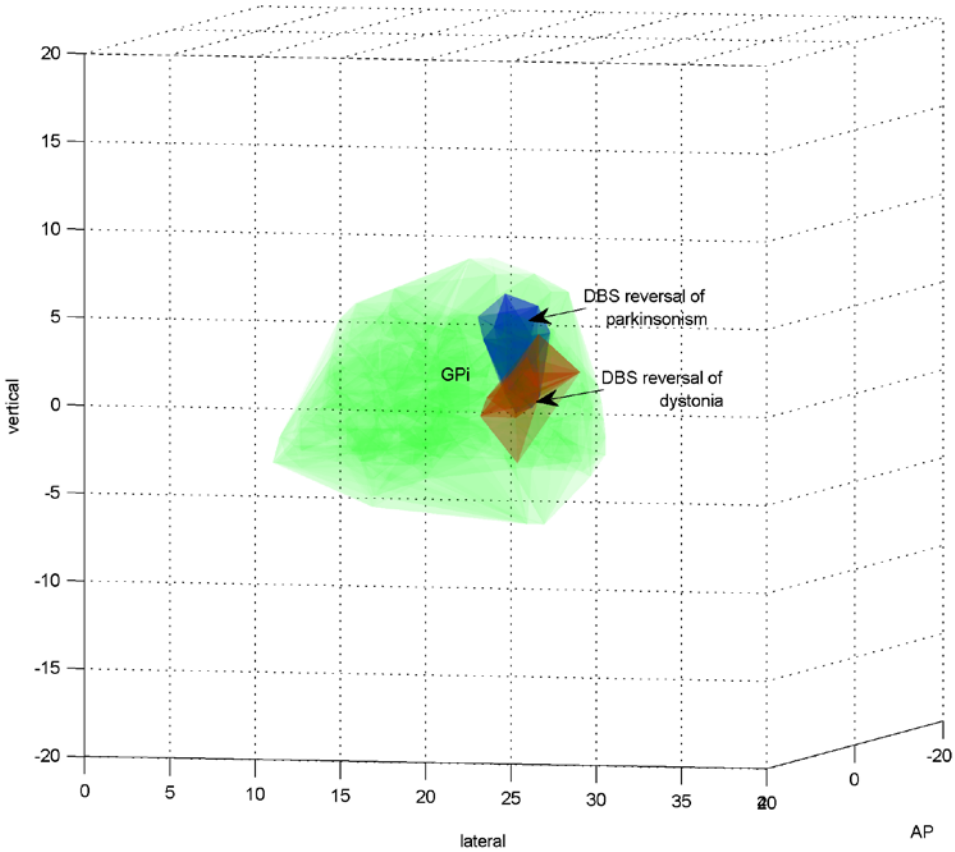

Figure 5.6. GPi DBS efficacy distributions for patients with PD versus dystonia. GPi DBS efficacy density regions for 12 subjects with PD (blue) versus 9 subjects with dystonia (red). The GPi representation (green) was created from multi-dimensional Schaltenbrand and Warran atlas sections (Schaltenbrand & Wahren, 1977).

5.4. Discussion

Results from this chapter showed that parkinsonism and dystonia can be induced via neuronal toxic lesions in GP, thereby demonstrating that silencing of GP neuronal signaling is sufficient to induce both of these common clinical conditions. Moreover, we demonstrated that these two movement features can be independently induced by pinpointed lesions in distinct sites within the motor territory of GP. Additionally, we found the *in vivo* baseline properties of neurons in

these two functionally distinct territories to be indistinguishable. Therefore, these disparate clinical conditions appear to originate from similar physiological disturbances along anatomically distinct basal ganglia motor sub-circuits.

Ultimately, however, major differences in neuronal properties result at the output level of the basal ganglia (EP/GPi) in these two conditions and almost certainly contribute to the dissimilar motor features.

As developed in the introduction, numerous previous clinical and experimental observations predicted that abolishing GP output should induce dystonia, as well as parkinsonism. However, most compelling to us, and leading to the present investigations, was our prior discovery in jaundiced dystonic rats of widespread neuronal silencing in GP preceding and persisting with dystonic motor activity. Thus, whether produced by excessive extrinsic inhibition via the putamen (Perlmutter, et al., 1997) (Black, et al., 2014) or by destruction of GP neurons, as demonstrated here, loss of GPe neuronal signaling appears to be a principal cause of dystonia. By showing largely indistinguishable clinical features and neuronal properties in EP and STN in GP lesioned and kernicterus rats, this supports a similar pathological role for GP silencing in various secondary forms of dystonia. However, in light of the large disparity between the responses to GPi pallidotomy and DBS in primary versus secondary dystonia (Holloway, Baron, Brown, Cifu, & Ramesh, 2006) (Eltahawy, Saint-Cyr, Giladi, Lang, & Lozano, 2005), major pathophysiological differences must exist between primary and secondary dystonias.

Delong and Georgopolous (1981) initially proposed that the basal ganglia contributes to segregated ‘sensorimotor’ and ‘association’ cortical-basal ganglia-thalamocortical circuits. The motor circuit of the basal ganglia has since been considered to encompass multiple anatomically distinct sub-circuits (Schell & Strick, 1984) (Hoover & Strick, 1993). Previous observations in

humans undergoing GPi pallidotomy and DBS suggested that these motor sub-circuits differentially contribute to various movement disorder features. For example, in PD subjects, lesions in the dorsal motor territory of GPi were observed to most effectively benefit akinesia (Krack, et al., 1998), while ventral lesions or DBS stimulation most effectively ameliorated levodopa-induced dyskinesia (Krack, et al., 1998) (Kisore, Panikar, Balakrishnan, Joseph, & Sarma, 2000). In patients with primary dystonia, DBS stimulation in the ventral motor territory of GPi was reported to most effectively improve dystonia (Houeto, et al., 2007) (Tisch, et al., 2007). Presently, we retrospectively compared the sites of efficacious DBS stimulation among groups of our patients with PD and dystonia. Consistent with prior single group observations, we found that stimulation of more dorsal DBS contacts most effectively ameliorated symptoms of PD, while relatively more ventral contracts were more efficacious for treating dystonia. The differential dorsal-ventral distributions for treating PD versus dystonia with GPi stimulation or lesions are consistent with the dorsal-ventral distribution we found for inducing parkinsonism and dystonia via GP lesions. These combined observations support our contention that excessive silencing of GPe along specific dorsal and ventral basal ganglia motor sub-circuits differentially disinhibits GPi to produce parkinsonism and dystonia, respectively, which, in turn, can be ameliorated by reducing pathological GPi discharge signaling via GPi pallidotomy or DBS targeting the specifically pathologically involved sub-circuit.

Using transsynaptic viral labeling techniques, Hoover and Strick (1993) injected arm regions of the supplementary motor area (SMA), primary motor cortex (MC) and premotor cortex in primates and, demonstrated retrograde labeling, via the thalamus, of neurons in non-overlapping regions of GPi. Using similar techniques, Saga et al (2011) injected separate dorsal and ventral regions of the premotor cortex and labeled neurons in non-overlapping regions of GPi. Both of

these studies also showed that GPi-thalamocortical projections to specific motor-related regions of the cortex originate from mirror regions in the internal and external portions of GPi (divided by the accessory lamina). Thus, while it is tempting to conclude here that parkinsonism originates from one specific motor sub-circuit and dystonia another, it is also conceivable that these conditions might originate along mirror parallel circuits located in outer and inner portions of GPi, respectively. Using diffuse tensor imaging, Rozanski et al. (2014) mapped the effective ventral GPi DBS stimulation contacts for treating dystonia to MC and SMA and the dorsal ineffective contacts to pre-SMA and premotor cortex. While these findings require replication, such novel techniques could allow us to accurately define in humans the responsible sub-circuits for dystonia and PD. Another consideration however is that extensive arborizing of pallidal dendritic trees, for example, may permit considerable communication across the various basal ganglia subcircuits (Percheron & Filion, 1991) (Haber, 2003). Along these lines, even though we induced parkinsonism and dystonia via restricted lesions in GP, only a small portion of neurons in EP and STN retained normal appearing neuronal activity.

The finding here of prominent oscillatory bursting exclusively in EP in parkinsonian but not dystonic rats is consistent with findings of tremor-related oscillatory activity in GPi in patients undergoing DBS surgery (Hutchison, Lozano, Tasker, Lang, & Dostrovsky, 1997). Although the 0.5-7 hz frequency of the burst oscillations overlaps that of typical 3-7 Hz rest tremor in PD, park-L rats do not exhibit tremor. It can be suggested that in dystonia, extensive, unabated activation of GPi-thalamocortical signals leads to uncontrolled co-activation of antagonist muscles and spread to unintended muscles. In contrast, in PD, burst and irregular discharge activity at the output level of the basal ganglia may act to disrupt normal thalamocortical signaling and in turn, produce such features as bradykinesia and akinesia. On the other hand,

burst oscillatory activity may drive motor activity and produce tremor. The present novel GP lesioned parkinsonian and dystonia models provide potentially valuable experimental models to further work out the precise pathological mechanisms contributing to these movement disorders.

In summary, we have shown that silencing of GP neurons in isolation is sufficient to both induce parkinsonism and dystonia. Further, our findings indicate that these two movement conditions originate along separate basal ganglia motor pathways and involve different pathophysiological features at the output of the basal ganglia. Additional studies are needed to define the specific motor sub-pathways involved in producing these conditions and to establish more specifically how the distinct neurophysiological abnormalities at the level of GPi differentially contribute to each of these conditions. Also, further studies are needed to define the mechanistic differences between primary and secondary forms of dystonia and parkinsonism to account for why pallidotomy and GPi DBS, with exceptions, only appreciably benefit primary forms of these disorders. The selective induction of hemi-parkinsonism via dorsal motor territory lesions and hemi-dystonia by ventral lesions in GP provide new focused animal models, which can provide the means to further address these and other many remaining uncertainties about normal and pathological basal ganglia functioning.

Movie . Behavioral responses to GP lesions in rats. ***0-20 sec***: Normal control rat behavior. ***20-40 sec***: mixed parkinsonism and dystonia following combined dorsal and ventral motor territory lesions. Note the parkinsonian forelimb paw flexion and dystonic hindlimb extension on the affected side. ***41-58 sec***: parkinsonism after a dorsal GP lesion. Note the forelimb paw flexion and reduced generalized activity. ***60-75 sec***: dystonia after a ventral GP lesion. Note the hindlimb extension and truncal posture.

CHAPTER 6

PERSISTENTLY ABNORMAL NEURONAL DISCHARGE ACTIVITY IN THE BASAL GANGLIA AND THALAMUS IN SPONTANEOUSLY RECOVERED DYSTONIC RATS

6.1 INTRODUCTION

It was previously reported that neuronal discharge activity in the globus pallidus (GP), subthalamic nucleus (STN), and entopeduncular nucleus (EP) in dystonic Gunn rats is characterized by 1) highly irregular or 2) slow, burst activity, in distinction from 1) regular tonic or 2) irregular discharge in normal rats. Further, abnormally synchronized movement related pauses across neurons in GP and synchronized bursts in EP correlated with EMG recorded co-contractions. Presently, neuronal activity in animals who had spontaneously recovered from after developing prominent dystonia was examined. We hypothesized that the neuronal activity in the basal ganglia-thalamocortical circuit would be largely normalized in recovered, previously dystonic animals. The recent findings of persistently abnormal pallidothalamic discharge activity in rats who had spontaneously recovered from dystonia were surprising [6]. Additional investigation would help to recognize any critical discharging feature in the network which regardless of abnormal activity in other components relays compensatory normal signals to the muscles. We further, hypothesize that, restoration of normal motor functions in these animals is due to downstream recovery of normal information processing at some point in BG-thalamo-cortical network indicating a potential bypass/ compensation (to some extent) of the abnormal pallidothalamic activity.

6.2. METHODS

Homozygous recessive jaundiced (jj) Gunn rats lack uridine diphosphate glucuronosyl transferase and cannot effectively conjugate and excrete bilirubin. The pups are mildly jaundiced at birth, but remain motorically normally. At 16 days of age, at the peak of bilribubin levels, jj and non-jaundiced (Nj) rats were injected (i.p) with sulfadimethoxine and saline, respectively. Sulfadimethoxine displaces bilirubin from serum albumin into the brain and in turn, induces dystonia. Behavioral activity, including dystonia, was accessed using a custom grid lined Plexiglas chamber and with surgically implanted fine EMG wires. The animals' heads were immobilized by securing a surgically implanted head fixture to a custom-designed stereotaxic system (Fig. 1A). Multi-neuronal activity was recorded in non-sedated rats using ultra-thin microelectrodes or heptodes (80 -100 µm) from motor regions of STN, EP, VL thalamus, and primary motor cortex (MC). Validated waveforms were sorted using various clustering techniques and the firing patterns were then discriminated based on various classification metrics, like coefficient of variation and local variables.

6.3. RESULTS

Behavioral and motor activities, including dystonia, were assessed using a custom grid lined Plexiglass chamber and with surgically implanted fine EMG wires. Multi-neuronal activity was recorded in awake, head-restrained rats *at rest* using up to seven heptodes inserted into motor regions of STN, EP, VL pallidal-receiving thalamus, and layer 5 primary motor cortical (MC)

burst neurons. Neuronal activity in the STN and EP in recovered rats was heralded by slow rates with highly abnormally patterned activity, approximating that seen in dystonic animals.

Basal Ganglia Nuclei

STN and EP neurons in normal rats were characterized by regular (STN 43.32 ± 13 Hz / EP 48.73 ± 18 Hz) or irregular (STN 16.01± 5 Hz / EP 19.69 ± 6.9 Hz) patterned activity, while dystonic and recovered animals showed irregular (dystonic: STN 13.41±7.8 Hz /EP 8.61±6.7 Hz ; recovered: STN 9.81± 3.97 Hz /EP 11.42+2.7 Hz) or burst (dystonic: STN 21.00±15.6 Hz /EP 13.20±5.5 Hz; recovered: STN 16.90+8.7 Hz /EP 13.61± 3.7 Hz) patterned activity. With increasing severity of dystonia, discharge rates in GP and EP are progressively slower and GP neurons become more bursty. In recovered animals, the numbers of regular tonic neurons are appreciably higher than in dystonics and the extent of burstiness is less. Although STN neurons showed marked alterations in discharge rates and patterned activity with induction of dystonia, most of these abnormalities did not differ between recovered, mild and more severely dystonic conditions. Dystonic rats however did show considerably more spike count variability within irregular spike trains compared to recovered rats.

VL thalamus and MC.

Preliminarily, discharge activity in VL thalamus was appreciably slower (18.37 ± 4.2 Hz) in recovered compared to normal rats (25.34 ± 12 Hz), while burst (purported pyramidal) neuronal activity in MC in recovered rats did clearly differ from that of normal rats.

Synchrony. In recovered rats, 1/18 pairs of basal ganglia neurons showed synchronized discharge activity at rest, compared to 10/27 pairs in dystonic rats, and 0/13 in normals. The incidence and

the degree of synchrony between pairs of neurons did not evidently increase with worsening severity of dystonia.

Table 6.1. Resting discharge rates and patterned activity (n = 10 controls, 10 dystonic (7 mod to severe, 3 slight) and 3 spontaneously recovered Gunn rats)

Nuclei	Pattern	Normal	Recovered Rates
GP	**Regular**	(62) 45.9 ±13.47	(10) 27.6 ± 18.33
	Irregular	(42) 19.9 ±7.39	(30) 17.0 ± 10.08
	Bursty	(0) -	(7) 45.0 ± 19.39
	Non-stationary	(1) 43.3 ± 0	(2) 21.3 ± 0
EP	**Regular**	(64) 48.7 ± 18.80	(8) 35.6 ± 19.20
	Irregular	(54) 19.69 ± 6.9	(11)14.8 ± 5.63
	Bursty	(1) 20.7 ± 0	(14) 25.0 ± 9.12
	Non-stationary	(0) -	(1) 29.4 ± 0
STN	**Regular**	(52) 43.3 ± 13.37	(0) -
	Irregular	(48) 16.01 ± 5.43	(7) 13.2 ± 5.32

Bursty	(1) 22.4 ± 0	(10) 22.7 ± 7.4
Non-stationary	(1) 19.5 ± 0	(0) -

Table 6.2. Synchronized spike train pairs in GP and EP in normal, recovered, & dystonic rats

	# pairs	CC z>4	# pairs	CC z>4	# pairs	CC z>4	# pairs	CC z>4
GP	**7**	**0**	**8**	**0**	**5**	**2**	**7**	**3**
EP	**6**	**0**	**10**	**1**	**7**	**2**	**8**	**3**

6.4. DISCUSSION

Findings of persistent but lesser severe abnormal neuronal activity in the basal ganglia of spontaneously recovered animals suggest a specific threshold requirement to induce clinical dystonia. Further investigations are necessary to elicit how these specific abnormalities contribute directly to the induction of dystonia. The progressive changes in GP and EP neurons from normal to severely dystonic, compared to that of STN neurons, suggest a greater role for the GP-EP signaling pathway in secondary dystonia. The paucity of synchronized neuronal

discharge activity in the basal ganglia in rats recovered from acute dystonia compared to the high frequency for all severities of dystonia suggests that a loss of independent neuronal signaling in the basal ganglia is an integral feature of dystonia, but probably does not appreciably contribute to worsening severity of dystonia.

Importantly, our observation of abnormal discharge pattern in STN and EP in spontaneously recovered dystonic rats, suggest that to some extent, the abnormality of EP output to VL thalamus, is somehow probably is bypassed/ fixed at a level outside BG. Simultaneous recording from EP, VL and MC, would help explore the information transfer/ modulation at each of these level. The combined information collected from dystonic and recovered dystonic rats will help us to understand which abnormal signals are critical to inducing dystonic movements, as well as to provide preliminary insight into understanding auto-recovery in recovered animals.

CHAPTER 7

REFINED BASAL GANGLIA MODEL ACCOUNTING FOR GPI MODULATION OF THALAMIC TONIC AND BURST MODES.

7.1. INTRODUCTION

The basal ganglia (BG) integrates a wide range of cortical signals, processes them internally and then relays these modulated signals to the motor cortex via thalamus. The pallidal receiving ventrolateral (VL) thalamic nucleus is the major relay nucleus for the BG influence on the motor cortex. The BG has long been recognized as the key structure in the pallidothalamocortical circuit that receives inhibitory GABAergic signal from main output nuclei of the BG, globus pallidus internus (GPi; or its rat equivalent entopeduncular nucleus, EP), and transmits excitatory signals back to cortex. Despite its importance, the mechanism by which GPi regulates thalamocortical drive has not been satisfactorily scrutinized (less is known about how the basal ganglia influences motor behavior and learning through the thalamocortical output pathway). Although the classical BG rate model suggests that the inhibitory effect of GPi/EP has a direct *proportional* influence on the level of thalamocortical drive, the model cannot account for the benefits of GPi pallidotomy and DBS on both the hypo- and hyperkinetic features. According to the rate model, the reduced GABAergic activity in EP during rest activity should disinhibit thalamocortical drive. This explanation cannot readily account for our findings of excessive GABAergic activity in EP with movement, which oppositely should reduce not *induce* excessive

dystonic motor activity, per the model. The explanation lies behind the corresponding alterations or response in VL activity to EP GABAergic inputs.

Thalamic neurons in rats switch frequently between two distinct discharge patterns; a *tonic* mode and a *burst* mode. The tonic mode is highly dependent on synaptic inputs and is thought to be better graded and more responsive to the intensity of depolarizing inputs, while the burst mode is assumed to provide high detectability and throughput to the cortex (58, 59). The role of the burst mode remains controversial. Some investigators have claimed that the burst mode serves as the principal alerting mode, while others suggest that it is principally related to sleep activity (60). The burst mode is itself differentiated into two further patterns: 1) *arrhythmic*, occurring in both first-order (relay neurons, including pallidal-receiving) and higher-order (cortical-thalamic-cortical) neurons and 2) *rhythmic*, thought to be chiefly restricted to higher order neurons. Rhythmic bursting is common during quiet wakefulness and fast (13-15 Hz) thalamic oscillations have been associated with sleep-related learning (61).

The normal shift from the tonic to burst mode of firing in thalamic neurons has been attributed largely to synaptic-related hyperpolarization of the basal resting membrane potential (62, 63). This in turn, has been attributed to hyperpolarization-induced inactivation of voltage-gated T-type Ca^{2+} channels (64-66). Based on this and previous findings in EP and VL thalamus, it has been additionally hypothesize that excessive and abnormally synchronized dystonic movement related burst signaling in EP induces GABAergic-induced hyperpolarization of VL neurons, which in turn, leads to high throughput of crude basal ganglia movement related signals to the motor cortex instead of normal precision movement related pallidothalamocortical signals. Since

kernicterus and lesion models both induce dystonia, it was interesting to observe if the 'downstream' features at the level of VL and MC are similar in these two rodent models. While recordings at rest provide invaluable insight into normal and pathological signaling, we were interested in determining the normal role of burst and tonic signaling in VL and in MC, and in determining the abnormalities at the level of VL and MC during dystonic motor activity.

7.2. METHODS

7.2.1. Rats

In this chapter recordings from two different dystonic models, kernicterus model of dystonia (described in section 4.2.1) and lesion model of dystonia (described in Chapter 5) are investigated. Briefly, the kernicterus model is obtained from homozygous jaundiced Gunn rats. These rats are genetically deficient of UDP glucuronosyl transferase, the principal liver enzyme responsible for bilirubin clearance. All rats were injected with sulfhonamide at the age of 15-16 days, when their blood bilirubin levels are at their highest. The sulfonamide displaces the bilirubin from blood into the brain. The rat becomes dystonic within hours of injection. The prominent characteristics of dystonia in these rats include contorted posture, hind limb spread, and impaired righting reflex due to co-contracting antagonistic muscles. The lesion model of dystonia is obtained by lesioning the ventral-lateral part of motor territory of GP, which results in generation of contralateral dystonic symptoms within 4-5 hrs. The symptoms include contorted posture and hind limb spread similar to the kernicterus model of dystonia.

7.2.2. Surgery

Details of animal surgery, lesioning, neurophysiological recording and histology can be found in Sections, 4.2.3, 5.2, 4.2.4 and 4.2.5 respectively. Please refer to Chapter 2 for different strategies for multi-target and multi-nuceli recordings. All surgeries were carried out under isoflurane anesthesia. The rat's head and hip area were shaved and cleaned. An incision was then made along a sagittal plane and a custom stainless steel head fixture was firmly screwed into animal's skull. Relevant hindlimb muscles were surgically exposed and Teflon coated 50 μm stainless steel fine wire electrodes were inserted via a 30 gauge needle and sutured into the antagonistic hip muscles, while the other end of the micro-wire was soldered to a microcircuit board.

The following day, the rat's head was immobilized by clamping the head fixture into a custom stereotaxic positioner (Chaniary, et al., 2011). Under isoflurane anesthesia, a burr hole was drilled into the skull exposing the underlying duramater, targeting the hemisphere contralateral to the study hindlimb. Allowing for full behavioral recovery from effects of anesthesia, neuronal recording sessions were initiated 30-50 minutes after the surgery.

7.2.3. Data Processing and rest analysis

Spike detection and sorting techniques are detailed in Chapter 2. Firing pattern discrimination of neuronal population is described in Chapter 3. Further burst characterization and correlation analysis is detailed in section 4.2.8. In brief, the action potentials from continuous neuronal data were detected using a threshold detection method. Different sorting features (Section 2.2.2) of spikes data were plotted on a 2 or 3-D feature space and similar waveform originating from same neuronal unit are clustered using manual, K-mean or valley seek clustering techniques. The sorted waveforms were further validated for noise. Spike trains were rejected if more than 5% of

the ISIs were less than the absolute refractory period of 2 ms or the variance in the waveform shape was abnormally high.

Subsequently, all adequate spike rasters were subjected to a novel pattern discrimination algorithm. To characterize neurons into the three basic discharge patterns (regular, irregular and bursty), it was necessary to define three main features in the spike trains: Poissonian irregularity, burstiness and non-stationarity. The discrimination algorithm then calculated three proxy metrics; 'irregularity', 'burstiness', and 'corruption' for each of the above three features (Chapter 3). After calculating the tri-component values for each spike train, these data were plotted in a 3-D feature space and clustered into above three categories using K-mean clustering. Bursty spike trains were further characterized based on burst order and burst duration.

7.2.4. Movement analysis

During the awake head restraint condition, the rat's tail was gently pinched to stimulate active movement responses. The hind limb movements were registered via 1-4 hip and knee muscle EMGs (bicep femoris, vastus lateralis, gluteus superficialis, and gluteus medius). EMGs were simultaneously recorded with neuronal activities at a 40,000 sampling rate. Each unit was then recorded for 60-120 min, during which the rat was intermittently stimulated to perform active hind limb movement. Movement analysis was then performed using following methods.

7.2.4.1. Correlation of neuronal units with changes in EMGs

The correlation between the neuronal train and the processed EMG was calculated to assess the level of movement response of the neurons. The entire recording with both rest (baseline) and movement epochs was considered for analysis. The EMGs and the simultaneously saved

reliable neuronal units were recorded from all active channels were used for analysis. EMGs were first filtered (high pass filter with 5 Hz cut off and low pass filter with 500 Hz cutoff) and then rectified. The signal was then further processed using a derivative based algorithm with a window length of 0.2 sec followed by normalization. This processed EMG signal showed high amplitude only during muscle contractions. The sorted neuronal units were then placed into bins of 0.2 sec window and local variables (LVr, CV2, IR), instantaneous rate, and burst percentage were then determined. The cross-correlation function was then estimated for each unit and the corresponding EMG. Only $r > 0.5$ ($p < 0.05$) were considered to be movement related.

7.2.4.2. Type of observed movement responses (Peri-movement time analysis)

Peri-movement time analysis involves analysis of a segment of neuronal recording that is centered at the movement epoch. Each neuronal channel was isolated for each observed movement epoch of 3 sec duration with movement onsets aligned at 1.2 sec. Each of these epochs were subdivided into bins of 0.2 sec. Peridata (spike count per bin) was calculated for each bin. All peridata epochs were aligned with respect to the movement onset. Mean and SD of the baseline zone was then calculated. Each post baseline bin was categorized into baseline offset categories (BOC). The BOC is calculated based on level of increment, decrement, or neutral response with respect to baseline mean as follows

Condition	BOC
< (baseline - (2×SD))	-2
< (baseline - SD) AND > (baseline - (2×SD))	-1

> (baseline - SD) AND < (baseline + SD)	0
> (baseline + SD) AND < (baseline + (2×SD))	+1
> (baseline + (2× SD))	+2

The ‘mode’ (defined as most frequent or dominant offset category of any bin) was estimated.

7.2.5. Statistics

Statistical analyses were performed using MATLAB. Indifference between means of characteristic metrics of the two dystonic similar groups (kernicterus and lesioned rats) were assessed with two one-sided tests (TOSTs) for equivalence (Schuirmann, 1987) (Wellek, 2010). The mean values were considered to be significantly equivalent ($\alpha = 0.05$) if the 90% confidence interval was within the defined zone of indifference (± 5 spikes/sec for discharge rates and ± 0.2 for the tri-components). Differences in population distributions within the same and between different groups were assessed with one and two sample t-Tests. Difference between means of discharge rates, tri-component metrics, and burst parameters between groups were assessed using independent two sample t-Tests. Differences were determined to be statistically significant for p values less than 0.05.

7.3. RESULTS

7.3.1. Baseline properties during rest activity

Neuronal discharge activity was recorded from pallidal-receiving VL thalamus in normal and dystonic rats (n = 27 normal and 22 dystonic neurons) and in motor cortex (MC) layer V (n = 7

normal and 10 dystonic neurons) at rest and during movement. At rest, normal VL neurons showed a predominance of burst mode activity (71%). Tonic mode showed a comparatively rare occurrence (regular: 14% and irregular: 12%). In contrast, the tonic mode predominated in both dystonic rats (Kernicterus rats: irregular: 45%, regular: 32%; lesioned rats: irregular: 35%, regular: 35%). The population percentage of bursty neurons reduced greatly in VL in both kernicterus (16%) and dystonic rats (24%). MC shows a higher population of irregular neurons in normal rats (64%), while burst neurons were found to be scarcer (23%). The total population of bursty neurons increases to about 50% when the rat is dystonic (kernicterus: 52%; lesion: 50%). Figure 7.1.b indicates the feature histograms of neuronal population in VL and MC. The irregularity and burstiness spectrum in all three types of rats does not indicate any strong evidence for clear dichotomy of population in VL (all three populations, $p > 0.05$). The overall mean firing rate is reduced by ~40% in dystonic rats as compared to normal rats (kernicterus vs normal: 41.2%, $p < 0.05$; lesioned vs normal: 48.5%, $p < 0.05$). In distinction, cerebellar-receiving VPL thalamic neurons were not altered in dystonic rats (not shown in figures).

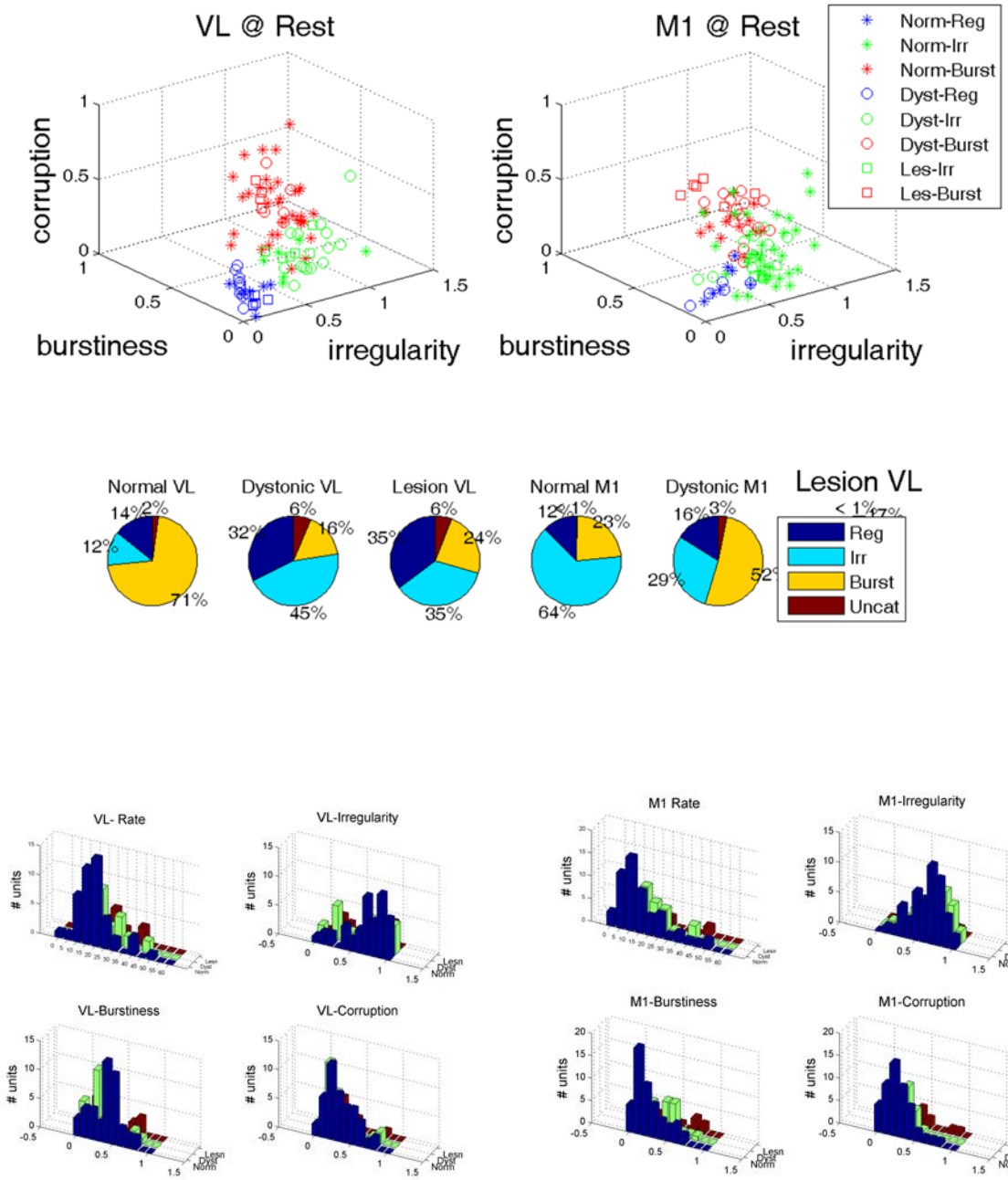

Figure 7.1: Characterization of neuronal patterns in different population in VL and MC: Tri-component feature space representation for VL thalamus and MC in normal, kernicterus and lesioned rats. Pie charts showing population distribution in above groups. Histogram showing variability in the characteristic features of each category: Rate, irregularity, burstiness and corruption.

Table 7.1: Population distribution of firing patterns in EP, VL and MC

Pattern	EP*			VL			MC		
	Normal	Dystonia	Lesion	Normal	Dystonia	Lesion	Normal	Dystonia	Lesion
Total	120	98	9	49	31	17	56	31	12
Tonic	118 (98%)	55 (56%)	4 (44%)	13 (27%)	24 **(77%)**	12 **(71%)**	43 **(77%)**	14 (45%)	4 (33%)
Bursty	0	38 (39%)	4 (44%)	35 **(71%)**	5 (16%)	4 (23%)	13 (23%)	16 **(52%)**	6 **(50%)**
Un-categorized	2 (1.7%)	5 (5%)	1(11%)	1 (2%)	2 (6%)	1 (1%)	0	1 (3%)	2 (16%)

7.3.2. Movement analysis

7.3.2.1. Correlation of neuronal units with movement related changes in EMGs

In VL in normal rats, tonic units showed weak to moderate correlation with movement. None of the regular neurons indicated strong movement, while three of the six slow irregular neurons have moderate correlation ($r = 05.8\text{-}0.6$, $p<0.05$). Out of 35 bursty neurons, 21 (60%) neurons showed moderate to high correlation with movement ($r = 0.621\text{-}0.761$, $p<0.05$). In MC, on the other hand, 78% (41 out of 52) of its neuronal population showed stronger movement correlation. In dystonic rats, in VL, only one regular neuron (out of 16) showed a correlation of 0.531. Five neurons (out of 20) showed correlation greater than 0.5 (range: 0.513-0.612). Four bursty (out of 9) neurons showed stronger correlation (range: 0.61-0.69). In MC, on the other hand, 31 out of 45 neurons were movement related.

7.3.1.2. Movement type (Peri-movement time analysis)

Since the rest and movement related activities (irregularity, burstiness, and response selectivity) in dystonia models of kernicterus and GP lesion model were equivalent ($p < 0.05$, two one-sided test for equivalency), further analyses were performed by combining the two groups.

Response selectivity

In VL of normal animals, 11 bursty and 2 slow irregular neurons showed higher response selectivity (+2), six bursty neurons showed response selectivity of +1, four bursty neurons and one slow irregular neuron indicated negative response selectivity (-1). In VL of dystonic animals, three bursty neurons and two irregular neurons showed response selectivity of +2, one bursty neuron and three irregular neurons indicated response selectivity of +1, while one regular neuron showed response selectivity of -1. In MC of normal rats, 19 neurons showed response selectivity of +2, six neurons showed +1 and 16 units showed -1. While in dystonia, 13 neurons showed (+2), 10 neurons showed (+1), and eight neurons had a response selectivity of (-1).

Zone-wise movement response

In normal rats, VL neurons showed a prominent step ramp in spike counts preceding EMG onset, compared to a flatter response in dystonic rats (Fig 7.2). VL neurons predominately maintained the burst mode under resting state in normal rats. During movement, the neuron's response preceded the movement onset by 0.4± 0.15 sec. All movement related VL neurons in normal rats responded by modulating the inter- and intra-burst properties by: (i) increasing the burst order (BO) from 2.6± 0.4 to 5.05±0.23; (ii) increasing the burst duration (BD) from 0.015± 0.005 s to 0.03±0.004s; and (iii) reducing the intraburst frequency by 22%. The overall burstiness in VL do

not change significantly with the movement onset, but show a transient decrement indicating the end of epoch (fig 7.2.b). None of the normal VL neurons showed any changes in mode with movement. In dystonic rats, with movement, VL neurons largely switched to the burst mode, but neuronal firing only poorly followed EMG activity and 'erroneously' resembled burst activity of normal rats at rest. The intraburst properties of movement related burst discharge in dystonic firing are erroneously similar, especially IBF, to that of rest activity in normal rats.

The burst properties during movement in dystonia did not reach the normal movement levels (BO: 3.1±0.04 and BD: 0.02±0.003). Further, in dystonic rats, the plateau for the spike counts abnormally extend during the prolonged EMG co-contractions with the normal sharp offset at the end of the EMG epochs.

In MC, dystonic rats showed attenuated increments in spike counts (slope of increment) prior to movement onset and an abnormal reduction in burstiness after the onset of movement (fig 7.3). In MC, pyramidal neurons failed to achieve peak discharge frequencies in relation to movement as shown in fig 7.3. These neurons, in contrast to normals, begin to silence early with respect to the end of movement, though in line time-wise with normals. Burstiness levels in MC correlate poorly with the movement in dystonic rats. MC in normal rats, has moderately more positive selectivity, however in dystonics negative selectivity goes down.

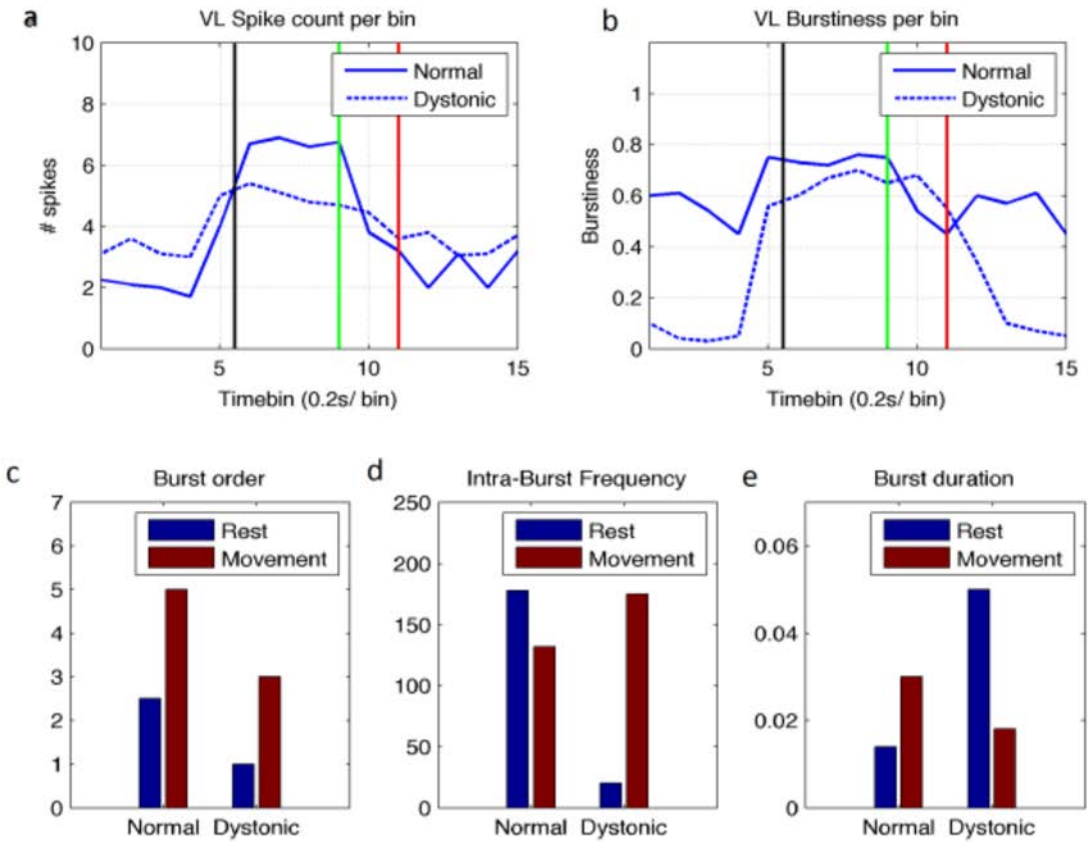

Fig 7.2. VL neuronal-EMG correlations and LTS bursts in normal vs dystonic rats. a. Neuronal spike activity in VL can be seen to poorly modulate with movement and fail to achieve peak spike intensity in dystonic rats **b**. Burstiness of VL neurons approaches that of normal rats with movement. **c.** However, the intra-burst features (likely to be integral to accurate movement signaling) are highly abnormal in dystonic rats. In figs a, b, black, green, and red lines indicate onset of movement, offset of normal and offset of dystonic motor activity (data are averaged over multiple movement epics and time axis is normalized for comparison).

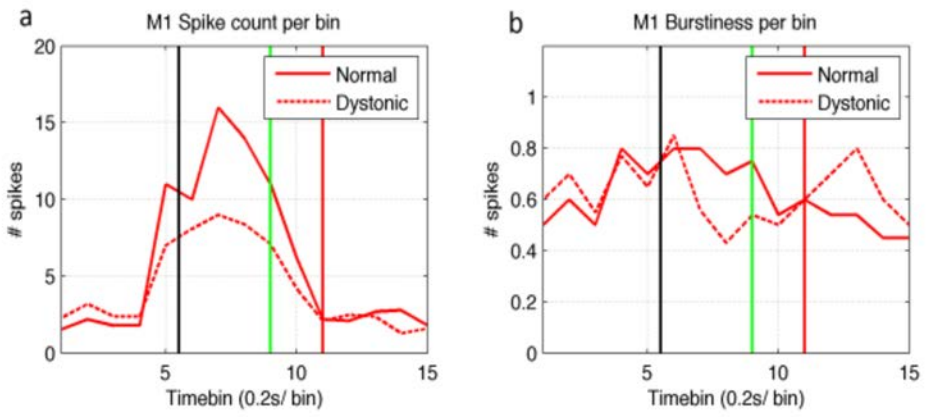

Fig 7.3. **MC neuronal-EMG correlations in normal vs dystonic rats. A.** spike count/ bin **B.** Burstiness level per bin. Black, green, and red lines indicate onset of movement, offset of normal and offset of dystonic motor activity (data are averaged over multiple movement epics and time axis is normalized for comparison).

DISCUSSION

The principal finding in this study was the dominance of burst discharge activity at rest in normal rats and the tonic mode in dystonic rats in pallidal receiving thalamus (VL). Normally with moderate GABAergic 'pacemaker' rest-state input from EP, neurons in VL are chiefly in burst mode. However, in dystonia, with reduced EP rates and associated GABAergic input chaotic pattern, the neurons are erroneously in the tonic mode. This finding discounts the classical rate model hypothesis, that inputs from EP 'directly' inhibit the neurons in VL. Instead it can be suggested that normally GABAergic resting input from EP hyperpolarizes a majority of VL neurons and holds them chiefly in the baseline 'ready' burst mode. The reduced GABAergic input from EP under dystonic condition, results in inadequate hyperpolarization of the cell membrane in VL neurons. This results in switching of the membrane potential of low threshold

spike (LTS) neurons of VL to Na^+/K^+ driven tonic mode.

Reduced excitability of the neuronal membrane or in this case increased presynaptic inhibition from EP (caused by initial ohmic leakage current, Na^+ and K^+) causes sustained hyperpolarization of the thalamic neurons (<-60 mV). T-type Ca^{2+} channels de-inactivates under this hyperpolarized state, and an influx of Ca^{2+} current (I_T) starts, which causes large transient membrane depolarization. This activates Ca^{2+} activated K^+ conductance (delayed rectifier) allowing efflux of K^+, hyperpolarizing the membrane. If this hyperpolarized state is sustained for at least 100 ms it de-inactivates I_T, resulting in a long lasting Ca^{2+} spike, called low threshold spike (LTS). These LTS are crowned by LT burst of Na^+ and K^+ spikes. The amplitude of Ca^{2+} spikes primarily depends upon the level of hyperpolarization. The depolarizing input, however, is presumed to be important for initial activation. The delayed K^+ channel also influences the amplitude of LTS. However, if there is reduced presynaptic inhibition, the LTS would switch to tonic mode.

From this study it was also concluded that in VL, burst mode is the more important and more responsive mode in thalamic function. Loss of bursty units in dystonia results in less response selectivity to movement epochs. A finding from this work is that the burst mode is the principal mode for motor signaling. Under dystonic tonic state, VL would necessarily need to then switch to the burst mode to signal movement. Since this switch requires 50-100 ms, this would be expected to be associated with a significant delay in the reaction time and affect the overall coordinated temporal timing of motor signaling. Additionally, in particular, with movement, VL neurons in dystonic rats are able to largely shift from the erroneous tonic to the desired burst

mode, but many facets of the temporal timing of the burst activity and the details conveyed by the intra-burst features, including BO, BD, and IBF, are highly abnormal. Thus, in dystonia, reduced GPi GABAergic resting output largely places VL LTS neurons erroneously in the tonic mode with delayed and inaccurate switching to the desired burst mode. These findings suggest that interventions aimed to correct these defined abnormalities at the level of the motor thalamus could offer a good approach to reversing the underlying signaling abnormalities and ameliorating dystonia.

The findings in MC reveal changes of increased burstiness and discharge rates. The neuronal/EMG correlations here revealed high signaling abnormality in VL, which translate to abnormal signaling in MC, which in turn leads to poor muscle control in dystonia.

CHAPTER 8

CONCLUSION AND FUTURE WORK

Although traditional basal ganglia circuitry models provide an invaluable framework for conceptualizing basal ganglia connections, rate-based models have major limitations. Firstly, the models necessitate that various movement disorders can be attributed specifically to pathological alterations in neuronal discharge rates. Yet, discharge rates in GP (Bezard et al., 1999) (Boraud et al., 2001) (Raz et al., 2000), EP (Raz et al., 2000) (Bergman et al., 1994) (Wichmann & DeLong, 1999), and thalamus (Pessiglione et al., 2005) are not clearly altered in animal models of PD. Secondly, while rate models correctly predict that pallidotomy (GPi ablation) should improve hypokinesia (reduced movements) in PD patients (by disinhibiting thalamocortical activity), current models cannot likewise account for comparable surgical benefits of pallidotomy on medication-induced dyskinesias (*excessive* movements) in these patients (Lozano et al., 1995) (Baron et al., 1996). Thirdly, in PD patients undergoing deep brain stimulator (DBS) surgery, intra-operative induction of dyskinesias can be associated with alterations in phasic patterned neuronal activity in GPi without corresponding changes in the discharge rates (Lee et al., 2007). In this work the contribution of alterations in discharge rates, as well as that of patterned discharge activity to normal and dystonic motor activity in Gunn rats was investigated. These studies have major implications not only for dystonia, but also for understanding other movement disorders and the normal control of motor function.

Towards this aim, a system was developed and modified to facilitate appropriate recording and analysis of neuronal-EMG signals from normal and dystonic rats. This is a very important step as

this dictates the reliability and robustness of the data and analysis. Considering the damage caused by multiple electrode tracks, different targeting strategies were developed which allows to simultaneously recording from multiple targets and multiple neurons, reducing the requirement to make unwanted additional tracks. Unlike many other in vivo studies which were performed under anesthesia and had inadequate control for movement during recording, the current study used awake head restrained system for recording.

To allow comprehensive and reliable analysis of the multi-channel neuronal data a MATLAB based application, 'NeuroPAM', was developed. The current version of NeuroPAM provides the possibility of a complete operation using a graphical-User Interface (GUI). It provides quick and reliable tools for processing continuous data, such as EMG, LFP, and EEG as well as spike detection-sorting-clustering. It also offers automated implementation of several point process and other statistical techniques and algorithms. Notable applications include a tool box for comprehensive spike data analysis toolbox, Moran I and GI* values for spatial statistics, peri-event movement analysis pack, and tri-component algorithm. The tri-component algorithm is a robust and reliable method for discriminating firing patterns in different neuronal populations. Finally, NeuroPAM also offers various neuronal simulation and modeling tools for testing and implementing new algorithms.

The next step, in this study was to test the proposed hypothesis. The primary hypothesis of this study was that the BG is an important component in motor control network and abnormality in its components causes various motor dysfunctions. First, the neuronal behavior in BG of normal and dystonic rats were characterized. It was concluded that the BG neurons, under dystonic condition, fires abnormally slow and further is irregular and bursty. Under burst dominated

input-output condition, the auto-stabilizing and dual projection loops within BG, generate abnormal synchrony among neurons. This synchrony is prominent with movement related cortical inputs. Many motor related GP (or GPi) neurons goes silent with dystonic movement epochs. Reduction in overall rest firing rate and synchronized movement related silencing of GP indicates its importance in dystonic pathophysiology. To further test this hypothesis, GP outputs were blocked using ibotenic lesions. Interestingly, based on the location of the lesion within GP motor territory, the animal acquired varying motor disorders. The dorsal lesions generated parkinsonism, while ventral lesions generated dystonia. This finding suggest that anatomically different circuits within GP regulate different aspects of motor control. Also, the neurons of the main output nuclei of BG, EP (or GPi), showed elongated synchronous bursting with dystonic movement epochs. Additionally, the prominent alterations in neurons in pallidal receiving VL thalamus, under dystonia, results in a change in firing mode from burst to tonic. This discounts the classical rate model, as the alterations in EP output are not inversely proportional to the alterations in thalamic rate. This highlights a major drawback in classical BG rate model that EP is not 'directly' inhibiting VL neurons. The novel hypothesis based on in vivo experimental observations, is that EP is controlling the hyperpolarization level of the cell membranes of VL neurons. This ultimately designates EP as the primary firing mode modulator of the VL neurons. Moderate and regular presynaptic inputs from EP, sustains the hyperpolarization state of VL LTS neurons, thus generating low threshold Ca^{2+} spikes crowned by Na^{+}/K^{+} bursts. Under dystonic conditions, the EP resting output is reduced and is more chaotic. This leads to inadequate hyperpolarization and thus a mode shift of the VL neurons to the tonic mode.

Our observations in neuronal recordings in basal ganglia nuclei, thalamic nuclei and motor cortex in normal, dystonic and lesioned rats lead to the development of a '***novel basal ganglia thalamocortical (BGTC) circuitry model'*** (Fig 8.1) that also illustrates the pathophysiology of dystonia. Under dystonic conditions, the nuclei of basal ganglia alter their normal baseline activities and fires in an abnormal reduced, increased irregular and bursty mode. From our studies with dystonic rats, it was observed that during motor dysfunction, the involuntary abnormal movements are preceded by different abnormal neuronal firing patterns. We previously observed that highly synchronized movement related alterations in neuronal discharge activity in globus pallidus (GP ~ external globus pallidus, GPe in primates) and entopenduncular nucleus (EP ~ internal globus pallidus, GPi in primates) were associated with co-contractions of antagonistic muscles and overflow contractions of the nearby muscles. The abnormal movement related silencing in GP is relayed to EP directly or via indirect pathway (STN). The auto-stabilizing loop between GP and STN, causes abnormally enhanced synchronized movement related neuronal firing. This enhanced synchrony leads to a loss of specificity among the BG neurons.

Ultimately the abnormal EP (main BG output nuclei to thalamus) signaling causes inadequate VL hyperpolarization. The abnormal reduced hyperpolarization of VL resulting in the loss of appropriate normal burst signaling causing it to fire 'mostly' in abnormal tonic mode. In addition, the movement related synchronized bursting in EP results in abnormally signaled movement related burst activities. These abnormalities when relayed back to motor cortex leading to imprecise bursting activities. The loss of specificity and phase relationship ultimately leads to simultaneous or untimely activation of the antagonistic and other undesired muscles.

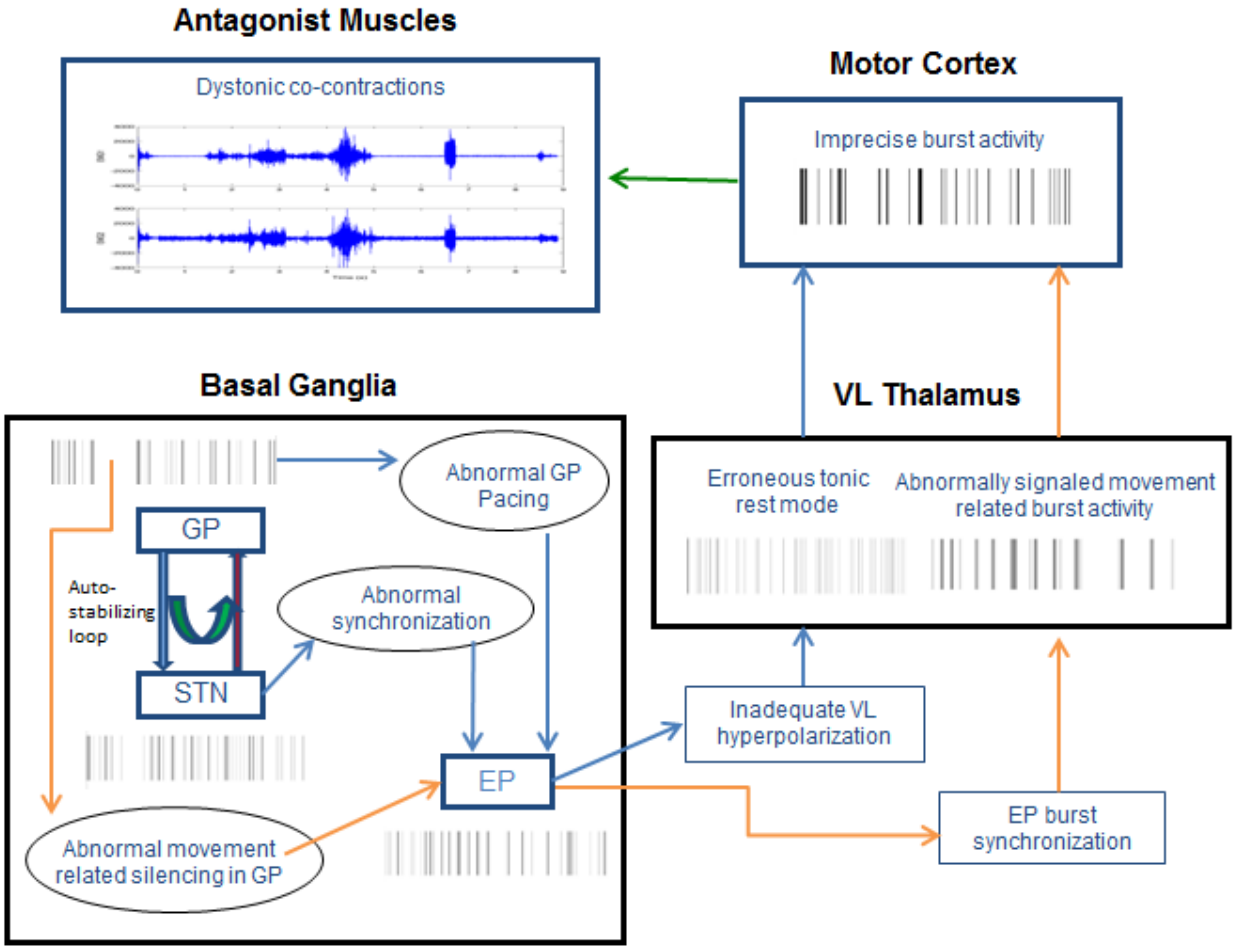

Fig 8.1. Novel BGTC model

8.2. FUTURE WORK

Based on the current findings following future studies are suggested:

1. **Optogentics in rat models**

Optogenetics is a new, powerful technique, which will permit to greatly enhance the understanding of dystonia by simulating dystonic neuronal signals in normal animals and to test therapeutic approaches by modulating the pathological signals in dystonic rats. Optogenetics is a relatively new field that offers a tremendous advancement over electrical stimulation. Opsins with properties similar to those in the human retina are naturally ubiquitous in various bacteria and algae. Their utility to experimentally depolarize or hyperpolarize neurons via illumination was also reported. By transfecting opsins into neurons with viral vectors, neuronal spiking and synaptic events can be controlled with very high spatial and temporal resolution. Photostimulation permits delivery of continuous, highly controllable subthreshold photocurrents to more naturally mimic synaptic activity. Photostimulation can precisely target neurons of interest without confounding electrical stimulation of fibers of passage. Additionally, photostimulation obviates intrusive stimulation artifacts, which limit combined electrical stimulation and recording studies. Because electrical stimulation could nevertheless offer faster applicability via DBS in humans, we will use electrical stimulation, as applicable, to test any potential control and therapeutic discoveries.

2. Closed loop control and coordinated reset in DBS in Parkinson and dystonic patients

Deep brain stimulation is a neurosurgical procedure used to treat different neurological disorders, including basal ganglia related motor disorders, like Parkinson's disease and dystonia. A neuro-stimulation electrode is implanted in a particular target nuclei in brain and high frequency electrical impulses are sent which have striking therapeutic effects. We intend to implement our findings and understandings from our rat studies in improvements and modifications in DBS treatments in patients. The project will focus on development of brain computer interface and closed loop control of deep brain stimulation. The project will utilize a multidisciplinary approach to characterize and restore normal basal ganglia functioning in movement disorders (PD, dystonia) using complex stimulation control algorithms. The algorithms will include detection of abnormal LFP and spike firing characteristics and stimulate with different pulse patterns in order to reduce the power in certain frequency bands. This would also include coordinated reset (CR) neuromodulation (independent differential stimulation of two regions in the basal ganglia) that improves DBS benefits on PD via strategically interrupting synchronization, with persistent therapeutic effects.

LITERATURE CITED

Albin, R., Young, A. & Penney, J., 1989. The functional anatomy of basal ganglia disorders. *Trends Neurosci.*, 12(10), pp.366-75.

Aldridge, J.W., Berridge, K.C. & Rosen, A.R., 2004. Basal ganglia neural mechanisms of natural movement sequences. *Can. J. Physiol. Pharmacol. 8*, 82, pp.732-39.

Alexander, G.E. & DeLong, M.R., 1986. Organization of supraspinal motor systems. In *Diseases of the Nervous System*. Asbury, McKhann, McDonald: Ardmore Medical Books. pp.352-69.

Alexander, G., DeLong, M. & Strick, P., 1986. Parallel organization of functionally segregated circuits linking basal ganglia and cortex. *Annual Review of Neuroscience*.

Amorim, R.C.d., 2011. *Learning feature weights for K-Means clustering using the Minkowski metric Feature Selection Algorithms: A Survey and Experimental Evaluation*. Birbeck: University of London.

Anon., 2012. *PhysiologyWeb*. [Online] Available at: http://www.physiologyweb.com/lecture_notes/neuronal_action_potential/neuronal_action_potential_refractory_periods.html [Accessed March 2013].

Anteneodoa, C., Malmgrenb, R.D. & Chialvoc, D.R., June 12, 2010. Poissonian bursts in e-mail correspondence. *European Physical Journal*, B 75, pp.389-94.

Bar-Gad, Bronfeld & Izhar, 2011. Loss of specificity in basal ganglia related movement disorders. *Frontiers in system neuroscience*.

Bar-Gad, I., Havazelet, H. & Goldberg, R., 2000a. Reinforcement driven dimensionality reduction - a model for information processing in the basla ganglia. *Journal of basic and clinical physiology and pharmacology*.

Baron, M.S., Chaniary, K.D., Rice, A.C. & Shapiro, S.M., 2011. Multi-neuronal recordings in the basal ganglia in normal and dystonic rats. *Frontier of System Neuroscience*.

Baron, M. et al., 1996. Treatment of advanced parkinson's disease by posterior GPi pallidotomy: 1-year results of a pilot study. *Ann Neurol.*.

Baron, M., Wichmann, T., Ma, D. & Delong, M., 2002. Effect of transient focal inactivation of the basal ganglia in parkinsonian primates. *J. Neurosci.*, 22(2), pp.592-99.

Barto, 1995. Adaptive critics and the basal ganglia. In *Model of information processing in the basal ganglia*.

Beiser, D.G. & Houk, J.C., 1998. Model of Cortical-Basal Ganglionic Processing: Encoding the Serial Order of Sensory Events. *J Neurophy*, 79.

Benhamou, L., Bronfeld, M., Bar-Gad, I. & Cohen, D., 2012. Globus Pallidus external segment neuron classification in freely moving rats: A comparison to primates. *PLOS one*, 7(9).

Bergman, H., Wichmann, T., Karmon, B. & DeLong, M., 1994. The primate subthalamic nucleus. II. neuronal activity in the MPTP model of parkinsonism. *J Neurophysiol*, 2(507-20), p.72.

Bevan, M., Booth, Eaton & Bolam, 1998. Selective innervbation of neostriatl interneurons by a subclass of neuron in the globus pallidus of the rat. *J Neurosci*.

Bezard, E., Boraud, T., Bioulac, B. & Gross, C., 1999. Involvement of the subthalamic nucleus in glutamatergic compensatory mechanisms. *Eur J Neurosci*, 11(6), pp.2167-70.

Black, K. et al., 2014. Spatial reorganization of putaminal dopamine D2-like receptors in cranial and hand dystonia. *PLoS One*, 9(2).

Boraud, T., Bezard, E., Bioulac, B. & Gross, C., 2001. Dopamine agonist-induced dyskinesias are correlated to both firing pattern and frequency alterations of pallidal neurones in the MPTP-treated monkey. *Brain*, 124(3), pp.546-57.

Borst, A. & Theunissen, F.E., 1999. Information theory and neural coding. *Nature Neuroscience* , pp.947 - 957.

Boston, Dum & Strick, 2010. The basal ganglia coomunicate with the cerebellum. *Proc Natl Acad Sci*.

Brochini, L., Carelli, P. & Pinto, R.D., 2011. Single synapse information coding in intraburst spike patterns of central pattern generator motor neurons. *The Journal of Neuroscience*.

Burns, C., 1993 a. A model for the functioning of striatum. *Biol cybern*.

Chaniary, K., 2010. *Electrophysiological analysis in an animal model of Dystonia*. Richmond: Virginia Commonwealth University.

Chaniary, K. et al., 2009. Quantification of gait in dystonic Gunn rats. *J. Neurosci. Methods*, 180(2), pp.273-77.

Chaniary, K. et al., 2008. Electromyographic characterization in an animal model of dystonia. *Mov. Disord.*, 23(8), pp.1122–29.

Chaniary, K. et al., 2011. A novel stereotaxic apparatus for neuronal recordings in awake head-restrained rats. *J. Neurosci. methods*, 198(1), pp.29-35.

Chen, L. et al., 2009. Detection of bursts in neuronal spike trains by the mean inter-spike interval method. *Progress in Natural science*, pp.229-35.

Chen, C.C. et al., 2006. Neuronal activity in globus pallidus interna can be synchronized to local field potential activity over 3–12 Hz in patients with dystonia. *Experimental Neurology*.

Christodoulou, C. & Bugmann, G., 2001. Coefficient of variation vs. mean interspike interval curves: What do they tell us about the brain? *Neurocomputing*, pp.1141-49.

Churchland, M.M. et al., 2010. Stimulus onset quenches neural variability: a widespread cortical phenomenon. *Nature Neuroscience*, (doi:10.1038/nn.2501).

Contreras-vidal, S., 1995. A neural model of basal ganglia-thalamocortical relations in normal and parkinsonian movement. *Biol Cybern*.

Davies, R.M., Gerstein, G.L. & Baker, S.N., 2006. Measurement of time-dependent changes in the irregularity of neural spiking. *Journal of Neurophysiology*, 96, pp.906-18.

DeLong, M., 1990. Primate models of movement disorders of basal ganglia origin. *Trends Neurosci.*, 13(7), pp.281-5.

DeLong, M. & Georgopoulos, A., 1981. Motor functions of the basal ganglia. In M. Brookhart, V.B. Mountcastle & V.B. Brooks, eds. *Handb. Physiol., Sect. 1 , The Nervous System, Vol. 2, Motor Control, Part 2, ed. 1*. Bethesda: Am. Physiol. Soc. pp.1017-61.

Demsar, 2006. Statistical comparisons of classifiers over multiple data sets. *Journal of Machine Learning Research*, 7, pp.1-30.

DeWeese, M.R., Wehr, M. & Zador, A.M., 2003. Binary spiking in auditory cortex. *The Journal of Neuroscience*, 23(21), pp.7940-49.

Doane, D.P. & Seward, L.E., 2011. Measuring skewness: A forgotten statistic ? *Journal of Statistics Education*, 19.

Eden, U.T. & Kramer, M.A., 2010. Drawing inferences from Fano factor calculations. *Journal of Neuroscience Methods*, 190, pp.149–52.

Eltahawy, H. et al., 2005. Primary dystonia is more responsive than secondary dystonia to pallidal interventions: outcome after pallidotomy or pallidal deep brain stimulation. *Neurosurg.*, 54(3), pp.613-19.

Feng, J. & Brown, D., 1999. Coefficient of variation of interspike intervals greater than 0.5. How and when ? *Biological Cybernetics*, 80, pp.291-97.

Ferstl, R., 2007. Spatial Filtering with EViews and MATLAB. *Aust. J. Stat.*, 36(1), pp.17-26.

Filion, M. & Tremblay, L., 1991. Abnormal spontaneous activity of globus pallidus neurons in monkeys with MPTP-induced parkinsonism. *Brain Res.*, 541(1), pp.142-51.

François, C. et al., 2004. Behavioural disorders induced by external globus pallidus dysfunction in primates II. Anatomical study. *Brain*, 127, pp.2055-70.

Gaudry, K.S. & Reinagel, P., July 25, 2007. Benefits of contrast normalization demonstrated in neurons and model cells. *The Journal of Neuroscience*, 27(30), pp.8071– 8079.

Gebber, G.L., 2006. Fractal Noises and motions in time series of presympathetic and sympathetic neural activities. *Journal of Neurophysiology*, 95, pp.1176-84.

Getis, A. & Ord, J., 1992. The Analysis of Spatial Association by Use of Distance Statistics. *Geogr. Anal.*, 24, pp.189-206.

Geyer, H. & Bressman, S., 2006. The diagnosis of dystonia. *Lancet Neurol.*, 5(9), pp.780-790.

Goltsev, L.L.M., Nov, 2012. Critical and resonance phenomena in neural networks.

Grahna, J., Parkinsonb, J. & Owena, A., 2009. The role of the basal ganglia in learning and memory:Neuropsychological studies. *Behavioural Brain Res*.

Grahn, J., Parkinson, J. & Owen, A., 2008. The cognitive functions of the caudate nucleus. *Progress in Neurobiology*.

Graybiel, A.M., 2005. The basal ganglia: learning new tricks and loving it. *sciencedirect: Current Opinion in Neurobiology*.

Grosse, P. et al., 2004. Patterns of EMG-EMG coherence in limb dystonia. *Mov Disord.*, 19(7), pp.758-769.

Gross, R.E. et al., 1999. Relationship of lesion location to clinical outcome following microelectrode-guided pallidotomy for Parkinson's disease. *Brain*, 122, pp.405-16.

Gurney, K., Prescott, T.J. & Redgrave, P., 2001. A computaional model of action selection in the basal ganglia. I A new functional anatomy. *Biological Cybernetics*.

Gurney, K., Prescott, T.J. & Redgrave, P., 2001. A computaional model of action selection in the basal ganglia. II analysis and simulation of behaviour. *Biological cybernetics*.

Haber, S., 2003. The primate basl ganglia: parallel and integrative networks. *J. Chem. Neuroanat.*, 26(4), pp.317-30.

Hanley, B. & Bevan, B., 2000. Synaptic Orgnaization of the Basal Ganglia. *J Anat*.

Heeger, D., 2000. *Poisson Model of Spike generation*.

Herrero, M., Barcia, C. & Navarro, J., 2002. Functional anatomy of thalamus and basal ganglia. *Childs Nerv Syst.*, 18(8), pp.386-404.

Hiromi, S. et al., 2013. Signals through the Striatopallidal Indirect Pathway Stop Movements by Phasic Excitation in the Substantia Nigra. *The Journal of Neurosci*.

Holloway, K.L. et al., 2006. Deep brain stimulation for dystonia: a meta-analysis. *Neuromodulation*, 9, pp.253-61.

Holt, G.R., Softky, W.R., Koch, C. & Douglas, J.R., 1996. Comparison of discharge variability in vitro and in vivo in cat visual cortex neurons. *Journal of Neurophysiololgy*, 75, pp.1806-14.

Hoover, J. & Strick, P., 1993. Multiple output channels in the basal ganglia. *Sci.*, 259(5096), pp.819-21.

Hoshi et al., 2005. The cerebellum communicates with the basal ganglia. *Nature Neuroscience*.

Houeto, J.L. et al., 2007. Acute deep-brain stimulation of the internal and external globus pallidus in primary dystonia: functional mapping of the pallidum. *Arch. Neurol.*, 64, pp.1281–86.

Houk, D. & Beiser, J., 1995. *Models of information processing in the basl ganglia*. Cambridge: MIT Press.

Hutchison, W. et al., 1997. Identification and characterization of neurons with tremor-frequency activity in human globus pallidus. *Exp. Brain Res.*, 113(3), pp.557-63.

Kaneoke, Y. & Vitek, J.L., 1996. Burst and oscillation as disparate neuronal properties. *Journal of Neuroscience Methods*, (68), pp.211-23.

Kelman, C., Ramakrishnan, V., Davies, A. & Holloway, K., 2010. Analysis of stereotactic accuracy of the cosman-robert-wells frame and nexframe frameless systems in deep brain stimulation surgery. *Stereotact. Funct. Neurosurg.* , 88(5), pp.288-95.

Kisore, A. et al., 2000. Evidence of functional somototopy in GPi from results of pallidotomy. *Brain*, 123, pp.2491-500.

Knappskog, P. et al., 1995. Recessively inherited L-dopa-responsive dystonia caused by a point mutation (Q381K) in the tyrosine hydroxylase gene. *Hum. Mol. Genet.*, 4, pp.1209-12.

Krack, P. et al., 1998. Opposite motor effects of pallidal stimulation in Parkinson's disease. *Ann. Neurol.*, 43, pp.180-92.

Kumbhare, D. & Baron, M., 2015. A novel tri-component scheme for classifying neuronal discharge patterns. *J. Neurosci. Methods*, 239, pp.148-61.

Kumbhare, D., Chaniary, K. & Baron, M.S., 2015. Preserved dichotomy but highly irregular and burst discharge in the basal ganglia in alert dystonic rats at rest. *Brain Res.*, I624, pp.297-313.

Kuoppamaki, M. et al., 2005. Parkinsonism following bilateral lesions of the globus pallidus: performance on a variety of motor tasks shows similarities with Parkinson's disease. *J. Neurol. Neurosurg. Psychiatry*, 76, pp.482-90.

Leblois, A. et al., 2010. Deep brain stimulation changes basal ganglia output nuclei firing pattern in the dystonic hamster. *Neurobiology of Disease*, 38, pp.288-98.

Lee, J. et al., 2007. Internal pallidal neuronal activity during mild drug-related dyskinesias in parkinson's disease: Decreased firing rates and altered firing patterns. *J Neurophysiol.*, 97(4), pp.2627-4.

Legéndy, C. & Salcman, M., 1985. Bursts and references of bursts in the spike trains of spontaneously active striate cortex neurons. *Journal of Neurophysiology*, 53(4), pp.926-39.

Leh, S., Ptito, A., Chakravarty, M. & Strafella, A., 2007. Fronto-striatal connections in the human brain: A probabilistic diffusion tractography study. *Neurosci Lett.*, 419(2), pp.113-8.

Lenz, F. et al., 1998. Pallidal activity during dystonia:somatosensory reorganization and changes with severity. *J Neurol Neurosurg Psychiatry*, 65(5), pp.767-70.

Lerchner, A., Ahmadi, M. & Hertz, J., 2004. High-Conductance states in a mean-field cortical network model. *Neurocomputing*, pp.935-40.

Lozano, A. et al., 1995. Effect of GPi pallidotomy on motor function in parkinson's disease. *Lancet*, 346(8987), pp.1383-7.

MacQueen, J., 1967. Some methods for classification and analysis of multivariate observations. In *5th Berkeley Symposium on Mathematical Statistics and Probability*. University of California Press, 1967.

Maimon, G. & Assad, J.A., 2009. Beyond Poisson: increased spike-time regularity across primate parietal cortex. *Neuron*, (62), pp.426–40.

Markus, B., Julia, S., Jochen, R. & Gaby, S., 2011. Measuring burstiness and regularity in oscillatory spike trains. *Journal of Neuroscience Methods*, pp.426-37.

Martinson, J., Webster, H.H., Myasnikov, A.A. & Dykes, R.W., 1997. *Recognition of temporally structured activity in spontaneously discharging neurons in the somatosensory cortex in waking cats*. Elsevier Brain Research 750.

McFarland, N. & Haber, S., 2002. Thalamic Relay Nuclei of the Basal Ganglia Form Both Reciprocal and Nonreciprocal Cortical Connections, Linking Multiple Frontal Cortical Areas. *The Journal of Neuroscience*.

McIntyre, R. & Wichmann, T., 2012. Basal ganglia activity patterns in parkinsonism and computaional modeling of their downstream effects. *Eur J neuroscience*.

Merello, M. et al., 2004. Neuronal globus pallidus activity in patients with generalised dystonia. *Mov Disord*, 19(5), pp.548-54.

Mink, J., 1996. The basal ganglia: focused selection and inhibition of competing motor programs. *Prog Neurobiol.* , 50(4), pp.381-425.

Mink, J., 2003. The basal ganglia and involuntary movements: Impaired inhibition of competing motor patterns. *Arch Neurol.*, 60(10), pp.1365-8.

Mink, J. & Thach, W., 1991. Basal ganglia motor control. II. Late pallidal timing relative to movement onset and inconsistent pallidal coding of movement parameters. *J Neurophysiol.* , 65(2), pp.301-29.

Mitchell, A., 2005. *The ESRI Guide to GIS Analysis, Volume 2*. 1st ed. ESRI Press.

Mitra, P. & Bokil, H., 2007. *Observed brain dynamics*. Oxford University Press.

Miura, K., Okada, M. & Amari, S., 2006. Estimating spiking irregularities under changing environments. *Neural Computation*, 18, pp.2359–86.

Miura, K., Tsubo, Y., Okada, Y. & Fukai, T., 2007. Balanced excitatory and inhibitory inputs to cortical neurons decouple firing irregularity from rate modulations. *The Journal of Neuroscience*, 27(50), pp.13802–12.

Moran, P.A.P., 1950. Notes on Continuous Stochastic Phenomena. *Biometrika*, 37(1), pp.17–23.

Münchau, A. et al., 2000. Unilateral lesions of the globus pallidus: report of four patients presenting with focal or segmental dystonia. *Neurol. Neurosurg. Psychiatry*, 69(4), pp.494-42.

Nambu, A., 2004. A new dynamic model of the cortico-basal ganglia loop. *Progress in Brain Research*.

Nambu, A., 2011. Somatotopic organization of the primate Basal Ganglia. *Front Neuroanat.*, 5(26).

Nambu, A. et al., 2011. Reduced pallidal output causes dystonia. *Frontiers in system neuroscience*.

Obeso, J.A., Rodríguez-Oroz, M.C., Rodríguez, M. & Arbizu, J., 2002. The Basal Ganglia and Disorders of Movement: Pathophysiological Mechanisms. *Physiology*.

Paladini, C.A. et al., 2002. Dopamine controls the firing pattern of dopamine neurons via a network feedback mechanism. *PNAS*, pp.2866-71.

Paxinos, G. & Watson, C., 1982. *The rat brain in stereotaxic coordinates: hard cover edition*. New York: Academic press.

Paxinos, G. & Watson, C., 2007. *The Rat Brain in Stereotaxic coordinates*. Academic Press.

Percheron, G. & Filion, M., 1991. Parallel processing in the basal ganglia: up to a point. *Trends Neurosci.*, 14, pp.55–59.

Perkel, D., Gerstein, G. & Moore, G., 1967. Neuronal Spike Trains and stochastic point processes. *Biophysical Journal*.

Perlmutter, J. et al., 1997. Decreased [18F]spiperone binding in putamen in idiopathic focal dystonia. *J. Neurosci.*, 17(2), pp.843-50.

Pessiglione, M. et al., 2005. Thalamic neuronal activity in dopamine-depleted primates: Evidence for a loss of functional segregation within basal ganglia circuits. *Neurosci.*, 6(1523-31), p.25.

Quan, A., May 2011. *Noise, delay, and resonance in a neural network.* Dept of Mathematics, Harvey Mudd college.

Raike, R., Jinnah, H. & Hess, E., 2005. Animal models of generalized dystonia. *NeuroRx.*, 2(3), pp.504-12.

Raz, A., Vaadia, E. & Bergman, H., 2000. Firing patterns and correlations of spontaneous discharge of pallidal neurons in the normal and the tremulous 1-methyl-4-phenyl-1,2,3,6-tetrahydropyridine vervet model of parkinsonism. *J Neurosci*, 20(22), pp.8559-71.

Rivlin-Etzion, M., 2009. *Synchronous Oscillations in the Basal-Gangli-Cortical Network: Do They Generate Tremor and Other Symptoms of Parkinson's Diseases?* Jerusalem: Hebrew University.

Rozanski, V.E. et al., 2014. Connectivity patterns of pallidal DBS electrodes in focal dystonia: A diffusion tensor tractography study. *Neuroimage*, 84, pp.435-42.

Saga, Y. et al., 2011. Origins of multisynaptic projections from the basal ganglia to rostrocaudally distinct sectors of the dorsal premotor area in macaques. *Eur. J. Neurosci.*, 33(2), pp.285-97.

Sanghera, M. et al., 2003. Basal ganglia neuronal discharge in primary and secondary dystonia in patients undrgoing Pallidotomy. *Neurosurgery*, 1358(70), pp.1370-3.

Saxena, 2010. Point process Models show temporal dependecies of basal ganglia nuclei under deep brain stimulation. In *32nd annual International conferebnce of IEEE EMBS*. Buenos Aires, Argentina, 2010.

Schaltenbrand, G. & Wahren, W., 1977. *Atlas for stereotaxy of human brain*. 2nd ed. Thieme.

Schell, G. & Strick, P., 1984. The origin of thalamic inputs to the arcuate premotor and supplementary motor areas. *J. Neurosci.*, 4(2), pp.539-60.

Schuirmann, D.J., 1987. A comparison of the two one-sided tests procedure and the power approach for assessing the equivaloence of average bioavailability. *J. Pharmacokinet. Biopharm.*, 15(6), p.1567.

Sejnowski, B., 1998. A computational model of how Basal Ganglia produces the action sequences. *J of cogn. neurosc*.

Shah, S., 2009. *The what, whys and Hows of Multiple metric Optimization*. [Online] Available at: searchengineland.com/the-what-whys-hows-of-multiple-metric-optimization-24151 [Accessed 2013].

Shaia, W. et al., 2002. Immunhistochemical localization of calcium-binding proteins in the brainstemvestibular nuclei of the jaundiced Gunn rat. *Hear. Res.*, 173, pp.82–90.

Shannon, C., 1948. A mathematical theory of communication. *Bell Systems Tech J*, pp.379–423.

Sharott, A. et al., 2008. Is the synchronization between pallidal and muscle activity in primary dystonia due to peripheral afferance or a motor drive? *Brain*.

Shinomoto, S. et al., 2009. Relating neuronal firing patterns to functional differentiation of cerebral cortex. *PLOS Computational Biology*, 5(7).

Shinomoto, S., Shima, K. & Tanji, J., 2003. Differences in spiking patterns among cortical neurons. *Neural Computation*, 15, pp.2823–42.

Soares, J. et al., 2004. Comparison of the effects of 1-methyl-4-phenyl-1,2,3,6-tetrahydropyridine-induced Parkinsonism and lesions of the external pallidal segment. *J. Neurosc.*, 24(29), pp.6417-26.

Sokolova, M. & Lapalme, 2009. A systematic analysis of performance measures for classification tasks. *Inf. Process. manage.*, 45, pp.427-37.

Starr, P. et al., 2005. Spontaneous pallidal neuronal activity in human dystonia: Comparison with parkinson's disease and normal macaque. *J Neurophysiol*, 93(6), pp.3165-76.

Steine, H., 2010. *Handbook of Basal Ganglia Structure and Function*. I ed. Academic Press.

Strong, S.P., Koberle, R., Steveninck, R.R.d.R.v. & Bialek, W., 1997. Entropy and information in neural spike trains. *Physical Review Letters, APS*, pp.197-200.

Swet, J.A., 1996. *Signal detection theory and ROC analysis in pscychology and diagnostics: collected papers*. Mahwah, NJ: Lawrence Erlbaum.

Taube, J.S., 2010. Interspike interval analyses reveal irregular firing patterns at short, but not long, intervals in rat head direction cells. *Journal of Neurophysiology*, 104(3), pp.1635–48.

Terra, D. et al., 2011. Advance cueing produces enhanced action-boundary patterns of spike activity in the sensorimotor striatum. *J Neurophysiol*.

Tisch, S. et al., 2007. Effect of electrode contact location on clinical efficacy of pallidal deep brain stimulation in primary generalised dystonia. *J. Neurol. Neuosurg. Psychiatry*, 78, pp.1314–19.

Turner, R. & Desmurget, M., 2010. Basal ganglia contributions to motor control: a vigorous tutor. *Curr Opin in Neurobiol.*, 20(6), pp.704-16.

Vega, R., Holloway, K. & Larson, P., 2014. Image-Guided Deep Brain Stimulation. *Neurosurg. Clin. N. Am.*, 25(1).

Vitek, J. et al., 1999. Neuronal activity in the basal ganglia in patients with generalized dystonia and hemiballismus. *Ann. Neurol.*, 46(1), pp.22-35.

Wellek, S., 2010. *Testing statistical hypotheses of equivalence*. II ed. Boca Raton: Chapman & Hall.

Wichmann, T. & DeLong, M., 1999. Oscillations in the basal ganglia. *Nature*, 400(6745), pp.621-2.

Worbe, Y., Yelnik, J. & Lehe ricy, S., 2010. *Basal Ganglia, Elsevier Ltd*.

Yanagisawa, N. & Goto, A., 1971. Dystonia musculorum deformans. analysis with electromyography. *J Neurol Sci.*, 13(1), pp.39-65.

Yoshinori, K. et al., 2013. Quantitative Analysis of Axon Bouton Distribution of Subthalamic Nucleus Neurons in the Rat by Single Neuron Visualization With a Viral Vector. *The Journal of Comparative Neurology | Research in Systems Neuroscience*.

Zhuang, P., Li, Y. & Hallett, M., 2004. Neuronal activity in the basal ganglia and thalamus in patients with dystonia.. *Clin Neurophysiol*, 115(11), p.2542.

APPENDIX

Modeling of Spike Trains

1. Basics of baseline sample sequencing

Considering the vast range of observed neuronal firing patterns in different conditions and species, generation of an enriched neuronal spike train data pool requires complex spike train modeling with control over various discharge features, like refractory limitations, level of irregularities, burstiness and temporal non-homogeneity. Since the overall firing pattern of a neuron can be described anywhere on the regularity spectrum, we employed a renewal point process with a gamma ISI distribution to model the neuronal spiking.

A gamma distribution represents a probability distribution based on two free parameters, allowing regulation of both regularity level and firing rate. The probability density function (PDF) of gamma distribution is as follows:

$$p(t) = \frac{1}{\Gamma(k)} \lambda^k t^{k-1}\, e^{-\lambda t} \qquad \text{…A1}$$

where, Γ is the gamma function with shape parameter (k) and rate parameter (λ). Exponential distribution is a special case of gamma with $k = 1, p(t) = \lambda e^{-\lambda t}$, which indicates a Poissonian interval distribution. For $k > 1$, the process is more regular (sub-Poissonian statistics) and for $k < 1$, the process is more irregular (supra-Poissonian statistics).

The Poisson PDF is given by

$$p(n\ spikes\ during\ t) = \frac{1}{n\,!} \lambda t^n\, e^{-\lambda t} \qquad \text{…A2}$$

The Poisson process will serve as a baseline for simulation of irregular spike train and burst trains, as described in next section.

The probability of a spike train during a short interval is given by:

$$P\ (1\ spike\ during\ \delta t) = \lambda t \delta t \qquad \ldots A3$$

2. *Generation of near-Poissonian trains*

(i) *Homogeneous (rate-stationary) principal irregular train:* inter-spike intervals (ISIs) were randomly choosen from exponential distribution with each successive spike time equal to the previous spike time plus the randomly drawn ISI. In addition, absolute refractory limitations were employed by not allowing any ISI less than or equal to the natural refractory period (2 ms).

(ii) *Homogenous irregular trains with different rate:* This was achieved by increasing the number of spikes (n) and reducing the total time (T), such that rate parameter (λ) is constant ($\lambda = n/T$).

3. *Generation of Regular firing trains*

Principal regular trains were formulated using MATLAB 'linspace' function to generate linearly spaced spike rasters. By varying the total time (T) and number of spikes (n), a pool of regularly firing trains were generated with different firing frequencies. Regular trains were also be generated from Gaussian probability distributions with very high values for shape parameter ($k > 20$). Refer to Appendix figures 1 and 2 for examples.

4. *Generation of Burst Trains*

Burst trains were generated by replacing each spike in a baseline Poissonian train (section 1 and 2 above) with burst/ non-burst epics. The example program for burst train generator is as follows:

(i) Using control parameters of the intended train, total firing rate (R Hz) of the train, total recording duration (T), percentage of spikes in bursts (BP), mean burst order (BO = number of spikes per burst event ranging from three spikes to nine spikes per burst), NBO (spikes per non-burst), the total event rates were calculated as follows

$$Total\ burst\ events\ (TBE) = \frac{\left({}^{BP}/_{100}\right) \times R \times T}{BO}$$

$$Total\ nonburst\ events\ (TNE) = \frac{\left(1 - {}^{BP}/_{100}\right) \times R \times T}{1.2}$$

$$Event\ rate = \frac{TBE+TNE}{T} = R\left\{\frac{(BP)}{BO} + \frac{(1-BP)}{NBO}\right\} \qquad \ldots A4$$

(ii) The baseline Poissonian and regular event trains (rate = event rate above) were generated as described in section 2(i) and 3, respectively.

(iii) Two sets of Poissonian random numbers (*MATLAB function: poissrnd*) were generated with mean parameter equals of BO and NBO, indicating number of spikes for each event in the train. Note, in case of trains with homogenous BO, all spikes in a burst event will be equal to BO.

(iv) Next, each of the above events were allotted randomly to train sequence (*MATLAB function: randperm*) generated in (ii).

(v) The Poissonian model of spike generation was again used for intra-sample sequencing of multi-spikes event. The within-burst ISIs set for ranges from 3-9 ms (excluding the refractory limitations).

Similar simulations were employed to generate a variety of burst trains by varying different control parameters. Refer to Appendix figures 8 and 9 for examples.

5. *Generation of a spike train data pool with different regularity levels*

This was achieved by randomly drawing ISIs from gamma distribution (equation A3) generated with different shape parameters (*MATLAB fuction: gamrnd*). Refer to Appendix figures 1- 7 for examples.

6. *Generation of different spike trains from same ISI distribution*

At first a third order non-oscillatory burst train was generated as described in #4 with its ISI distribution. ISIs was randomly drawn from this distribution to generate a near-Poissonian train. Similarly, from the same ISI distribution, all ISIs were arranged in decreasing order to generate a regular train (figure 3, main paper).

7. *Generation of non-stationary trains*

To generate non-stationarity in a spike train, epochs of different pattern-rate features were randomly replaced. Each of the three principal trains was corrupted by randomly introducing 0-5, 6 s corruption epochs (with train duration 60 s, the corruption varied from 0- 50% of the total train). The corruption epochs were defined as burst or non-burst epochs, with varying rate and baseline regularity. For burst corruption, BO, event rate, burst type (mixed or pure BO) were randomly varied for each epoch. Refer to Appendix figures 10-12 for examples.

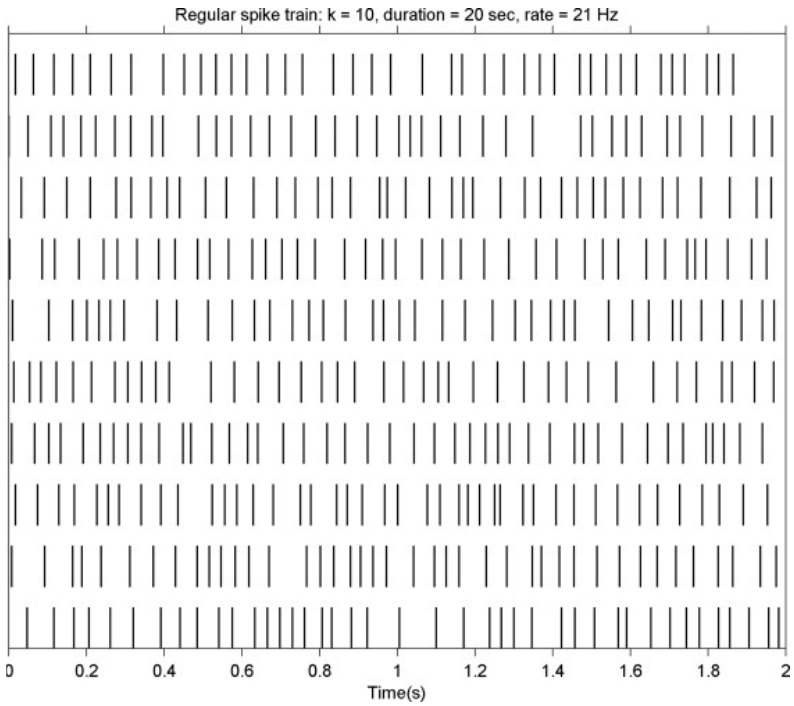
Regular spike train: k = 10, duration = 20 sec, rate = 21 Hz
0
0.2
0.4
0.6
0.8
1
1.2
1.4
1.6
1.8
2
Time(s)

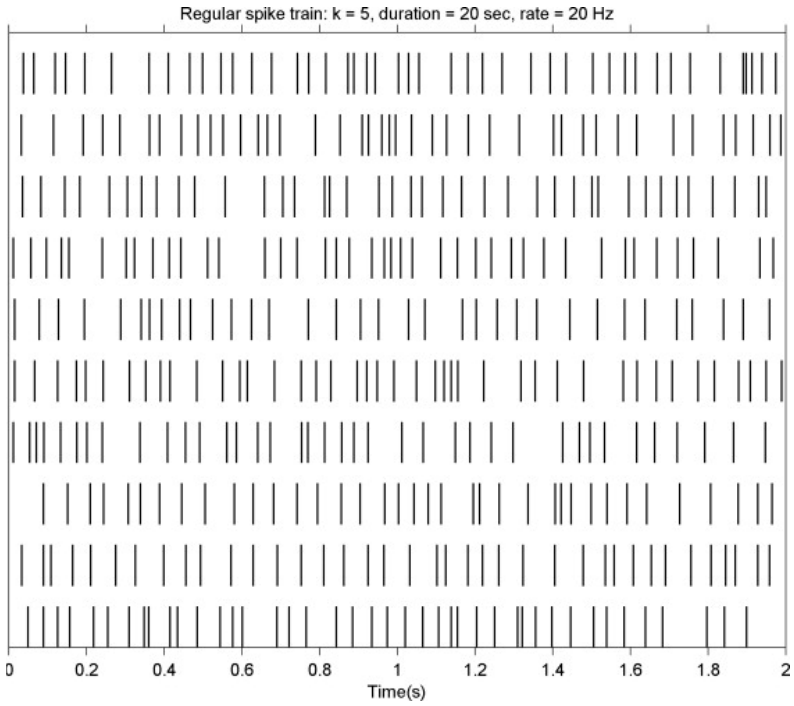
Regular spike train: k = 5, duration = 20 sec, rate = 20 Hz
0
0.2
0.4
0.6
0.8
1
1.2
1.4
1.6
1.8
2
Time(s)

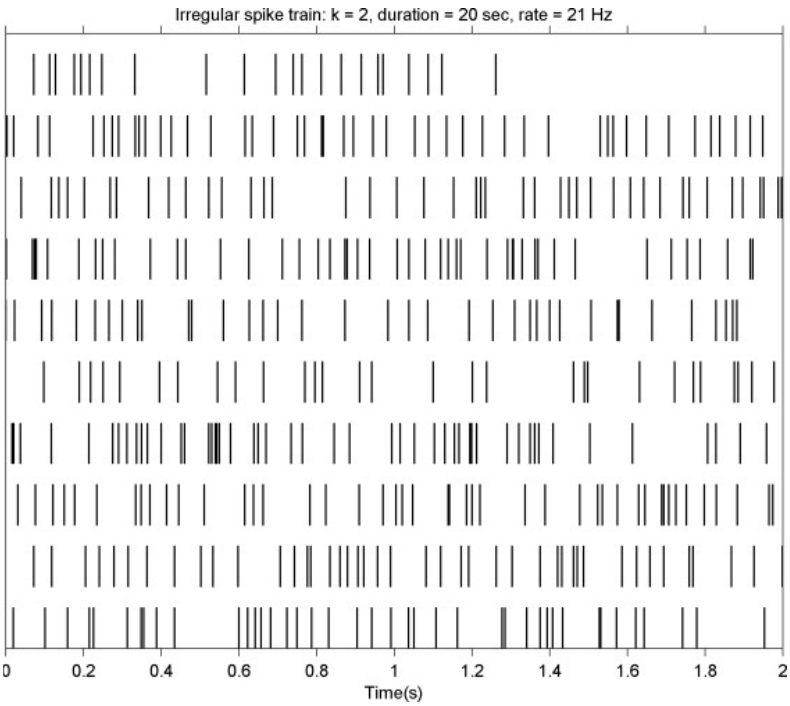
Irregular spike train: k = 2, duration = 20 sec, rate = 21 Hz
0
0.2
0.4
0.6
0.8
1
1.2
1.4
1.6
1.8
2
Time(s)

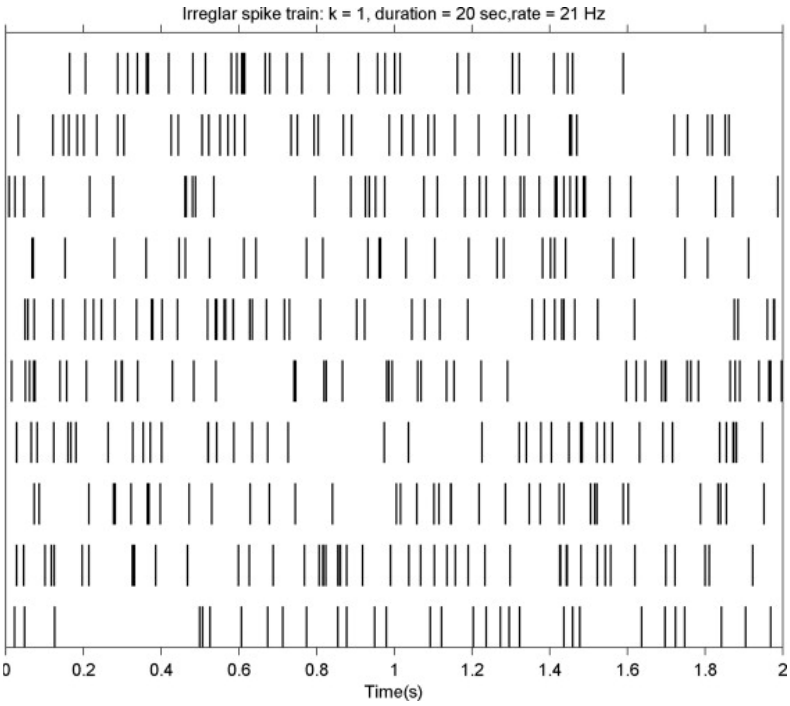
Irreglar spike train: k = 1, duration = 20 sec,rate = 21 Hz
0
0.2
0.4
0.6
0.8
1
1.2
1.4
1.6
1.8
2
Time(s)

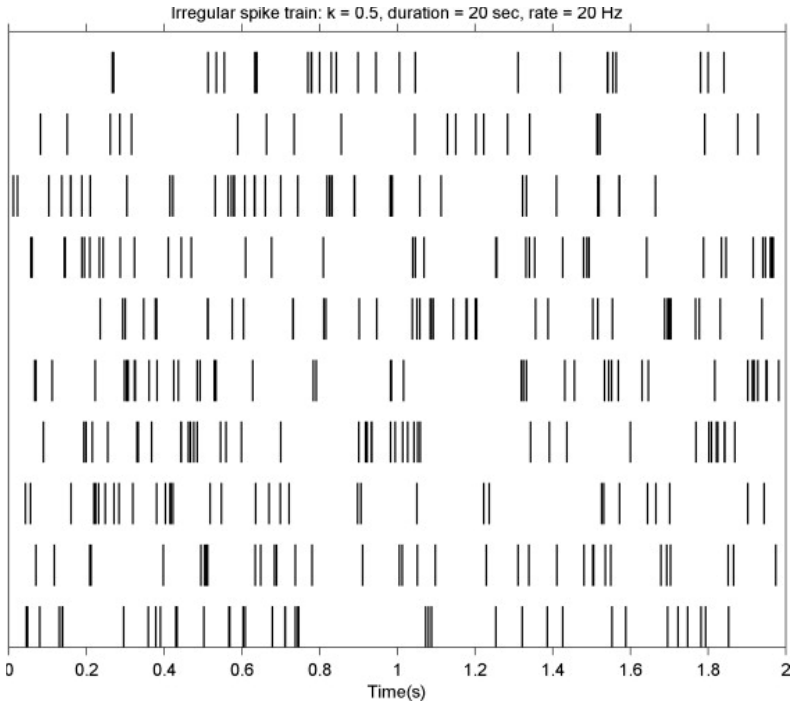
Irregular spike train: k = 0.5, duration = 20 sec, rate = 20 Hz
0
0.2
0.4
0.6
0.8
1
1.2
1.4
1.6
1.8
2
Time(s)

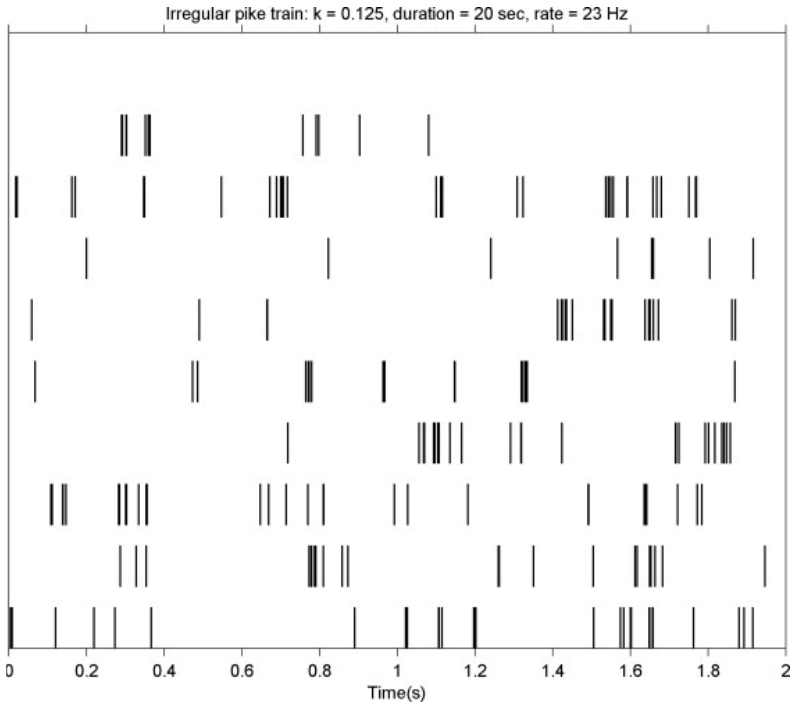
Irregular pike train: k = 0.125, duration = 20 sec, rate = 23 Hz
0
0.2
0.4
0.6
0.8
1
1.2
1.4
1.6
1.8
2
Time(s)

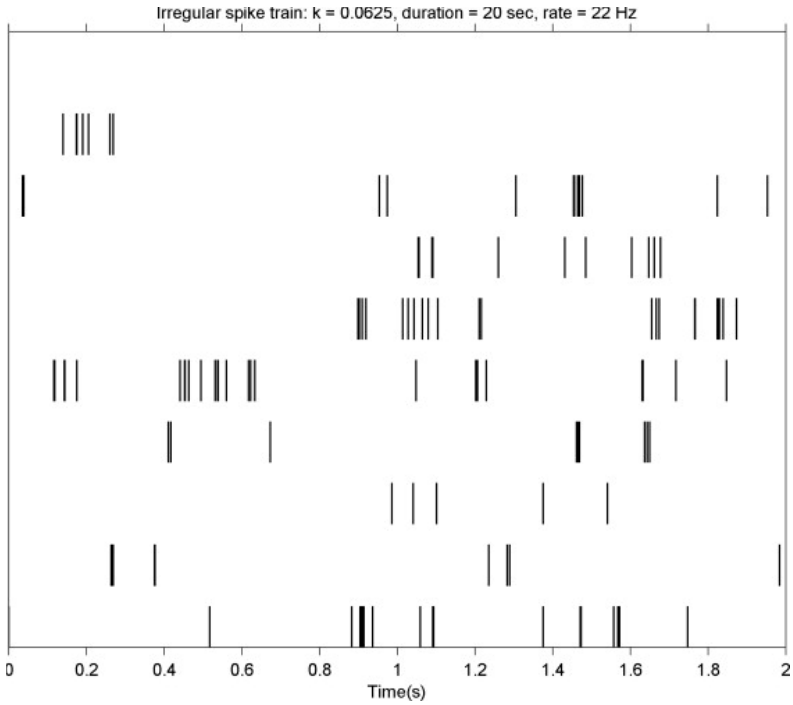
Irregular spike train: k = 0.0625, duration = 20 sec, rate = 22 Hz
0
0.2
0.4
0.6
0.8
1
1.2
1.4
1.6
1.8
2
Time(s)

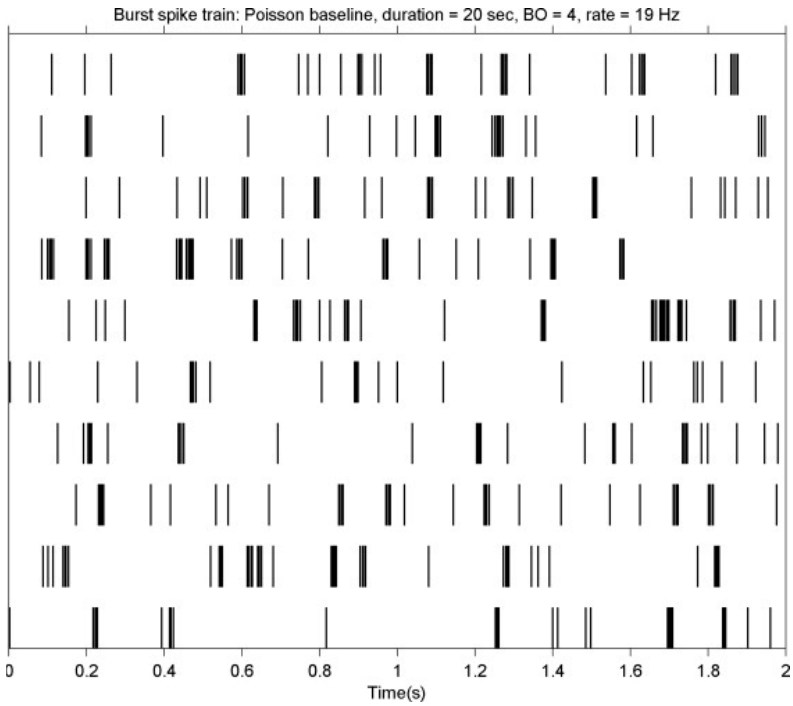
Burst spike train: Poisson baseline, duration = 20 sec, BO = 4, rate = 19 Hz
0
0.2
0.4
0.6
0.8
1
1.2
1.4
1.6
1.8
2
Time(s)

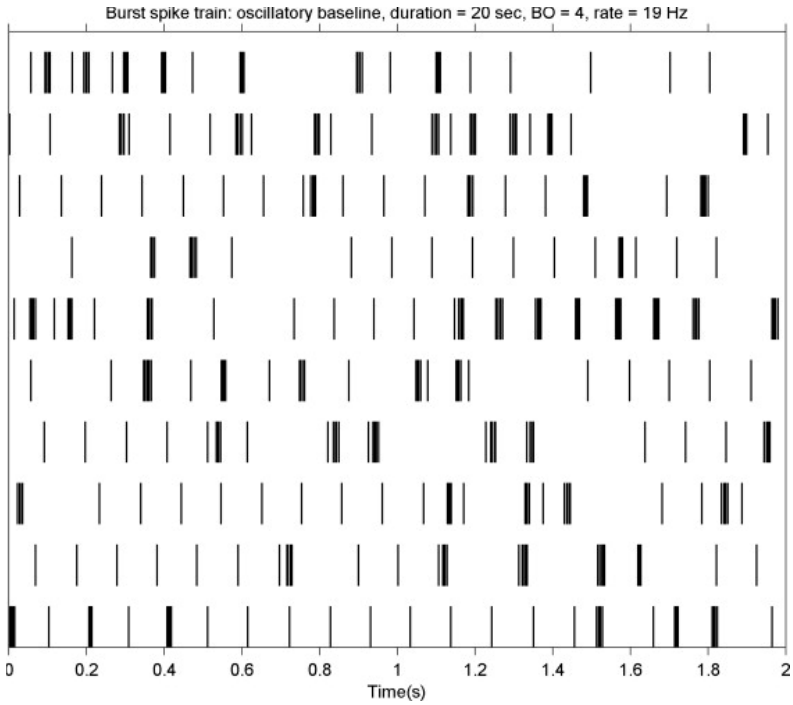
Burst spike train: oscillatory baseline, duration = 20 sec, BO = 4, rate = 19 Hz
0
0.2
0.4
0.6
0.8
1
1.2
1.4
1.6
1.8
2
Time(s)

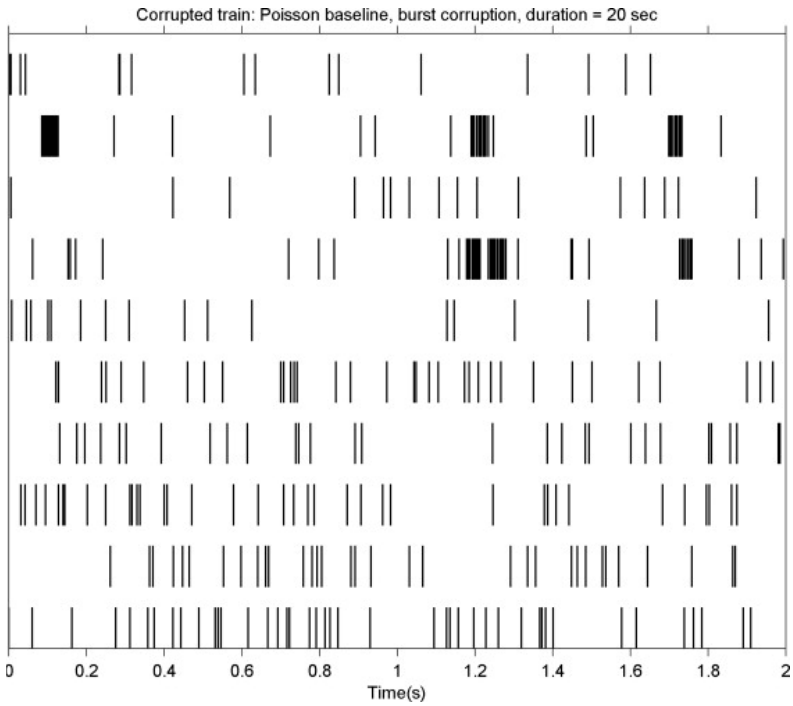
Corrupted train: Poisson baseline, burst corruption, duration = 20 sec
0
0.2
0.4
0.6
0.8
1
1.2
1.4
1.6
1.8
2
Time(s)

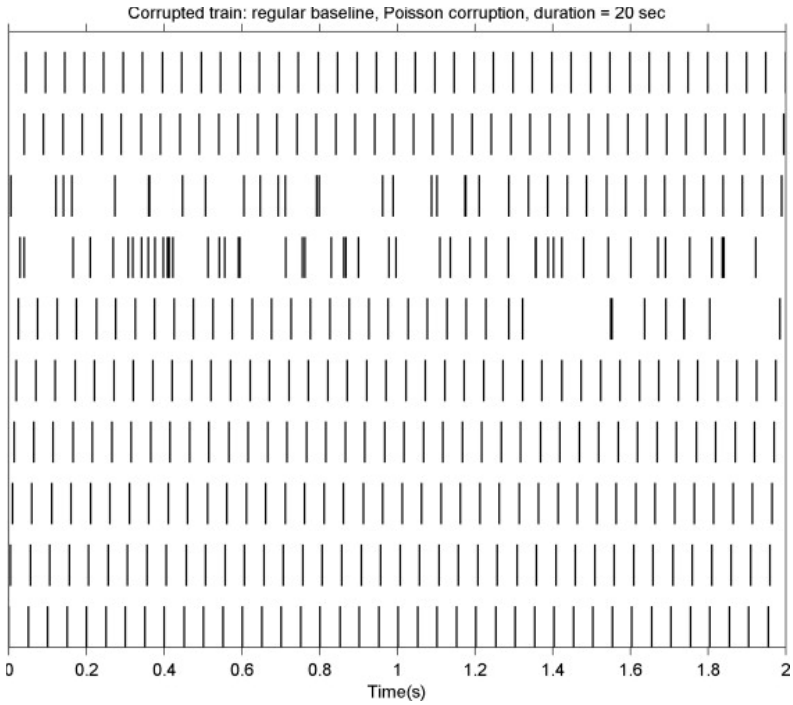
Corrupted train: regular baseline, Poisson corruption, duration = 20 sec
0
0.2
0.4
0.6
0.8
1
1.2
1.4
1.6
1.8
2
Time(s)

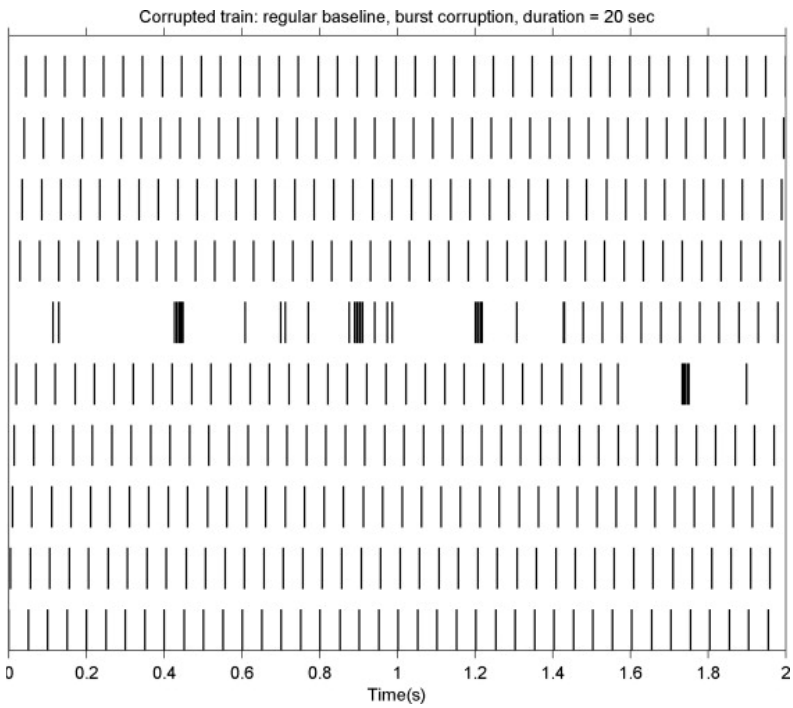
Corrupted train: regular baseline, burst corruption, duration = 20 sec
0
0.2
0.4
0.6
0.8
1
1.2
1.4
1.6
1.8
2
Time(s)